

MODELING WATER VAPOR USING GPS
WITH APPLICATION TO MITIGATING INSAR
ATMOSPHERIC DISTORTIONS

A DISSERTATION
SUBMITTED TO THE DEPARTMENT
OF ELECTRICAL ENGINEERING
AND THE COMMITTEE ON GRADUATE STUDIES
OF STANFORD UNIVERSITY
IN PARTIAL FULFILLMENT OF THE REQUIREMENTS
FOR THE DEGREE OF
DOCTOR OF PHILOSOPHY

Fayaz Onn
November 2006

© Copyright by Fayaz Onn 2007
All Rights Reserved

I certify that I have read this dissertation and that, in my opinion, it is fully adequate in scope and quality as a dissertation for the degree of Doctor of Philosophy.

(Howard A. Zebker) Principal Advisor

I certify that I have read this dissertation and that, in my opinion, it is fully adequate in scope and quality as a dissertation for the degree of Doctor of Philosophy.

(David P. Hinson)

I certify that I have read this dissertation and that, in my opinion, it is fully adequate in scope and quality as a dissertation for the degree of Doctor of Philosophy.

(John M. Pauly)

Approved for the University Committee on Graduate Studies.

Abstract

Spatial and temporal fluctuations of water vapor content in the lower atmosphere cause variable time delays in radio-frequency signals propagating from space-borne transmitters to targets on the ground. These delays result in significant distortions in repeat-pass Interferometric Synthetic Aperture Radar (InSAR) images of crustal deformation and errors in Global Positioning System (GPS) position estimates. Temporal variability of these errors can be estimated directly from GPS data, but spatial variations of water-vapor-induced distortions cannot easily be separated from signals due to true ground motion in InSAR images.

The primary objective of this work is to reduce water-vapor-induced phase distortions in InSAR images using GPS measurements. We present methods of estimating maps signal delay - proportional to total column water vapor - from time series measurements acquired from a sparse network of GPS receivers. Reducing the InSAR phase distortions with these maps allows the detection of any smaller magnitude ground motion signals in the radar image.

The fundamental problem in meeting our objective is estimating delay maps at the high resolution of InSAR from spatially-sparse GPS measurements. We address this problem in two steps. In the first step, we characterize the spatial variability of water-vapor-induced delay in InSAR observations according to two physical mechanisms. The InSAR atmospheric phase variability consists of a topography-dependent component due to vertically-stratified water vapor and another component caused by horizontal turbulent mixing of water vapor. Using only GPS data recorded at the radar observation times, we measure the effect of vertical stratification and estimate a map showing topography-dependent water vapor variations which reduces InSAR phase distortions in the interferogram by 46%. We use the same

GPS measurements, corrected for altitude-dependent water vapor, to spatially interpolate another map which then reduces the residual phase errors due to atmospheric turbulence by 6%. The accuracy of this correction is limited by the sparse network of GPS observations in the imaged area.

In the second step, we have developed two techniques, one based on statistics of an advected water-vapor-induced delay field and the other based on a model for advection and diffusion of moisture, that allows us to incorporate additional GPS measurements from before and after the radar image acquisition time to estimate water vapor maps that more accurately correct the phase distortions due to turbulence. The first method is based on the “frozen-flow” hypothesis of advecting slab of atmosphere driven by mean wind. In our algorithm, we estimate mean flow over time from covariance analysis of the GPS delay time series. The mean flow estimates provide denser networks of control points which we spatially interpolate to generate a map of water vapor. This map reduces the residual phase error by an additional 7% reduction over that achieved using only GPS data acquired at the acquisition times. Much of the remaining error is due to short scale decorrelation noise that cannot be reproduced using GPS data. Ignoring the high-frequency phase variations by prior smoothing of the data, our method realizes a 31% additional reduction in phase error.

In the second algorithm, we estimate maps of signal delay by solving an inverse problem of fitting a deterministic transport model of water total column water vapor to GPS time series measurements acquired from a sparse network. This model generalizes the “frozen-flow” hypothesis and is derived from the conservation of mass and humidity in the atmosphere. The model is parametrized by spatially-variable two-dimensional flow field and turbulent diffusion. We develop a finite-difference scheme for regularized, least-squares estimation of the flow field. These flow fields measure the vertically-integrated wind in the atmosphere. We use these flow estimates in an iterative algorithm based to generate a map of atmospheric delay from time series of delay measurements from GPS acquired around the radar image acquisition times. This method yields water vapor maps that reduce the phase errors by an additional 17% over the reduction achieved using only data at the radar image acquisition time.

Acknowledgements

This dissertation concludes six years of my graduate study and research at Stanford University. I would like to take this opportunity to express my heartfelt gratitude to all the people who have helped me reach this point.

First and foremost, I would like to express my deep and sincere thanks to Professor Howard Zebker, who served as my principal dissertation advisor, for his guidance, support and mentorship during my tenure as a graduate student at Stanford University. I am grateful to Dr. David P. Hinson for serving as my associate dissertation advisor and for providing insightful and constructive comments on my dissertation and during my oral defense. My gratitude also goes to Professor John M. Pauly for serving as my third reader, and to Professor Paul Segall for chairing my oral defense.

It has been a privilege for me to be a part of the Radar Interferometry Group in STARlab. My sincere gratitude goes to my fellow groupmates, Leif Harcke, Shadi Oveisgharan, Lauren Wye, Ana Bertran-Ortiz, Sang-Ho Yun, Andy Hooper, Piyush Shanker, Joern Hoffman, Sigurjon Johnson and Curtis Chen. It has been my honor to have worked with these individuals in various problems and projects in the field of interferometric radar.

I would like to extend my sincere thanks to the professors, researchers, staff and students of STARlab whom have contributed, in their own way, to this work. In particular, I thank Professor Len Tyler, Professor Tony Frasier-Smith and Dr. Ivan Linscott for their guidance and encouragement. I am grateful to the students of the Radioscience community in STARlab, especially Hrefna Gunnarsdottir, Ahmed Kamal Sultan Salem, Kerri Kusza, Fraser Thomson, Bob Marshall and Tim Chevalier, for their continual assistance, in all matters technical and non-technical, and for their invaluable support.

I have been fortunate to have had the opportunity to interact with many people outside of Electrical Engineering. To these individuals, in particular Emeric Henry, Prakash Kannan, Joanne Yoong and Eleni Diamanti, I extend my heartfelt thanks for their steadfast friendship and warm company all through my years at Stanford.

Finally, none of this would have been possible without the unfailing love and support of family, to whom I owe everything.

Contents

Abstract	v
Acknowledgements	vii
List of Symbols	xix
1 Introduction	1
1.1 Objectives	6
1.2 Contributions	8
1.3 Outline	9
2 Water vapor in the atmosphere	11
3 GPS and InSAR	17
3.1 Introduction	17
3.2 Global Positioning System	18
3.3 InSAR	24
3.3.1 SAR	24
3.3.2 Interferometric SAR	27
3.4 Conclusions	32
4 The neutral atmospheric signal in GPS and InSAR	35
4.1 Introduction	35
4.2 Meteorological dependence	36
4.3 Spatial and temporal variability	43

4.3.1	Vertically-stratified neutral atmosphere	45
4.3.2	Variability due to turbulent mixing	48
4.4	Overview of other existing approaches	57
5	Estimating atmospheric phase signatures from GPS	63
5.1	Introduction	63
5.2	Topography-dependent atmospheric phase	64
5.3	Magnitude and correlation of the turbulent component	68
5.4	Estimating the turbulently-mixed atmospheric phase	73
5.5	Summary	77
6	The “frozen-flow” algorithm	79
6.1	Introduction	79
6.2	The “frozen-flow” algorithm	81
6.2.1	Estimating mean wind from the GPS network data	81
6.2.2	Generating dense networks of ZWD control points	83
6.3	Interpolating a IWV difference map	85
6.4	Discussion	91
6.5	Conclusions	100
7	Advection-diffusion modeling of wet delay	103
7.1	Derivation of the 2D ZWD transport model	106
7.1.1	Conservation of IWV	106
7.1.2	Incorporating turbulent mixing effects	111
7.2	Algorithm implementation	115
7.2.1	Finite-difference ZWD transport model	115
7.2.2	Estimating spatially-variable mean flow	117
7.2.3	Estimating IWV difference maps	120
7.3	Results	124
7.4	Discussion	129
7.5	Conclusions	135

8	A case study	137
8.1	GPS and InSAR observations	138
8.1.1	Vertical-dependence of GPS and InSAR delays	139
8.2	Spatial and temporal variability	144
8.3	Estimating the turbulent phase variations	148
8.3.1	Frozen-flow algorithm	148
8.3.2	Advection-diffusion modeling of GPS ZWD	152
9	Conclusions	157
9.1	Contributions	157
9.2	Future directions	159
A	Dependence of Zenith wet delay on specific humidity	161
B	Structure functions and PSD of phase and ZWD	163
B.1	Introduction and preliminaries	163
B.2	2D structure function of InSAR atmospheric phase	164
B.3	2D PSD of InSAR atmospheric phase	166
B.4	1D structure function of GPS ZWD	167
B.5	1D PSD of GPS ZWD	169
	Bibliography	171

List of Tables

3.1	ERS parameters	24
5.1	Parameter estimates of altitude-dependent model	66
5.2	Parameter estimates of altitude-dependent model direct fit	66
5.3	Parameter estimates of spatial autocorrelation model	74
5.4	RMS atmospheric phase with overpass-time-only corrections	77
6.1	RMS atmospheric phase for frozen-flow correction	88
7.1	Cross-validation RMS errors for advection-diffusion modeling	126
7.2	RMS atmospheric phase for advection-diffusion modeling corrections . . .	130
8.1	Parameter estimates of altitude dependent model to case study GPS data . .	142
8.2	Parameter estimates for direct fit of altitude-dependent model to case study InSAR data	143
8.3	RMS atmospheric phase for frozen-flow correction on case study data . . .	152
8.4	RMS atmospheric phase for advection-diffusion modeling correction on case study data	155

List of Figures

1.1	Radar interferogram from Peltzer, 1998	3
1.2	Radar interferogram from Hanssen, 1999	4
1.3	Radar interferograms from Zebker, 1997	5
2.1	Layers of the atmosphere	12
2.2	Radiosonde relative humidity measurements	14
2.3	Total column water vapor from a microwave radiometer	15
2.4	Temperature and humidity from GPS limb sounding	16
3.1	GPS cone averaging effect	21
3.2	GPS ZWD timeseries from the SCIGN network	23
3.3	SAR imaging geometry	25
3.4	SAR and InSAR images over Death Valley	27
3.5	InSAR viewing geometry	28
3.6	Atmospheric effects in a SAR interferogram over Southern California	33
4.1	Neutral atmospheric propagation medium	36
4.2	Comparison between InSAR and GPS ZWD differences	42
4.3	Vertical stratification of the neutral atmosphere	45
4.4	GPS and InSAR data as a function of altitude	46
4.5	Relative change of ZWD over time	48
4.6	Treuhaft-Lanyi structure function model	51
4.7	Structure functions from GPS and InSAR	53
4.8	Locations on structure function grid where sparse samples are estimated	54

4.9	Spectra from GPS and InSAR	56
5.1	Vertical profile model fitted to GPS and InSAR data	67
5.2	Topography-dependent maps	68
5.3	Comparison between GPS and InSAR measurements corrected for vertical- dependence	69
5.4	Correlation coefficient of GPS and InSAR turbulent fluctuations	71
5.5	Spatial autocorrelation function of GPS and InSAR turbulent delay variations	73
5.6	IWV maps interpolated from GPS using kriging	76
6.1	Polar motion plot of wind vectors from the “frozen-flow” algorithm	83
6.2	Denser network of ZWD control points inferred by the “frozen-flow” algo- rithm	84
6.3	IWV maps interpolated the “frozen-flow”-generated network of control points	86
6.4	Transect through observed InSAR atmospheric phase and interpolated IWV maps	87
6.5	RMS error surface	89
6.6	Empirical spatial autocorrelation profiles from GPS and InSAR before and after applying the “frozen-flow” algorithm	94
6.7	Target map used in numerical simulation	97
6.8	Sampling patterns	98
6.9	RMS error curves from numerical simulation	99
7.1	1D illustration of passive scalar conservation	109
7.2	1D illustration of passive scalar conservation assuming turbulent wind fluc- tuations	113
7.3	Computational grid	116
7.4	Algorithm flow chart	123
7.5	Spatially-variable flow fields on Feb. 5th, 2000	125
7.6	Spatially-variable flow fields on Nov. 27th, 1999	125
7.7	IWV maps generated by the advection-diffusion algorithm	128
7.8	RMS error as a function of time window length	129

7.9	Average flow speeds	132
7.10	Diffusion coefficient and RMS error as a function of time scale	134
8.1	GPS ZWD timeseries from the SCIGN network in 2005	138
8.2	Radar interferogram over Southern California showing atmospheric phase variations in 2005	140
8.3	GPS and InSAR plotted as a function of altitude in 2005	141
8.4	Topography-dependent maps of atmospheric phase generated from data in 2005	143
8.5	Comparison between GPS and InSAR data in 2005	145
8.6	Power spectra computed from GPS and InSAR data in 2005	146
8.7	Spatial autocorrelation of GPS and InSAR data in 2005	147
8.8	Polar motion plots of wind solution inferred from the frozen-flow algorithm applied to GPS data in 2005	149
8.9	IDW maps generated by the frozen-flow algorithm on data acquired in 2005	151
8.10	IWV difference maps from the advection-diffusion algorithm, applied to data in 2005	153
8.11	RMS error for between observed InSAR atmospheric phase and inferred IWV maps from the advection-diffusion algorithm, 2005	154

List of Symbols

1D	one dimensional.
2D	two dimensional.
3D	three dimensional.
\mathbf{A}_k	$M^2 \times 2(M^2 + M)$ matrix, finite-difference first derivative operator
$A(x, y, z)$	amplitude of electromagnetic wave
B_{perp}	perpendicular component of the interferometric baseline
B	interferometric baseline
\mathbf{B}_k	$M^2 \times M^2$ matrix of flow-dependent weights at k -th time step
c	speed of light
$C(\mathbf{r})$	3D correlation function of g
C	ZWD recorded at sea-level or 2D autocorrelation mean-square parameter
j	
\mathbf{C}	covariance matrix of measured GPS ZWD
$C]_{ij}$	element of covariance matrix of measured GPS ZWD
$\hat{\mathbf{C}}(\mathbf{R}_k)$	estimate of autocorrelation function gradient at lag \mathbf{R}_k
dx	infinitesimal length on the x axis
dz	infinitesimal length on the z axis
$d\mathbf{k}$	infinitesimal volume in wavenumber space
$D(\mathbf{r})$	3D structure function of g , or Kolmogorov structure function of refractivity
$D_\phi(\mathbf{R})$	2D structure function of InSAR phase
$D_{GPS}(\tau)$	1D structure function of GPS wet delay as a function of time
$\hat{D}_l(\mathbf{R}_k)$	empirical structure function from GPS ZWD
d_i	element of cross-correlation vector

e	partial pressure of water vapor
f_s	sampling frequency
f	temporal frequency
F	passive scalar
\bar{F}	mean passive scalar
F'	passive scalar fluctuation
$g(\cdot)$	wide-sense stationary random function
H	tropospheric scale height
\mathbf{H}_1	regularization matrix implementation incompressibility condition
\mathbf{H}_2	regularization matrix implementation irrotationality condition
h	height of mountain
k	GPS satellite number, or wavenumber
k_1, k_2, k'_2, k_3	constants in refractivity equation
k_x, k_y, k_z	x , y and z wavenumbers
k_o	wavenumber corresponding to outer scale of turbulence
k_i	wavenumber corresponding to inner scale of turbulence
K	turbulent diffusion coefficient
$l_{hyd}^{GPS,z}$	GPS zenith hydrostatic delay
l_{hyd}^z	zenith hydrostatic delay
$l_{wet}^{GPS,z}$	GPS zenith wet delay
l_{wet}^z	zenith wet delay
$l_{wet}^{GPS,z}(x, y, t)$	GPS zenith wet delay as a function of two spatial coordinates and time
$l_{wet}(t)$	wet delay as a function of time
\mathbf{l}_{m+1}^{GPS}	$M \times 1$ vector containing measured ZWD from GPS
\bar{l}_{wet}^z	mean ZWD, averaged over grid cell
l'_{wet}	turbulent fluctuation of ZWD
\hat{l}_{wet}	krig estimate of ZWD
l_{wet}^{InSAR}	InSAR wet delay difference
$l_{wet}^z(i, j, k)$	wet delay at grid cell (i, j) and time step k
\mathbf{l}_k	$M \times 1$ vector of ZWD of all grid cells
L	height of radiation source from the ground

L_{cloud}	cloud thickness
l_{cloud}^z	zenith delay due to liquid water in clouds
l_i	inner scale of turbulence
l_o	outer scale of turbulence
$l_{vert}(z)$	vertical-dependent wet delay model
l_{min}	minimum ZWD measured by GPS at SAR overpass times
L^*	characteristic length scale
l^*	characteristic wet delay scale
L_0	Von Karman PSD parameter
m	element number of \mathbf{l}_k
M	grid dimension
M_w	Earthquake magnitude, Richter scale
N^k	integer number of cycles of phase corresponding to range to the k -th GPS satellite
n	refractive index of the neutral atmosphere
n_{SAR}	InSAR phase measurement noise random variable
N	neutral atmospheric refractivity
$N(x, y, z, t)$	neutral atmospheric refractivity as a function of three spatial coordinates and time
N_{hyd}	hydrostatic component of neutral atmospheric refractivity
N_{wet}	wet component of neutral atmospheric refractivity
P	atmospheric pressure
\hat{P}_l	cross-correlation of GPS ZWD at consecutive times
q	specific humidity
R_d	specific gas constant of dry air
g_m	local gravity at the center of an atmospheric column
P_s	surface pressure
R_v	specific gas constant of water vapor
r_1	range from SAR at pass 1 to resolution cell at height z
r_2	range from SAR at pass 2 to resolution cell at height z
\mathbf{R}	Rotation matrix or spatial separation in (x, y) plane
R_x	x -component of spatial separation
R_y	y -component of spatial separation

\mathbf{R}_k	k -th lag where autocorrelation is estimated from GPS data
SNR	Signal-to-noise ratio
$S(\mathbf{k})$	3D power spectral density (PSD) of g , or Kolmogorov PSD of refractivity
$S_\phi(\mathbf{u})$	2D PSD of InSAR phase
$S_{GPS}(f)$	1D PSD of GPS wet delay
$S(\mathbf{R}_k)$	set of GPS site-pairs separated by \mathbf{R}_k
t_1	SAR acquisition 1
t_2	SAR acquisition 2
t	time
T	atmospheric temperature
T^*	characteristic time scale
T_m	weighted mean temperature
T_s	surface temperature
T_{window}	time window length about SAR overpass
t_i^n	GPS ZWD time stamp on i -th SAR overpass
U	electromagnetic wave or x component of vertically-averaged wind
U_A	x -component of 2D flow at grid cell A
U_C	x -component of 2D flow at grid cell C
U_D	x -component of 2D flow at grid cell D
U_P	x -component of 2D flow at grid cell P
$U(i - 1/2, j)$	x -component of 2D flow at sides of a grid cell (i, j)
\bar{U}	x component of mean 2D flow
U'	x component of 2D vertically-averaged turbulent wind perturbation
u	x component of 3D wind
\mathbf{u}	wavenumbers in two dimensions
v	spacecraft velocity or y component of 3D wind
\mathbf{V}	wind velocity
\bar{V}	y component of mean 2D flow
V'	y component of 2D vertically-averaged turbulent wind perturbation
\mathbf{V}^{3D}	actual 3D winds in the atmosphere
V	y component of vertically-averaged wind

V_x	x -component of wind velocity
V_y	y -component of wind velocity
V_A	y -component of 2D flow at grid cell A
V_C	y -component of 2D flow at grid cell C
V_D	y -component of 2D flow at grid cell D
V_P	y -component of 2D flow at grid cell P
$V(i, j - 1/2)$	y -component of 2D flow at sides of a grid cell (i, j)
\mathbf{v}_k	$2(M^2 + M) \times 1$ vector of 2D flow at all grid cell sides
V^*	characteristic velocity scale
$\hat{\mathbf{V}}$	estimate of 2D wind
\mathbf{w}	vector of kriging weights
W	liquid water content in the atmosphere
W_x, W_y	x and y wavelengths of spatial autocorrelation model
$w(t)$	white noise random process
w	z component of 3D wind
w_i	krig weights
x	azimuth coordinate
(x_a, y_a)	x, y coordinates of a particular GPS site
\mathbf{x}	GPS receiver position
x_0, y_0	unsampled location where ZWD is krig-interpolated
y	slant range coordinate
z	height of a target on the ground, or vertical coordinate
α	vertical decay rate of ZWD or tropospheric drift rate parameter
β	Von Karman PSD power index
χ^2	chi-squared random variable
Δ	grid cell spacing
Δr	path length difference of a resolution to SAR at both passes
Δt	time sampling
Δt_{clock}^k	k -th GPS satellite clock offset
Δt_{clock}	GPS receiver clock offset
ΔT	GPS ZWD time sampling interval

Δl_{wet}	difference of GPS ZWD at the two SAR overpass times
ε	dielectric constant of the neutral atmosphere
γ	GPS satellite elevation angle or correlation coefficient between GPS and InSAR measurements
ϕ^{GPS}	GPS carrier phase
$\phi^{GPS,k}$	GPS carrier phase from the k -th GPS satellite
ϕ_{iono}^{GPS}	GPS carrier phase shift due to ionospheric propagation
ϕ_{NA}^{GPS}	GPS carrier phase shift due to neutral atmospheric propagation
ϕ_{errors}^{GPS}	GPS carrier phase shift due to errors
$\phi_{NA}^{GPS,z}$	zenith neutral atmospheric delay
ϕ_{topo}^{INSAR}	InSAR topographic phase
ϕ^{INSAR}	InSAR interferometric phase
$\phi^{INSAR}(x,y)$	radar interferogram in azimuth and range coordinates
ϕ_{noise}^{INSAR}	InSAR phase noise
$\phi(x,y,z)$	phase of electromagnetic wave as a function of 3 spatial coordinates
ϕ_{defo}^{INSAR}	InSAR deformation phase
ϕ_{iono}^{INSAR}	InSAR differential phase shift due to ionospheric signal propagation
ϕ_{NA}^{INSAR}	InSAR differential phase shift due to neutral atmospheric signal propagation
ϕ_{orbit}^{INSAR}	InSAR phase due to errors in satellite orbits
ϕ_{hyd}^{INSAR}	InSAR hydrostatic differential phase shift
ϕ_{wet}^{INSAR}	InSAR wet differential phase shift
λ	wavelength
∇^2	$M^2 \times M^2$ matrix, finite-difference second derivative operator
∇	gradient operator
κ	constant of proportionality between IWV and ZWD
ρ_v	density of water vapor
ρ_S^k	position of k -th GPS satellite in an inertial reference frame
ρ	density of air
ρ_a, ρ_b	location of GPS sites in a pair separated by \mathbf{R}_k
ρ^k	geometric distance from a GPS receiver to the k th GPS satellite
σ_{SAR}^2	InSAR phase measurement noise variance

σ_{GPS}^2	GPS ZWD measurement noise variance
θ	radar look angle
τ	time separation
τ_x, τ_y	x and y decay parameters of spatial autocorrelation model
IWV	integrated water vapor
PW	precipital water vapor
ZWD	zenith wet delay

Chapter 1

Introduction

We consider the effects of atmospheric water vapor on observations from two satellite-based, active microwave remote-sensing systems, namely the Global Positioning System (GPS) and Interferometric Synthetic Aperture Radar (InSAR).

Over the past two decades, space-based GPS and InSAR have revolutionized geodesy. GPS was originally designed as a navigation and time transfer tool (Bevis et al. (1992)). Advances in GPS technology over the past decade or so have made GPS the geodetic tool of choice for studying crustal motion over time (Segall and Davis (1997)). A powerful feature of GPS is its ability to provide measurements of a receiver's position at fine time resolution. Also, over the past twenty years InSAR has proven to be a powerful tool for mapping and studying numerous geophysical phenomena on Earth. InSAR observations have been widely used to derive high-resolution topographic maps of the Earth (Zebker and Goldstein (1986)), observe ocean currents (Goldstein and Zebker (1987)) and measure crustal deformation due to volcanoes and earthquakes (Massonnet et al. (1993), Massonnet et al. (1994)), along with the many other applications of the technique. A key property of InSAR is the fine spatial resolution (20 meters) combined with large coverage (100 kilometer wide swath) of observations.

GPS and InSAR are termed active remote-sensing techniques because they illuminate an area on the ground with pulses of radio-frequency (RF) energy, in contrast to passive systems which use naturally occurring sources of radiation such as solar radiation or electromagnetic emissions from the Earth's surface and atmosphere. Unlike some water vapor

remote sensing systems, GPS and InSAR are not restricted to daytime operation. Furthermore, since clouds are relatively transparent to RF signals, these two systems can be used even in the presence of condensation and precipitation in the atmosphere.

GPS and InSAR are most often used to determine the position of targets on the ground accurately. GPS methods measure time-varying positions of fixed points on the ground over time while repeat-pass InSAR measures the three-dimensional locations of a field of targets as well as the relative motion of those targets between two time instances, typically months or years apart. These systems infer target positions by measuring the travel time of electromagnetic signals propagating from the space-borne transmitters to those targets. In Chapter 3, we give an overview of the GPS and InSAR remote sensing techniques.

The atmosphere, in general, and water vapor in particular affects GPS and InSAR signals similarly. The refractive index of water vapor at radio frequencies is about 20 times greater than at optical wavelengths (Olmi (2001)). This relatively large refractive index is due to the polar nature of the water vapor molecule (Solheim et al. (1999)). Since GPS and InSAR signals propagate through the atmosphere, atmospheric water vapor reduces the propagation velocity of GPS and InSAR signals, delaying the time taken for these signals to reach the ground (Zebker et al. (1997)). These unknown delays cause errors when inferring target positions from GPS and InSAR observations. Moreover, as the distribution of water vapor in the atmosphere is highly variable, these time delays fluctuate significantly over a wide range of temporal and spatial scales. Time delays due to atmospheric water vapor are often regarded as high-frequency errors and short-scale variations in GPS and InSAR observations respectively. While techniques have been developed to estimate this rapidly fluctuating delay component in GPS measurements (Bevis et al. (1992)), water-vapor-induced delay distortions cannot be easily separated from signals due to ground motion in InSAR observations (Hanssen (1998)). Zebker et al. (1997) show that a 20% change in spatial or temporal relative humidity can result in 10 – 14 cm error in ground deformation retrievals.

In Figure 1.1(a), we show an InSAR image, called a radar interferogram, formed by Peltzer et al. (1998) from two radar observations of the Landers, California area on September 27, 1992 and January 23, 1996. This image is one of seven similar images of the area that the authors formed from 10 radar observations made on various dates after a $M_w = 7.3$ earthquake occurred near Landers on June 28th, 1992. These dates ranged from August

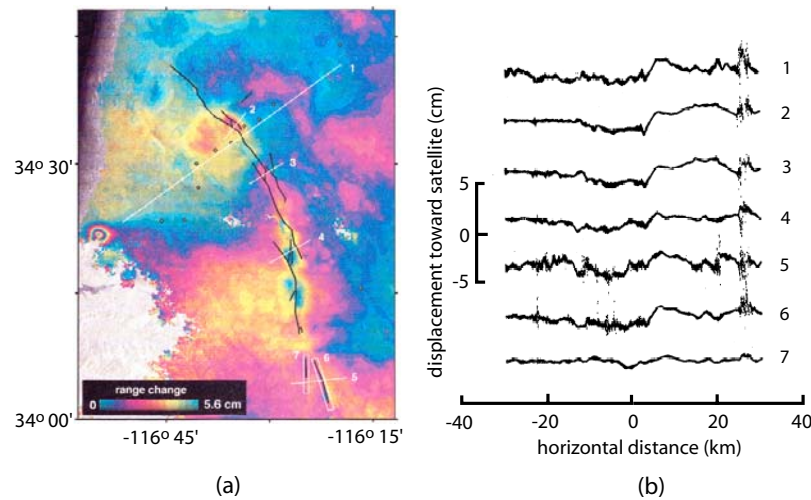


Figure 1.1 (a): InSAR image (Peltzer et al. (1998)) formed from two radar observations of Landers, California on September 27, 1992 and January 23, 1996. The image shows ground displacement in the line-of-sight of the radar. The transect labeled 1 is an 80 km profile spanning the fault shown in black. The yellow diamonds indicate locations of GPS stations. (b): Transects from seven InSAR images acquired along the location indicated by Profile 1 in (a). These seven images were formed from 10 radar observations over Landers, California from August 7, 1992 to March 19, 1997

7, 1992 to March 19, 1997. The patterns in Figure 1.1(a) show post-seismic ground displacement in the line-of-sight of the radar. The authors extracted many 80 km profiles along transect 1 from the seven images they processed. These profiles are shown in Figure 1.1(b). Profile 3 in Figure 1.1(b) was obtained from the image shown in Figure 1.1(a). The authors observe that ground displacements obtained from the InSAR profiles generally show uplift in regions east (positive horizontal distance) of the fault (indicated by the black line in Figure 1.1(a)) and subsidence west (negative horizontal distance) of the fault. The authors also note that the large bumps in Profiles 2 and 3 in Figure 1.1(b) are not due to post-seismic ground displacements but instead is most likely caused by water vapor effects on the InSAR observations. This example shows that atmospheric water vapor introduces distortions in InSAR images and these distortions are comparable in magnitude to signatures due to crustal motion.

Several authors such as Zebker et al. (1997) and Hanssen et al. (1999) have used InSAR images to observe water effects directly. In these studies, the authors formed InSAR images

from radar observations acquired one day apart, thus minimizing the contribution of target motion on the observations. Figure 1.2(a) shows an InSAR image formed by Hanssen et al.

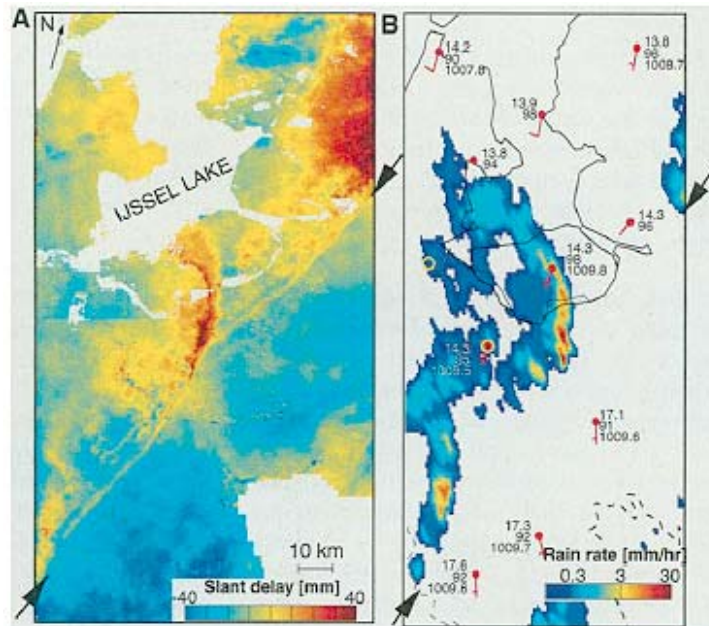


Figure 1.2 (a): InSAR image (Hanssen et al. (1999)) formed from 1-day repeat pass radar observations of the Netherlands. The image measures radar signal delay difference, in mm, due to water vapor distribution in the atmosphere on both dates. The diagonal band indicated by the arrows suggests a precipitating cold front propagating from the northwest (b): Weather radar image acquired on both dates and surface meteorological measurements (temperature in Celcius, percentage relative humidity and pressure in hectopascals). Also shown are surface wind measurements where half wind barb corresponds to 2.5 m/s and a full barb to 5 m/s.

(1999) from two radar observations of the Netherlands on October 3 and 4, 1995. The InSAR image measures the radar signal propagation delay difference, expressed in mm, due to water vapor distribution in the neutral atmosphere on both those dates. In Chapter 4, we will explain this delay in greater detail. The author compared this InSAR image with a weather radar image as well as surface meteorological observations, as shown in Figure 1.2(b). The author concluded that the narrow diagonal band observed in the image is most likely due to a precipitating cold front propagating from the northwest.

In Figure 1.3, we show a sequence of InSAR images of Hawaii formed by Zebker

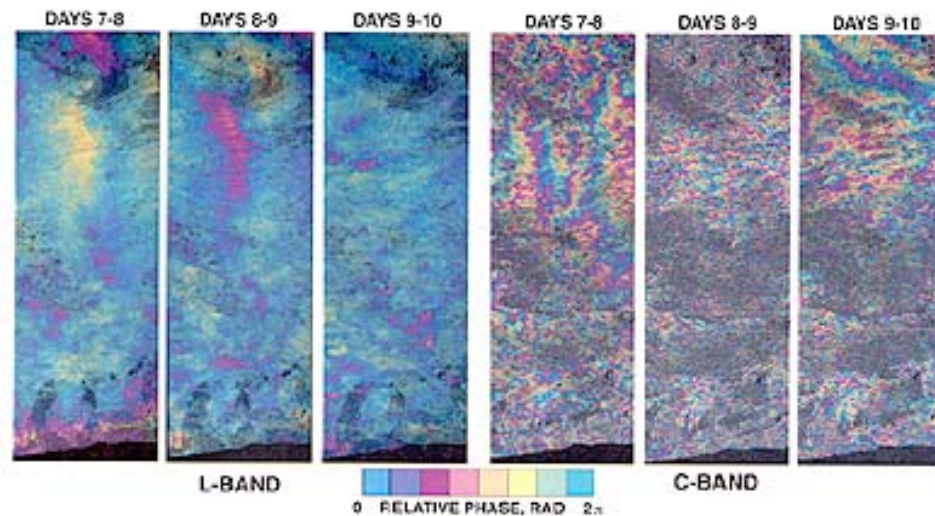


Figure 1.3 InSAR images (Zebker et al. (1997)) from a sequence of radar observations acquired on 4 successive days (October 7-10, 1994). Radar observations were acquired at two frequencies, C-band and L-band

et al. (1997) from 1-day radar observation pairs. The radar observations were acquired at L-band (24 cm wavelength) and C-band (5 cm wavelength) frequencies. The images show spatial and temporal variations in the phase of radar echoes (see Chapter 3 for further detail on the InSAR technique) due to water vapor variations in the neutral atmosphere. The authors note that the ratio of phase artifacts in the L-band and C-band images is equal to the wavelength ratio, supporting the observation that the neutral atmosphere is nondispersive at these frequencies.

The examples in Figures 1.2 and 1.3 indicate that atmospheric water vapor affects InSAR observations. The images above were formed from radar observations available at short (1-day) time intervals, thereby minimizing the effect of ground motion on the observations. In studies of crustal deformation, however, InSAR images are generated from radar observations often spaced months or years apart and water vapor effects generally corrupt signatures due to ground motion (Figure 1.1, for example). Thus, as a practical issue, it is important to mitigate the effects of water vapor in InSAR observations to increase the accuracy of estimated displacement velocities. This problem is the main motivation for this dissertation. In the following chapters, we will present methods for correcting

water-vapor-induced artifacts in InSAR observations using timeseries measurements from GPS.

1.1 Objectives

We focus on the temporal and spatial water vapor “noise” component in, respectively, GPS timeseries observations acquired from a receiver network and an InSAR image of the same area. Our primary objective of this work is to reduce water-vapor-induced delay distortions in InSAR images using timeseries measurements of water-vapor-induced signal delay obtained from a sparse network of GPS receivers. Specifically, we use the GPS observations to estimate maps of signal delay which we then subtract from the InSAR distortions, thereby in principle allowing smaller magnitude ground motion signals to be detected.

As will be explained in Chapter 3 and Chapter 4, these GPS-derived maps of signal delay are related to the spatial distribution of total overlying water vapor in the area containing the GPS network. To convert these maps to absolute quantitative spatial measurements of total column water vapor, additional meteorological measurements are required. In particular, surface pressure and temperature observations are needed to, respectively, correct the maps for long-wavelength variations that are independent of water vapor and to compute a scaling factor that converts signal delay in millimeters to total column water vapor with units of kg/m^2 . However, the fluctuations of water vapor content in the neutral atmosphere, relative to the variation of other meteorological variables, are the primary source of variations of the error component in GPS and InSAR observations. Thus, we focus here on reproducing the spatial variations of distortions observed in the InSAR image from delay fluctuations over time from GPS. The estimated maps show spatial variations that are due primarily to atmospheric water vapor, and these maps can later be converted to total column water vapor maps given additional meteorological data which vary slowly in space and time compared to water vapor.

A fundamental problem that we address in meeting our objective is to estimate total column water vapor maps at the resolution of InSAR using GPS measurements acquired at only a few, sparsely-distributed locations in the imaged area. Several authors (Williams et al. (1998), Hanssen (1998), Li et al. (2006)) have suggested calibrating atmospheric

artifacts in InSAR observations using GPS measurements. While calibration using GPS is recommended because atmospheric water vapor similarly affects both GPS and InSAR measurements, these authors note that the low spatial density of GPS networks limits their effectiveness in reproducing the high spatial variability of water vapor effects in InSAR data.

We overcome this sampling problem in two steps. First, we characterize the distortions in GPS and InSAR measurements according to two physical mechanisms of water vapor spatial variability, namely the vertical-stratification of humidity in the atmosphere and the horizontal fluctuations caused by turbulent mixing of water vapor. These two models of water vapor variability constrain the estimated signal delay maps from the spatially-sparse GPS measurements. We separately estimate from the sparse GPS data a map showing variability caused by the vertical-stratification of water vapor in the neutral atmosphere as well as another map approximating variability caused by turbulent mixing of moisture.

In the second step, we increase the effective density of GPS observations by leveraging its dense time sampling of water vapor. We use additional observations measured by GPS before and after the InSAR acquisition times to improve the estimation of total column water vapor maps. In doing so, we assume that the effects of water vapor in GPS and InSAR observations are dynamic in nature. In particular, we consider dynamic models in which total column water vapor is transported and dispersed by wind. The timeseries measurements of water-vapor-induced delay fluctuations from GPS then track, albeit at only a few locations spatially, this dynamic atmosphere. Based on this idea, we develop algorithms that allow us to incorporate the time-dependence of GPS measurements to improve the estimation of the distortions in the InSAR image. This idea is supported by the results of some authors (e.g. Wadge et al. (2002)) who have shown that high-resolution numerical weather models can be used to predict the spatial distribution of water vapor, and consequently of InSAR water-vapor-induced distortions, from meteorological measurements acquired earlier.

1.2 Contributions

In this work, we have used data from a network of GPS receivers to evaluate the effect of water vapor on InSAR measurements. We have investigated the degree to which these effects can be removed through calibration using the GPS data. The specific contributions of this dissertation are as follows:

- (1) We demonstrate how a sparse collection of GPS measurements acquired only at the radar image acquisition instances can generate maps proportional to total column water vapor that approximate: (i) topography-dependent InSAR atmospheric distortions caused by vertical-stratification of the neutral atmosphere and (ii) shorter-scale InSAR distortions resulting from the turbulent mixing of water vapor in the atmosphere. We show that both these maps reduce the level of phase distortion in radar interferograms with variations primarily due to the atmosphere.
- (2) We develop two algorithms that use estimates of vertically-integrated wind to incorporate additional measurements from GPS acquired before and after the radar image acquisition instances in the estimation of maps proportional to total column water vapor. These maps better reduce the distortions in the radar interferograms compared to corresponding maps generated using only GPS data acquired at the radar image acquisition instances. The first algorithm uses statistical interpolation of a network of control points with greater spatial density than is suggested by the configuration of GPS receivers. This denser network is formed from GPS measurements acquired around the radar acquisition instances. The second algorithm produces a map proportional to total column water vapor from GPS measurements acquired from a sparse network by using a deterministic transport model for water vapor.
- (3) We develop two algorithms to estimate vertically-integrated wind over time from ZWD timeseries sparsely measured by a GPS network. The first algorithm is based on the statistics of a cloud of turbulently-mixed water vapor moving over the area containing the GPS network under the action of mean wind. The second algorithm is deterministic and is based a physical model of water vapor transport by spatially-variable, vertically-integrated two-dimensional wind fields.

1.3 Outline

Chapter 2 presents some background on water vapor in the atmosphere. We also mention conventional remote sensing techniques for measuring water vapor and discuss briefly the significance of water vapor in meteorological studies.

A brief overview of the GPS and InSAR techniques is presented in Chapter 3. The observations from both these instruments are a sum of contributions from many different processes. Through appropriate processing of these data, we present temporal and spatial measurements of neutral atmospheric signal delay derived from the GPS and InSAR observations, respectively.

Chapter 4 explains the relationship between meteorological quantities and delay measurements in GPS and InSAR. As we are primarily interested in signal fluctuations over space and time, we then characterize the variations in GPS and InSAR according to the effects of: (1) vertical-stratification of the neutral atmosphere, and (2) turbulent-mixing of water vapor. In this chapter, we also present an overview of existing approaches and related work by other authors to reduce atmospheric distortions in InSAR images.

In Chapter 5, we show results of reducing the atmospheric distortions in the InSAR image presented in Chapter 3 using the GPS measurements acquired only at the radar acquisition time instances. In particular, we use these sparse GPS measurements to estimate a map approximating variations due to the vertical-stratification of the neutral atmosphere and another map approximating the fluctuations caused by turbulent mixing of water vapor.

We present an algorithm in Chapter 6, which we call the “frozen-flow” algorithm, that uses GPS measurements acquired before and after the radar image acquisition instances to improve the estimation of that component of InSAR atmospheric distortions due to the turbulent-mixing of water vapor. The frozen-flow algorithm assumes a statistically-stationary field of water vapor that is transported across the imaged domain by mean wind. Based on this assumption, our algorithm produces a network of GPS measurements that is spatially denser than suggested by the distribution of GPS receiver network. With more point measurements available, we interpolate signal delay maps - proportional to total column water vapor - that better reduces InSAR atmospheric distortions as compared to corresponding maps generated using only GPS measurements acquired at the radar image

acquisition times.

Chapter 7 presents another algorithm that estimates maps showing variations caused by the turbulent mixing of water vapor from GPS timeseries measurements. This algorithm is based on a physical model for 2D transport of water vapor in the atmosphere that generalizes the frozen-flow transport model in Chapter 6. Instead of interpolating dense networks of GPS measurements acquired before and after the radar image acquisition times, we estimate maps of signal delay as solutions to an inverse problem of fitting the water vapor transport model to timeseries measurements acquired from the GPS network. We demonstrate that this algorithm also produces maps of signal delay that results in a greater reduction of InSAR atmospheric distortions than corresponding maps generated using only GPS data acquired at the radar image acquisition times.

In Chapter 8, we present results from a case study where we apply these techniques to another GPS-InSAR dataset. We present our conclusions in Chapter 9.

Chapter 2

Water vapor in the atmosphere

Water vapor constantly circulates in the atmosphere, and is present even in otherwise clear skies. Water vapor is primarily found in the troposphere, which is the lowest 10-12 kilometers of the atmosphere. In fact, nearly one half of total water vapor in the atmosphere is found between sea level and 1.5 km. Less than 5-6% of water vapor is found above 5 km and less than 1% is found in the stratosphere (> 12 km) (AGU (1995)). The troposphere contains 80% of the Earth's total atmospheric mass and, in this layer, water is present in all three phases: ice, water and vapor. In the troposphere, temperature decreases at an approximate rate of 6.5°C per vertical kilometer. This implies that water vapor is primarily concentrated near the surface of the Earth because warmer air can sustain more water vapor than colder air.

In Figure 2.1, we illustrate the different layers in the atmosphere. In this work, we focus on water vapor in the neutral or non-ionized portion of the atmosphere, which comprises primarily the troposphere and stratosphere. Water vapor influences global climate in two ways: (1) it plays a fundamental role in Earth's hydrological cycle and (2) it is the dominant greenhouse gas in the atmosphere. The hydrological cycle describes the movement of water, in all three phases, between the land, ocean and atmosphere. Solar heating evaporates water vapor from the surface and, once in the air, water vapor is transported by wind and moves quickly through the atmosphere. This cycle is completed when water vapor condenses to form clouds and subsequently returns to Earth as rain. The distribution of water vapor in the atmosphere is intimately coupled with the distribution of clouds and

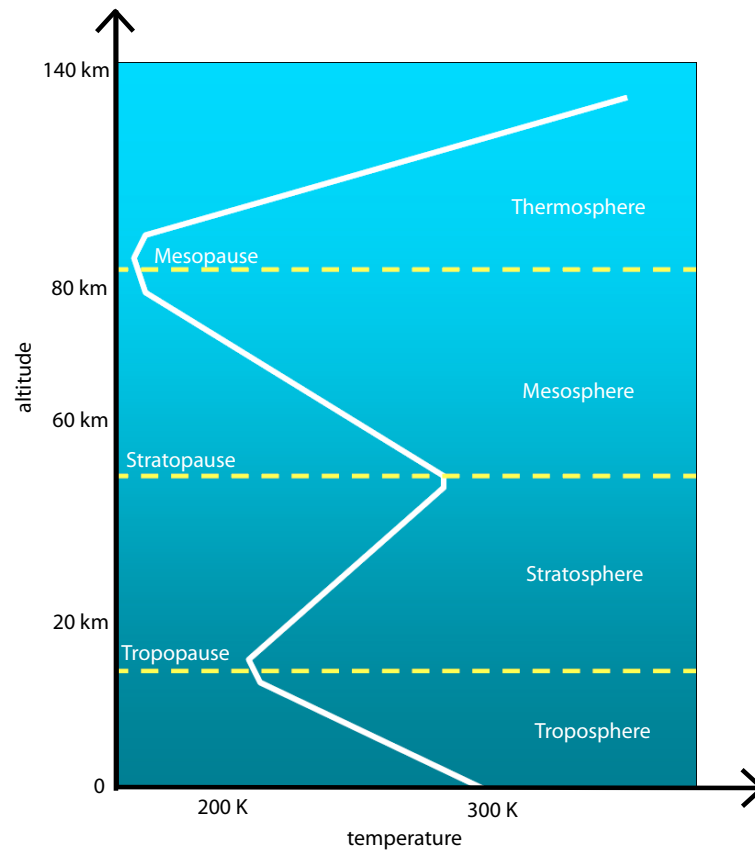


Figure 2.1 Layers of the atmosphere

rain (Bevis et al. (1992)). Water vapor has a large latent heat associated with its change of phase. Thus, as water vapor is transported by wind, latent heat is effectively redistributed in the atmosphere. Upon condensation, this latent energy is converted to sensible heat and this represents a major source of energy for circulation systems associated with the weather and climate.

Water vapor also impacts global climate through its role as the primary greenhouse gas. Greenhouse gases are transparent to much of the Sun's shortwave radiation but absorb or trap longwave radiation emitted by the Earth's surface. Without water vapor, surface air temperature on Earth would be well below freezing (AGU (1995)).

Water vapor is one of the most variable constituents in the atmosphere (Hanssen (1998))

and concentrations of moisture vary over a large range of spatial and temporal scales. Accurate characterization of the variability of water vapor is essential for climate studies and numerical weather prediction models. The accuracy of these models in forecasting short term weather is limited by the lack of observations of water vapor at short temporal and spatial scales. The need for high-resolution observations follows from that the variability of water vapor in the atmosphere, which cannot be adequately predicted using ground-based measurements of humidity alone. In particular, quantitative precipitation forecasting (QPF) is affected by the lack of mesoscale (< 100 km) moisture observations. Improving QPF requires water vapor observations at high spatial (< 20 km in the horizontal and < 200 meters in the vertical) and temporal (< 1 hour) resolutions (Weckwerth et al. (1999)). It is also important to measure water vapor in the presence of clouds due to its close relationship with precipitation.

Atmospheric water vapor is conventionally measured either from the ground using *in situ* devices such as radiosondes or from space using satellite passive remote sensing systems such as microwave radiometers and infra-red (IR) sensors. Radiosondes are balloon-borne instrument packages that measure pressure, temperature, humidity and wind at fine vertical resolution. Figure 2.2 shows an example of a relative humidity measurement acquired from a radiosonde launched from the Oakland airport in Northern California in 2002. We observe from this figure the fine-scale vertical moisture distribution in the troposphere, as measured by the radiosonde. Radiosondes, however, cannot measure the short-scale horizontal variations of water vapor. Also, the relative high-cost and labor intensive nature of setting up the instrument restricts launches to typically twice daily (Bevis et al. (1992)). Consequently, radiosondes cannot observe the temporal variability of atmospheric water vapor at time scales shorter than half a day.

Satellite-based passive remote sensing instruments can observe water vapor over large spatial scales. Passive systems infer water vapor distribution by measuring the amount of upwelling microwave radiation from the Earth absorbed by moisture in the atmosphere, direct observation of thermal emission of water vapor at microwave frequencies or by observing the attenuation due to water vapor of near-IR solar radiation reflecting off Earth's surface and clouds. Figure 2.3 shows a map of total column precipitable water (PW) over Southern California and the Pacific Ocean as measured by a microwave radiometer on

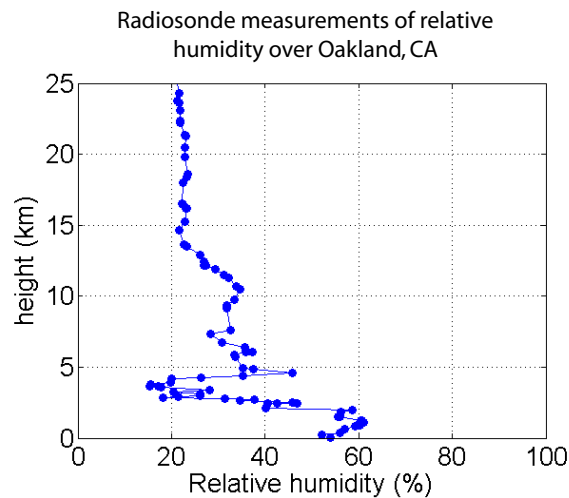


Figure 2.2 High vertical resolution measurements of relative humidity from a radiosonde launched from the Oakland International Airport, CA

board NASA's Aqua satellite platform. PW is the amount of vertically integrated water vapor and can be expressed as the height of an equivalent column of liquid water (Bevis et al. (1992)). The spatial resolution of these observations is about 50 km. We see that microwave radiometers, in contrast to radiosondes, can measure atmospheric moisture horizontally over large spatial scales. Also, retrievals of water vapor from microwave radiometers are complicated by the difficulty in characterizing the high variability of temperature over land (Bevis et al. (1992)). Thus, water vapor observations from these instruments are more useful over ocean than land.

Space-borne near-IR sensors, such as the MODIS instrument, have recently been shown to measure water vapor distribution at higher resolution (1 km) (Gao and Kaufman (2003)). Since such sensors measure the attenuation of reflected solar radiation, water vapor observations can only be provided over an area during daylight. Furthermore, the presence of clouds degrades the quality of moisture retrievals (Li et al. (2005)).

With the rapidly expanding number of GPS satellites and low earth orbiting (LEO) satellites equipped with GPS receivers in recent years, an active remote sensing technique called microwave limb sounding has proven to yield profiles of humidity at high vertical

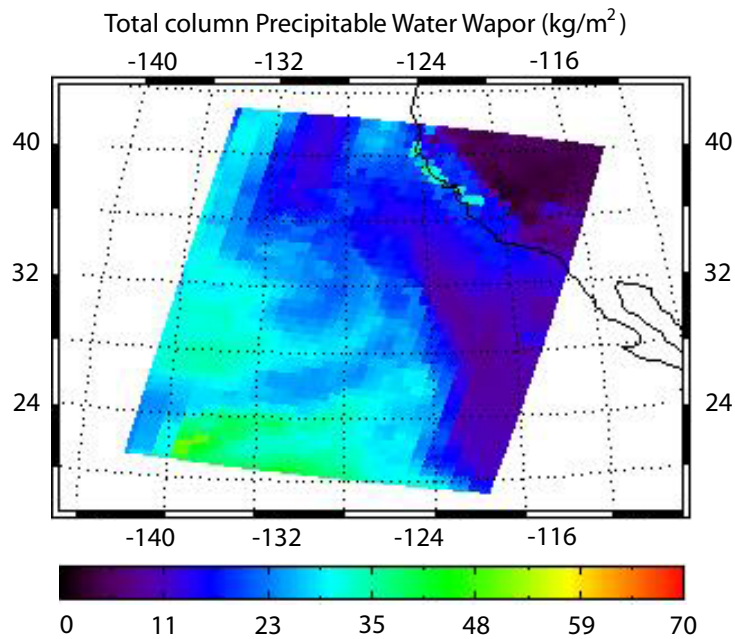


Figure 2.3 Measurements of total column water vapor over Southern California and the Pacific Ocean from a spaceborne microwave radiometer (AIRS). The spatial resolution of observations is 50 km

resolution. Atmospheric limb sounding relies on the radio occultation technique (Kursinski et al. (1997)). By measuring the amount of bending in the path of ray transmitted from a GPS satellite to an LEO receiver, atmospheric parameters such as temperature and water vapor quantity can be retrieved as a function of height. Figure 2.4 show vertical profiles of temperature and humidity retrieved from the CHAMP experiment (Wickert et al. (2001)).

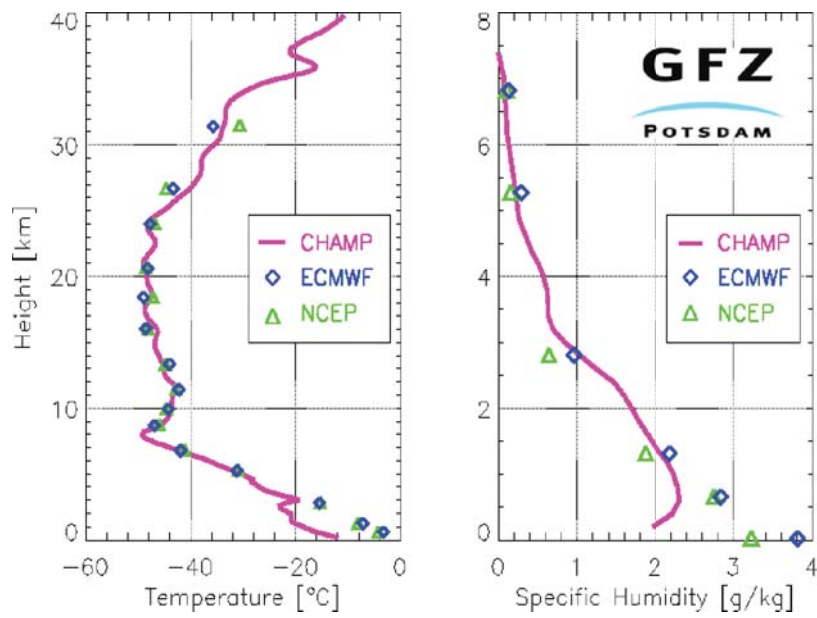


Figure 2.4 Vertical profiles of temperature in Kelvin and specific humidity in g/kg retrieved from the CHAMP experiment. These profiles are compared with results from meteorological analyses.

Chapter 3

GPS and InSAR

3.1 Introduction

Our primary objective is to estimate maps proportional to water vapor content from GPS measurements and to use these maps to compensate water-vapor-induced distortions in InSAR observations. In this chapter, we first present an overview of GPS followed by a brief description of InSAR. Our aim here is to show that the primary observable from GPS and InSAR, the carrier phase, contains a component due to signal propagation in the neutral atmosphere. The phase of this neutral atmospheric component is our “signal” of interest because it is proportional to the line-of-sight integrated atmospheric water vapor. However, the phase observables from GPS and InSAR are generally a superposition of phase components due to several physical processes including neutral atmospheric signal propagation. In this chapter we describe how we estimate the neutral atmospheric component from the GPS and InSAR observables. We then show timeseries measurements of neutral atmospheric propagation effects estimated from raw data acquired from a GPS network. We also present an InSAR image of the same area showing distortions caused by the neutral atmosphere. In the following chapters, we will present algorithms for estimating maps from these GPS measurements which we then use to correct the distortions observed in the InSAR image.

3.2 Global Positioning System

The Global Positioning System (GPS) is a widely used tool for making very precise geodetic measurements. In GPS, the position of a receiver on the ground is inferred from measurements of distance between the receiver and at least four GPS satellites in view.

Since July 1992, there have been 24 satellites in the GPS constellation, orbiting the Earth at an altitude of approximately 20,000 kilometers and with an orbital period of 12 hours. This configuration provides continuous coverage of any point on the globe by at least four satellites.

The GPS satellites transmit coded messages modulated on two carriers at frequencies $f_1^{GPS} = 1.57542$ GHz ($\lambda_1^{GPS} = 0.19$ meters) and $f_2^{GPS} = 1.2276$ GHz ($\lambda_2^{GPS} = 0.24$ meters). These two frequencies are called *L1* and *L2*, respectively. Three codes in total are transmitted, two of which (“C/A” and “P”) are pseudorandom number (PRN) sequences unique to each satellite and are used to infer receiver-satellite distances. The third code contains information on satellite health, position, onboard clock and the positions of other satellites in the constellation. The accuracy of distances, or *ranges*, inferred from these codes is insufficient for high-precision geodetic applications, therefore, GPS signal carrier phase is typically tracked to achieve sub-centimeter positioning accuracy.

GPS receivers track the carrier phase of signals using a delay-lock loop. Relative motion between the satellite and the receiver on the ground shifts the received signal in frequency by the *Doppler effect*. The GPS receiver determines the phase by mixing the received, Doppler-shifted, signal with a local replica of the transmitted waveform. The difference, or “beat”, frequency component of the mixed signal is then integrated to give the phase from which range to the satellite can be inferred. The distance ρ^k to GPS satellite k expressed as cycles of carrier phase is

$$\rho^k = \lambda N^k + \phi^{GPS,k} \quad (3.1)$$

where N^k is an unknown integer number of cycles corresponding to the range to satellite k when the receiver first locked on to the transmitted signal. ϕ^{GPS} is the GPS phase, expressed as length via scaling by $\lambda/(2\pi)$, from the k -th satellite carrier signal. For high-precision positioning, the unknown integer ambiguity N must be resolved.

While the carrier phase observables can provide distance measurements to the GPS satellites, the satellite orbits must be known precisely so that the position of the receiver on the ground can be inferred. Describing the positions and velocities of points on the ground requires a well-defined reference frame or coordinate system that is fixed to the solid Earth. The terrestrial reference frame currently used in geodesy is the International Terrestrial Reference Frame (ITRF). In contrast, an inertial coordinate system, fixed with respect to stars, is typically used to describe satellite orbits. To convert between these two coordinate systems, effects such as Earth rotation, precession and nutation of the planet's axis as well as polar motion must be accounted for.

High-precision satellite orbits are computed from analyses of observations collected at a network of ground tracking stations whose locations are known accurately a priori. The ground tracking station positions are also used to define the ITRF. The International GPS Service for Geodynamics (IGS) (<http://igsceb.jpl.nasa.gov/>) is composed of a global network of tracking stations and routinely provides high-precision GPS ephemerides (orbits), satellite clock information and ionospheric information. In addition, IGS also provides earth rotation parameters which are used to convert between satellite inertial and Earth-fixed reference frames. In this work, we use estimates of orbits, clocks and earth orientation obtained from IGS to process GPS data.

The observed GPS carrier phase, at L1 or L2 frequencies, consists of a superposition of several components, and is expressed as path length in units of meters via scaling by $\lambda/(2\pi)$:

$$\phi^{GPS,k} = \rho^k + c(\Delta t_{clock}^k - \Delta t_{clock}) + \phi_{iono}^{GPS} + \phi_{NA}^{GPS} - \lambda N^k + \phi_{errors}^{GPS} \quad (3.2)$$

In the above, $\phi^{GPS,k}$ denotes the carrier beat phase measured over time by the GPS receiver from a signal transmitted from the k -th GPS satellite. The k -th satellite and receiver clock offsets, which translate to equivalent path length errors by multiplication with the speed of light c , are denoted as Δt_{clock}^k and Δt_{clock} respectively. ϕ_{iono}^{GPS} represents a contribution due to signal propagation in the ionosphere while ϕ_{NA}^{GPS} is the contribution due to propagation in the neutral atmosphere. The phase error term, ϕ_{errors}^{GPS} , incorporates the effects of orbit inaccuracies, signal multipath and receiver antenna phase center variations.

Depending on the application, one term in Eq. (3.2) above is the signal of interest while the other terms are regarded as errors. In this work, we are primarily interested in the neutral atmospheric propagation component, ϕ_{NA}^{GPS} . Hereafter, we shall refer to this component as *neutral atmospheric delay*, for reasons that will be given in Chapter 4. Therefore, the other terms in Eq. (3.2) need to be accounted for accurately so that the measured GPS carrier phase yields the neutral atmospheric delay.

The k -th satellite-receiver geometric range ρ^k is related to receiver position \mathbf{x} as follows

$$\rho^k = \| \mathbf{R}\rho_S^k - \mathbf{x} \| \quad (3.3)$$

where ρ_S^k denotes the position of the k -th GPS satellite in an inertial frame while the rotation matrix \mathbf{R} transforms the orbits to the terrestrial reference frame in which receiver position \mathbf{x} is defined. This rotation matrix incorporates the effects of diurnal planet rotation, precession, nutation and polar motion. Here, we use the high-precision IGS estimates of satellite orbits and Earth orientation parameters. Also, in this work, the GPS receiver positions \mathbf{x} are known a priori as the receivers used in this study are part of the SCIGN permanent network of GPS stations installed to measure cm-sized displacements due to crustal motion. The error in the a priori receiver positions is typically less than half a meter. This accuracy is sufficient to linearize Eq. (3.3) and solve for a correction to the a priori receiver positions from the GPS observables.

The ionospheric component, ϕ_{iono}^{GPS} , can be removed by forming a linear combination of the measurements at the two GPS frequencies, L1 and L2. This is possible because the ionosphere is a dispersive medium and thus ϕ_{iono}^{GPS} is frequency dependent. The contribution due to satellite clock errors, $c\Delta t_{clock}^k$ is minimized because we use here high-precision (accuracy less than 3 cm, see <http://igsch.jpl.nasa.gov>) clock information is from IGS.

The GPS data used in this work were processed using the GIPSY/OASIS-II software originally developed at the Jet Propulsion Laboratory (JPL) (Zumberge et al. (1997)). Using GIPSY, we estimate three quantities from the raw GPS carrier phase observables, after accounting for geometric range, ionospheric phase and satellite clock offsets as mentioned above. These three unknowns are: (1) a small correction to the a priori guess for receiver position, \mathbf{x} , (2) receiver clock offsets $c\Delta t_{clock}$ and (3) *zenith neutral atmospheric delay*,

$\phi_{NA}^{GPS,z}$. Zenith neutral atmospheric delay (ZND) is the phase shift caused by signal propa-

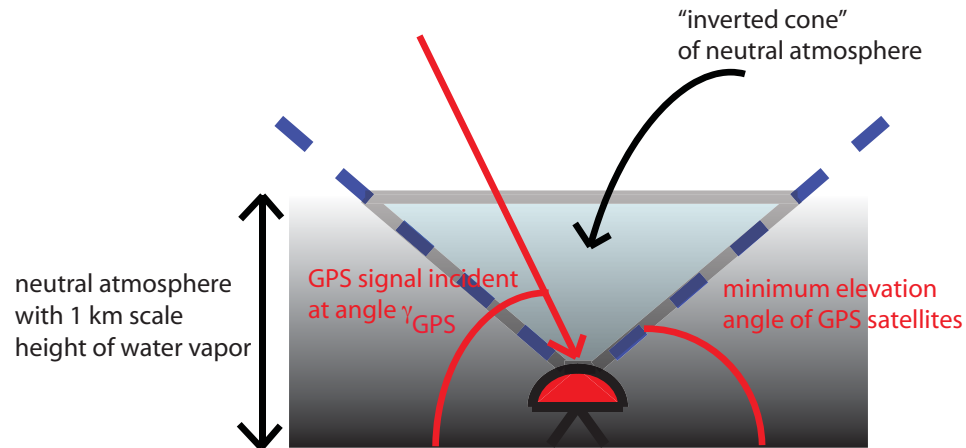


Figure 3.1 The “cone-averaging” effect in GPS. A receiver on the ground records GPS signal carrier phase observed at elevation angles above a minimum cut-off, typically 15° . As the GPS satellites fly over the ground, the volume of neutral atmosphere through which the GPS signal propagate is approximately conical, with the vertex fixed at the receiver on the ground

gation in the neutral atmosphere and incident on the receiver in the zenith direction. GPSY estimates ZND by computing a weighted average of carrier phase observations recorded over many elevation angles γ as the GPS satellites fly over the receiver on the ground. The specific weighting, or *mapping*, function used is the Neill mapping function (Neill (1996)). Thus, ZND measures the net effect of a volume of neutral atmosphere above the receiver through which the GPS signals at various incidence angles propagate, as shown schematically in Figure 3.1. This figure shows a conical volume above a GPS receiver on the ground. This cone is defined by the elevation of angles of satellites transmitting to the receiver. Typically, the minimum elevation angle at which signals are received is set to 15° . The figure also shows a layer of neutral atmosphere with a 1 km scale height and, due to the observation geometry, the received GPS carrier phase is sensitive to neutral atmospheric effects within this cone.

ZND represents the total signal delay caused by a mixture of dry gases and water vapor in the neutral atmosphere, which slightly increases the refractive index of the propagation medium from unity, the free space value. As a result, the propagation velocity of the

electromagnetic waves in the neutral atmosphere decreases (Zebker et al. (1997)) and the time taken for the GPS signals to reach a receiver on the ground is slightly longer than implied by the satellite-receiver distance. These additional delays appear as phase shifts ϕ_{NA}^{GPS} in the GPS carrier phase observables. ZND is typically described as a superposition of two delay components: (1) hydrostatic delay and (2) delay due to atmospheric water vapor,

$$(\lambda/(2\pi))\phi_{NA}^{GPS,z} = l_{hyd}^{GPS,z} + l_{wet}^{GPS,z} \quad (3.4)$$

Hydrostatic delay is primarily due to dry gases in the neutral atmosphere while wet delay is solely caused by water vapor. Hydrostatic delay reaches about 2.3 meters in the zenith direction, is well-constrained by surface pressure measurements and varies slowly in both space and time (Bevis et al. (1992)). In contrast, wet delay magnitude is smaller (about 35 cm in humid regions) but its variability exceeds that of hydrostatic delay by an order of magnitude (Elgered et al. (1991)). In Chapter 4, we will discuss hydrostatic and wet delays in further detail. We mention this point of detail here because we use GIPSY to estimate only the water-vapor dependent component of ZND, the zenith “wet” delay (ZWD), while we fix the hydrostatic delay component to a nominal value of 2.1 meters. In particular, GIPSY models ZWD as a first-order Gauss-Markov (Lichten and Border (1987)) stochastic process

$$l_{wet}(t+1) = \alpha l_{wet}(t) + w(t) \quad (3.5)$$

where t denotes the sample time index and α is related to the drift rate and controls the amount of ZWD variation between time steps. In the above, $w(t)$ is an additive Gaussian white noise stochastic process.

In Figure 3.2(b), we show several timeseries of ZWD estimated from GPS data acquired from a network of 29 receivers. These receivers are part of the Southern California Integrated GPS Network (SCIGN) operating in the greater Los Angeles metropolitan area, and provide coverage for crustal motion studies in Southern California. The locations of receivers in this network are shown in Figure 3.2(a). The average spacing of receivers in this network is about 12 km. We computed a 24-hour timeseries ZWD, for each GPS site, on two dates corresponding to dates of SAR image acquisition (see below for a discussion on SAR), sampled every 5 minutes. We note that, here, we use $\alpha = 9.8 \times 10^{-8}$ km/ \sqrt{s} as

the drift rate in the stochastic estimation of ZWD.

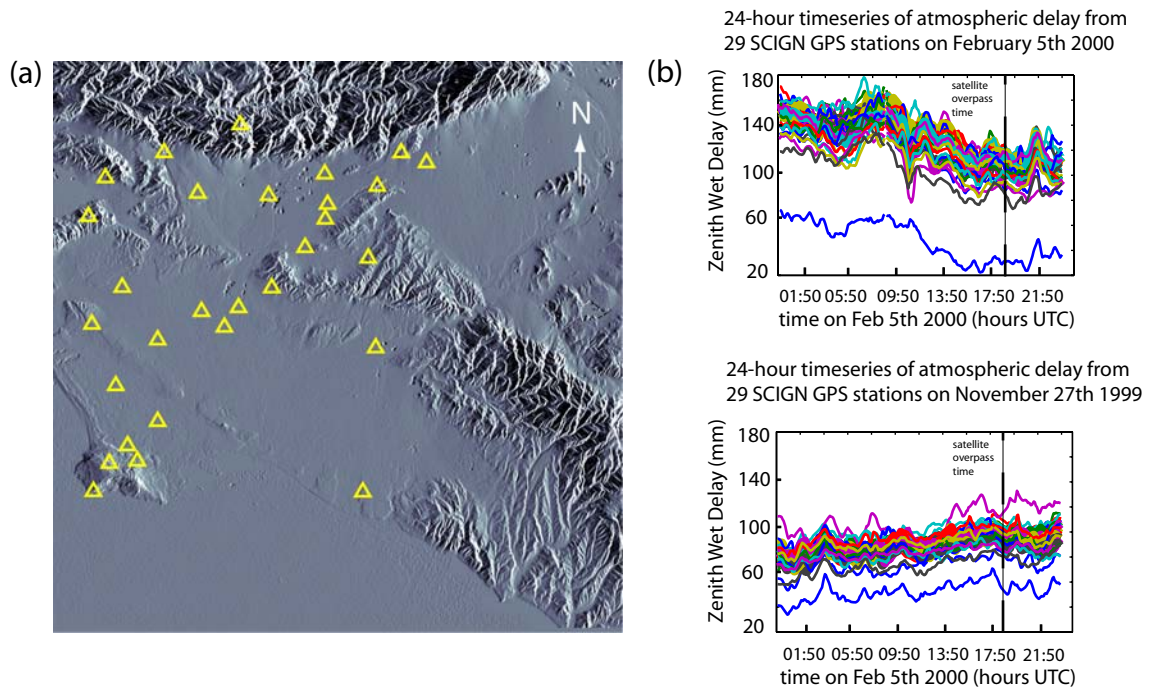


Figure 3.2 (a): Shaded relief map of the Los Angeles/Orange County basin. Yellow triangles indicate locations of SCIGN GPS receivers. (b): 24-hour timeseries of Zenith Wet Delay (ZWD) from 29 SCIGN continuous GPS receivers for February 5th, 2000 (top) and November 27th, 1999 (bottom). The dashed vertical line in each plots indicates the time when radar observations over Southern California were acquired

Estimates of ZWD derived from GPS observations are susceptible to several types of errors, including (1) biases due to deviations of hydrostatic delay $I_{hyd}^{GPS,z}$ from the nominal value we assumed, (2) unmodeled signal multipath and antenna phase center variation effects and (3) limitations in the assumption of equal mapping functions for both wet and hydrostatic delays. We minimize these last two error sources by only using GPS carrier phase observations recorded from satellites at elevation angles γ greater than 15° (Segall and Davis (1997), Li et al. (2005)).

parameter	value
radar frequency	5.3 GHz (C-band)
radar wavelength, λ	5.67 cm
pulse bandwidth	15.55 MHz
pulse repetition frequency (PRF)	1679.9 Hz
sampling frequency, f_s	19.2 Mhz
orbital altitude, H_{alt}	790 km
orbit repeat time	35 days
look angle, θ	$21^\circ - 26^\circ$
swath width	100 km
spacecraft velocity, V_{SAR}	7.5 km/s

Table 3.1 Parameters of the ERS-1 and ERS-2 imaging radar systems

3.3 InSAR

3.3.1 SAR

In synthetic aperture radar, a side-looking radar mounted on a satellite platform illuminates a swath of ground repeatedly, at a rate denoted the pulse repetition frequency (PRF), with pulsed waveforms of electromagnetic radiation as the sensor moves at velocity V_{SAR} along its flight track, as depicted in Figure 3.3. In this work, we use SAR (and InSAR) observations acquired from a radar system onboard the European Remote Sensing (ERS) satellites. The wavelength of radiation used by the ERS radar is $\lambda = 5.67$ cm (C-band). The radar antenna beam pattern in the direction perpendicular to the flight track when projected on the ground defines the width of the imaged swath, typically 100 km. As the sensor moves along its flight track, the antenna beam pattern sweeps over the target area resulting in an imaged swath that is typically 100 km in length, as well. In Table 3.1, we show relevant ERS radar system parameters.

The transmitted radar signals scatter off natural and man-made objects on the ground. The SAR receives and samples (at a rate of f_s) these backscattered radar echoes. The samples are stored in complex format. The raw radar data, then, measure the amplitude and phase of backscattered energy from all scatterers in the illuminated area. The radar returns thus

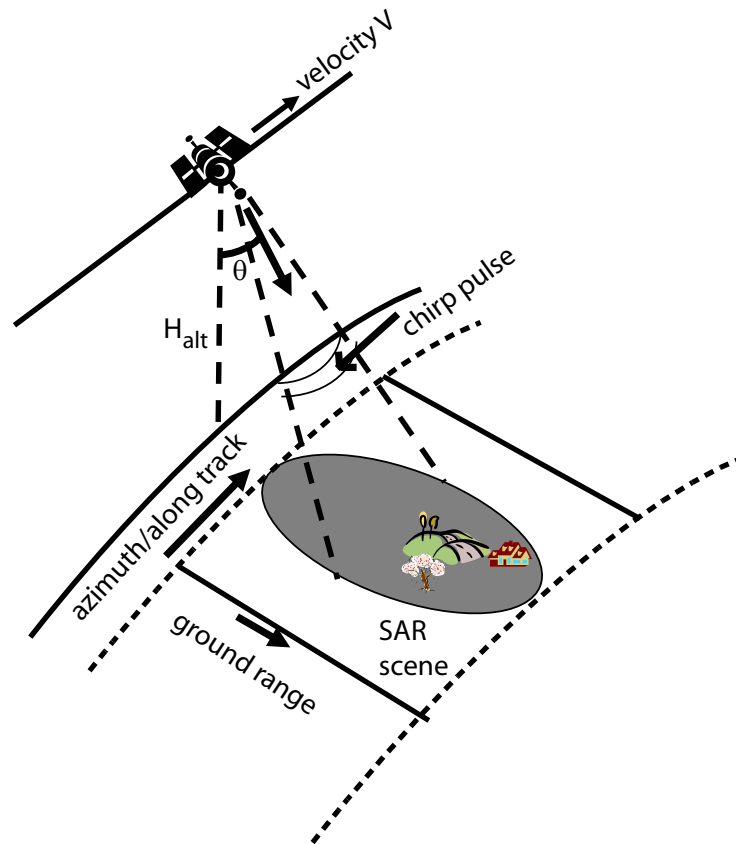


Figure 3.3 SAR imaging geometry. Spacecraft flies along a track at velocity V emitting linear-frequency modulated pulses at a rate of PRF. The orbital altitude is denoted H_{alt} . The coordinate system of the a SAR image is in terms of slant range (distance from transmitter to target on the ground) and azimuth

contain information on the position of scatterers relative to the SAR, electrical properties of the scatterers on the terrain below and the state of the neutral atmosphere and ionosphere along the propagation paths between the ground and the space-borne sensor.

Without matched filter processing, across-track, or *range*, radar resolution to discriminate targets on the ground is proportional to the width of the transmitted pulse. For ERS, this is approximately 5 kilometers. The resolution in the along-track, or *azimuth*, direction before SAR processing depends on the antenna beamwidth, and is also approximately 5 kilometers.

In SAR systems, high range resolution is often achieved by using a linear-frequency modulated waveform to increase the bandwidth of the transmitted pulse. By processing the received echoes with a matched filter tuned to the transmitted waveform, the range resolution improves to less than 10 meters for ERS. A similar procedure is adopted to increase resolution in the azimuth direction. Here, the replica or reference function used in the matched filter is generated based on Doppler frequency shifts of echoes from successive pulses that illuminate the same point on the ground as the satellite flies along its track. The Doppler effect in the received echoes arises because of the relative motion between the sensor and the ground. After applying the matched filter, the azimuth resolution for ERS is around 5 meters. Thus, the fine azimuth resolution results from synthesizing a much larger aperture, compared with the antenna size, by a Doppler-weighted linear combination of successive pulses illuminating a point on the ground.

A SAR image consists of a two-dimensional array of complex values in range and azimuth coordinates. Each element of the array, a *pixel*, has an amplitude and phase proportional to the random superposition of echoes from many scatterers within a resolution cell centered on that pixel. We note that, for ERS, the area on the ground defined by a pixel and a resolution cell is slightly different. The range pixel dimension is dependent on the sampling frequency f_s and is about 20 meters when projected onto the flat ground. The azimuth pixel dimension is given by $\frac{V_{SAR}}{PRF}$ and is about 4 meters. The size of a resolution cell, in contrast, is determined by the width of the impulse response of the SAR imaging system. As mentioned previously, the slant-range resolution for ERS is less than 10 meters while the azimuth resolution is 5 meters. When projected onto the flat ground, the resolution cell size is slightly larger than a pixel size. Typically, 5 azimuth pixels are averaged together - a procedure called “taking looks”- to give resulting pixels with square 20×20 meter dimensions.

Because of the random superposition of echoes from scatterers, the amplitude varies from pixel to pixel, displaying the speckle effect. The phase of each pixel is related to the to all scatterers within the resolution cell and additional *scattering phase* shifts caused by electromagnetic scattering of the incident radiation off the targets in that cell. Because of the random superposition of echoes from many targets in the cell, the net phase is uniformly distributed between 0 and 2π and phases from adjacent pixels are typically uncorrelated.

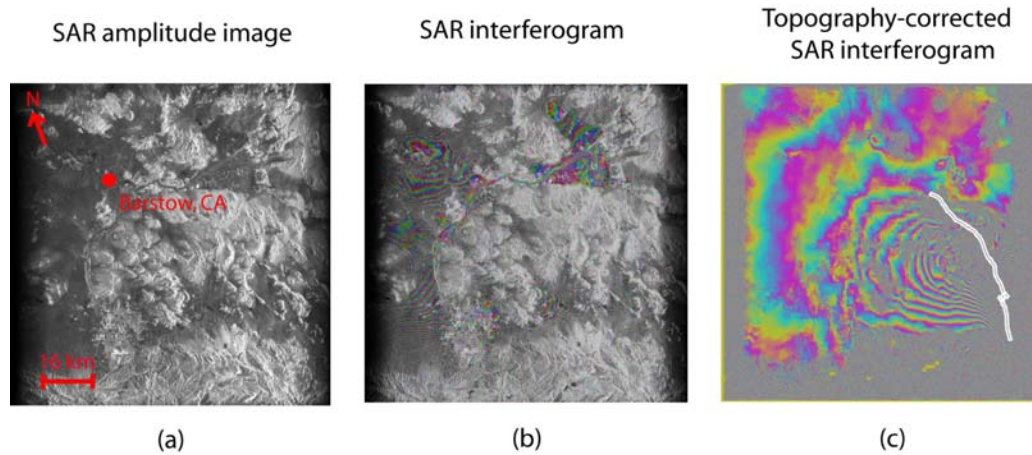


Figure 3.4 (a): SAR image over Landers, CA. The pixel spacing is about 90 meters, and the imaged swath is approximately $100 \text{ km} \times 100 \text{ km}$. (b): SAR interferogram over Landers, CA formed from two ERS-1 SAR observations on April 24th and September 11th, 1992. The perpendicular baseline between the two radar observations was about 800 meters. Here, one cycle of phase between 0 and 2π represents a height change on the ground of about 10 meters. (c): SAR interferogram with topographic phase ϕ_{topo}^{INSAR} removed using a Digital Elevation Model (DEM) of the area. The colored fringes show coherent movement of scatterers on the ground between the two SAR observation times. Here, a cycle of phase between 0 and 2π represents a range change of 2.86 cm

Figure 3.4 shows an example SAR image over Landers, California acquired from ERS-1 radar observations in April 24th, 1992. The ground pixel spacing in this image is about 90 meters and the variation in observed brightness is due to the terrain's reflectivity at the C-band wavelength used.

3.3.2 Interferometric SAR

The phase of a SAR resolution cell contains information on the path length between the sensor and that resolution cell on the ground. However, because of the random superposition of echoes from many scatterers in that cell, the net phase is effectively uniformly distributed. However, if a second SAR image was acquired over the same area, but from a slightly different viewing angle, the corresponding phase measured in that same resolution

cell would be nearly equal to the phase observed in the first image.

Therefore, in interferometric SAR (InSAR), two SAR images are acquired over the same area but from slightly different viewing geometries. InSAR results from repeat-pass SAR observations of the same area, whereby two SAR images of the same terrain are acquired by one satellite but at different times corresponding to multiples of the satellite's orbit period. The small difference in viewing angle arises because the satellite orbits do not repeat exactly. This viewing angle difference is quantified by the spatial separation of the antennas on each pass, and this separation distance is called the *interferometric baseline*. Figure 3.5 shows the InSAR imaging geometry.

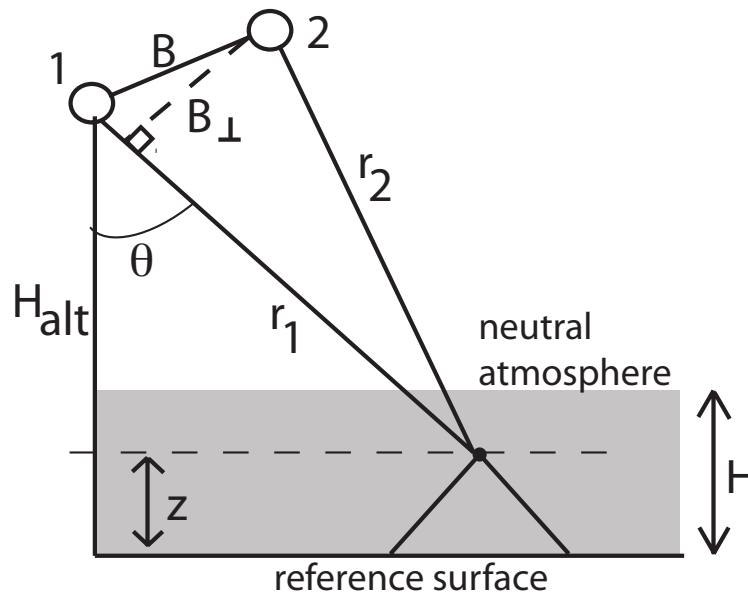


Figure 3.5 (a): InSAR viewing geometry. The two open circles denote the locations of the satellite sensor on both passes 1 and 2 over the scene. A target at height z over the reference surface is at distances r_1 and r_2 to the sensor at passes 1 and 2 respectively. B is the interferometric baseline, while B_{\perp} denotes the component of interferometric baseline perpendicular to the look direction. The look angle is denoted as θ . The shaded box denotes the neutral atmosphere, of thickness H , through which the radar signals propagate

With two SAR observations over the same terrain, an interferometric combination is formed by multiplying one SAR image by the complex conjugate of the other. The scattering phases thus nearly cancel out in the phase difference of the product image. The 2D

array of phase differences in the product image is called an *interferogram*. These phase values are arranged in a range y and azimuth x coordinate system. The residual phase in the interferogram, which we refer to as *interferometric phase*, is equal to path length differences between a resolution cell on the ground and the two SAR antennas plus noise

$$\phi^{INSAR}(x, y) = \frac{4\pi}{\lambda} \Delta r + \phi_{noise}^{INSAR} \quad (3.6)$$

where $\Delta r = r_1 - r_2$ denotes the path length difference, as shown in Figure 3.5. Here, the range coordinate y of a scatterer is given by r_1 , the distance of the scatterer measured by the first (master) SAR observation. Figure 3.4(b) shows an example interferogram over the same Landers area as the SAR image in Figure 3.4(a). This interferogram was formed from two ERS-1 SAR images acquired on April 24th and September 11th, 1992. The colored fringes show the interferometric phase values between 0 and 2π .

The interferometric phase ϕ^{INSAR} observed for a pixel of the radar interferogram is a superposition of phase due to several processes

$$\phi^{INSAR} = \phi_{topo}^{INSAR} + \phi_{defo}^{INSAR} + \phi_{iono}^{INSAR} + \phi_{NA}^{INSAR} + \phi_{orbit}^{INSAR} + \phi_{flat}^{INSAR} + \phi_{noise}^{INSAR} \quad (3.7)$$

where ϕ_{topo}^{INSAR} is the contribution to interferometric phase due to the height of resolution cells above a reference surface which is typically the reference geoid, and ϕ_{defo}^{INSAR} is the phase due to line-of-sight (LOS) range change caused by coherent motion of scatterers between the two SAR observation times. ϕ_{iono}^{INSAR} is the differential phase shift due to signal propagation in the ionosphere while ϕ_{NA}^{INSAR} is due to propagation in the neutral atmosphere. Since interferometric phase measures the difference in phase at two acquisition times, the phase shifts associated with the atmosphere ϕ_{iono}^{INSAR} and ϕ_{NA}^{INSAR} are differences of propagation effects at those two times. In Eq. (3.7), ϕ_{orbit}^{INSAR} is a component of measured phase due to inaccuracies in the knowledge of satellite orbits while ϕ_{flat}^{INSAR} is the phase contribution due to a curvature of the Earth. This phase component is removed using satellite orbit information and a reference Earth model. ϕ_{noise}^{INSAR} is phase noise resulting from thermal noise internal to the radar system and loss of coherence between the individual SAR observations forming the interferogram.

The specific application of InSAR determines which term in Eq. (3.7) is the signal of

interest. In this work, we focus on the phase component due to the neutral atmosphere, ϕ_{NA}^{INSAR} . We hereafter refer to this interferometric phase component simply as *atmospheric phase* bearing in mind that it is actually a difference measurement of propagation effects at two times and that atmospheric phase results only from neutral atmospheric effects. As we explain below, the impact of the ionosphere on InSAR observables is usually minimal. As with GPS neutral atmospheric delay, InSAR atmospheric phase can be similarly partitioned into two contributions: (1) due to (mainly dry) gases in the neutral atmosphere in hydrostatic equilibrium and (2) due to non-hydrostatic water vapor. Unlike GPS, however, InSAR atmospheric phase components are differences of the states at the two acquisition times:

$$\phi_{NA}^{INSAR} = \phi_{hyd}^{INSAR} + \phi_{wet}^{INSAR} \quad (3.8)$$

The dominant source of atmospheric phase variability in radar interferograms is due to fluctuations in water vapor content, while hydrostatic effects are usually minimal (Zebker et al. (1997)). This will be explained in greater detail in Chapter 4. For the present, we discuss the contribution of the other phase terms in Eq. (3.7) to the observed interferometric phase. This discussion will explain how these terms can be accounted for in the estimation of the atmospheric phase term ϕ_{NA}^{INSAR} .

We see in Figure 3.4(b) that the observed fringes correlate with topography. The topographic phase is given by (Zebker and Goldstein (1986))

$$\phi_{topo}^{INSAR} = \frac{-4\pi}{\lambda} \frac{B_{\perp}}{r_1 \sin \theta} z \quad (3.9)$$

where r_1 denotes range, θ is the viewing or *look* angle of the satellite, nominally 23° for ERS-1, and B_{\perp} denotes the component of the interferometric baseline B perpendicular to the look direction as shown in Figure 3.5. Here, z is the height of a particular resolution cell above the reference surface and, thus, depends on local topography. The perpendicular baseline for the two SAR observations forming the interferogram Figure 3.4 was about 800 meters and, from Eq. (3.9), one cycle of phase in the image corresponds to a height change on the ground of about 11 meters. We remove the topographic phase contribution in Figure 3.4 by using a Digital Elevation model (DEM) of the area and Figure 3.4 shows the result.

The phase signature in Figure 3.4(c) now is due to coherent motion of scatterers between the two SAR acquisition times. In this case, ground displacement was caused by a M 7.3 earthquake near Landers, CA on June 28th, 1992. This deformation phase signature corresponds to the ϕ_{defo}^{INSAR} term in Eq. (3.7). Here, a cycle of phase from 0 to 2π corresponds to a 2.86 cm LOS range change of scatterer positions between the 4.5-month time interval. As mentioned in Chapter 1, atmospheric phase distortion ϕ_{NA}^{INSAR} are a major source of error in the interpretation of deformation interferograms, such as Figure 3.4, because the magnitude of ϕ_{NA}^{INSAR} is often comparable to the deformation signal of interest, ϕ_{defo}^{INSAR} . In the case of the deformation interferogram Figure 3.4, however, the combination of dry desert air and large displacements associated with the strong earthquake effectively increases the signal-to-atmospheric-noise ratio for detecting the deformation.

Ionospheric effects in InSAR observations, ϕ_{iono}^{INSAR} are generally minimal at C-band. Phase trends in the image due to the ionosphere have long wavelengths and are usually indistinguishable from phase ramps due to, for example, orbit inaccuracies ϕ_{orbit}^{INSAR} . The magnitude of the ionospheric phase shift is proportional to the density of free electrons in the ionosphere which, in turn, depends on the amount of solar radiation. ERS satellites fly in sun-synchronous, nearly polar orbits. As such, the radar views the same area on the ground at the same local time. Thus, for short time intervals between observations in repeat-pass interferometry, the amount of solar radiation generating free electrons should be approximately equal such that the net effect on the phase difference should be minimal (Hanssen (1998)). The orbit phase ϕ_{orbit}^{INSAR} typically varies slowly over the interferogram and is well-approximated by a low-order polynomial (Hanssen (1998)).

Some InSAR data used in this work are shown in Figure 3.6. We formed this SAR interferogram from ERS-2 radar observations of the Los Angeles County, California area (center latitude 33.5° N, 242.1° W) acquired on November 27th, 1999 (orbit 24072, frame 2925, track 170) and February 5th, 2000 (orbit 25074). On each date, the local SAR acquisition time was 18.30 UTC and this is indicated in Figure 3.2. Hereafter, we refer to this time instant as the *SAR overpass time*. The component of the interferometric baseline perpendicular to the radar look direction, B_\perp for this imaging experiment was 1 meter, thus the topographic phase terms are negligible. Nevertheless, we did remove the small contribution of topography and Earth's curvature to the interferometric phase using a USGS Digital

Elevation Model (DEM) with 30 meter height postings and a reference Earth model. Due to the short time separation (2 months) between SAR observations, we also assumed that any phase due to crustal deformation was similarly negligible. Hence, we interpret the residual phase as due primarily to (1) differences of neutral atmosphere delay at the two acquisition times ϕ_{NA}^{INSAR} , (2) temporal decorrelation, (3) slowly-varying phase trends due to imprecise knowledge of satellite orbit parameters and (4) system noise. We used a total of twenty looks in processing the interferogram yielding a ground pixel spacing of 40 meters, and the data were unwrapped using the method of Chen (2001).

3.4 Conclusions

In this chapter, we have presented an overview of the GPS and InSAR techniques. The primary observables in GPS and InSAR are RF carrier phases. Dry gases (in hydrostatic equilibrium) and water vapor in the neutral atmosphere introduce time delays in the GPS and radar signals and these delays manifest as phase shifts in these observations. In this dissertation, we are primarily interested in the effects of water vapor on these observations. We estimated several timeseries of ZWD from GPS data acquired from the SCIGN network in Southern California (Figure 3.2). We also formed a radar interferogram from two SAR observations of Southern California separated by two months. Correcting this interferogram for topographic phase, we produced an image showing spatial phase variations primarily due to the heterogeneity of water vapor distributions at the two imaging times (Figure 3.6). In Chapter 5, Chapter 6 and Chapter 7 we will present algorithms that use the GPS ZWD timeseries to estimate maps of water-vapor-induced signal delay - proportional to total column water vapor over the study area - which we then subtract from the radar interferogram to reduce the observed water-vapor-induced phase distortions. In the following chapter, we discuss in greater detail the dependence of neutral atmospheric delay magnitude on meteorological quantities such as pressure, temperature and water vapor. We also characterize the spatial and temporal variability of delay in terms of physical processes of the neutral atmosphere.

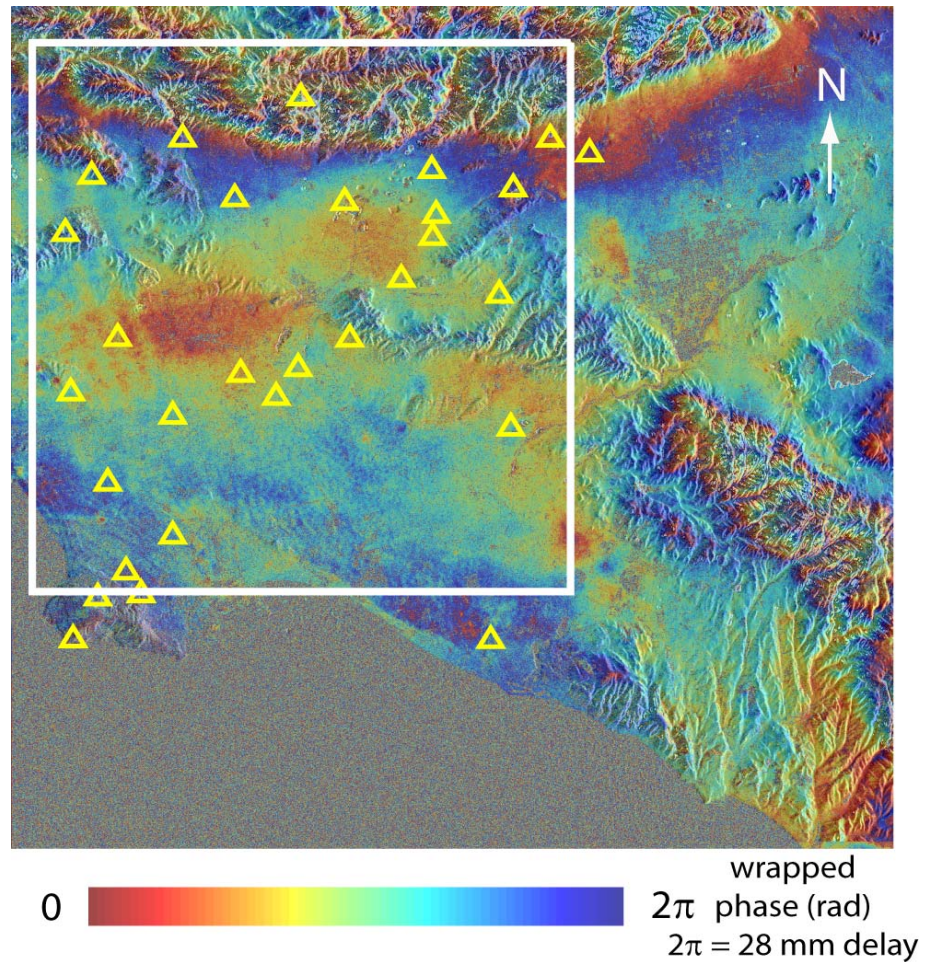


Figure 3.6 Interferogram over Los Angeles/Orange County basin derived from data acquired on November 27th 1999 and February 5th 2000, with topographic phase removed. Yellow triangles indicate locations of SCIGN GPS receivers in the range-azimuth grid of the radar interferogram. The area of study (white box) is approximately 60 km \times 60 km

Chapter 4

The neutral atmospheric signal in GPS and InSAR

4.1 Introduction

In the previous chapter, we described the fundamentals of GPS and InSAR. We showed that the basic GPS and InSAR observable, the signal carrier phase, contains contributions from many sources, among them the effects of the neutral atmosphere. We showed timeseries estimates of neutral atmospheric delay obtained from a network of GPS receivers in Figure 3.2 and we presented a radar interferogram showing spatial variations of phase caused by the difference of neutral atmospheric states at the two SAR observation times, Figure 3.6. We also showed in Chapter 3 that neutral atmospheric delay in GPS and InSAR contains a component due to water vapor in the atmosphere.

In this chapter, we describe how neutral atmospheric delay depends on meteorological properties of the atmosphere, namely pressure, temperature and humidity. The background material presented here draws from studies of neutral atmospheric effects on radio-frequency signals by Davis et al. (1985) and Smith and Weintraub (1953), among others. We focus also on the temporal and spatial variability of GPS and InSAR data (Figures 3.2(b) and 3.6) which are driven primarily by fluctuations in water vapor content in the lower atmosphere. These variations are a major source of error in InSAR images of crustal deformation. Our objective in this dissertation is to use timeseries of ZWD from GPS to

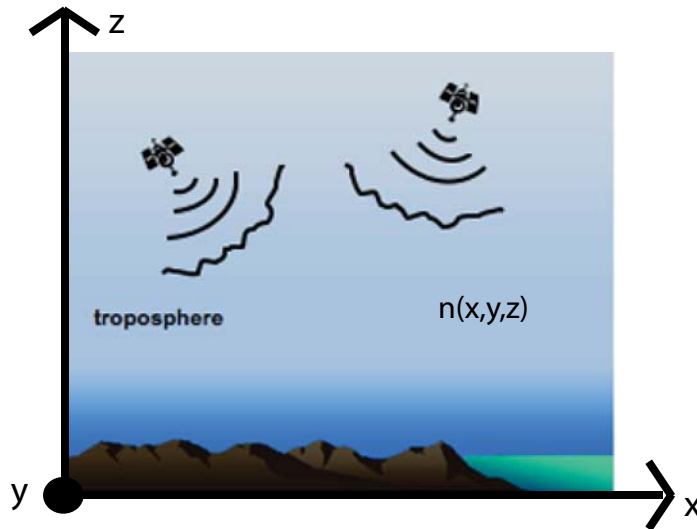


Figure 4.1 Schematic diagram illustrating the neutral atmospheric propagation medium and coordinate system used in this study

infer maps approximating the atmospheric phase distortions observed in InSAR.

We then present an overview of existing approaches proposed by other authors for reducing atmospheric phase distortions in InSAR interferograms using GPS and meteorological data. This overview will allow us to compare our method and results obtained in subsequent chapters with the existing approaches. More importantly, this overview will highlight some issues related to using GPS ZWD observations to correct InSAR atmospheric phase. In the following chapters, we will address these issues.

4.2 Meteorological dependence

The neutral atmosphere propagation medium can be modeled as a three-dimensional half space ($z \geq 0$) bounded by the Earth's surface, as shown in Figure 4.1. GPS and InSAR signals are affected by the neutral atmosphere in similar ways because both the GPS and radar signals are electromagnetic waves at approximately the same frequency propagating through the same medium (Williams et al. (1998)). At these frequencies, the neutral at-

mosphere is non-dispersive and the refractive index n of the medium is real-valued. The neutral atmospheric refractive index deviates slightly from unity (the free-space value) and rarely exceeds 400 parts per million (ppm). Following (Bevis et al. (1992)), we also denote the scaled deviation of n from unity as *refractivity* N ,

$$N = 10^6(n - 1) \quad (4.1)$$

We can determine the effect of the neutral atmosphere on the phase of GPS and radar signals using the scalar wave equation

$$\Delta^2 U + k^2 n^2 U = 0 \quad (4.2)$$

where $k = 2\pi/\lambda$ is the wavenumber of radiation. We assume a time-harmonic dependence of the radiation and we neglect time variation of refractive index since the travel time of the electromagnetic signals is much shorter than typical time scales of neutral atmospheric variation. We express the radiation as

$$U(x, y, z) = A(x, y, z)e^{j\phi(x, y, z)} \quad (4.3)$$

where A denotes the amplitude and ϕ denotes the phase. The amplitude A is very insensitive to the presence of water vapor in the atmosphere and so we consider only the phase of propagating GPS and radar signals. As the wavelengths of GPS and InSAR signals are much shorter than typical spatial scales of variation in the neutral atmosphere, we can adopt the geometrical optics approximation (Born (1959)). For a signal propagating in the vertical direction, the solution for ϕ satisfying Eq. (4.2) is then given by

$$\phi(x, y, z = 0) = \frac{2\pi}{\lambda} \left(\int_0^L dz + 10^{-6} \int_0^L N(x, y, z) dz \right) \quad (4.4)$$

and the phase is measured on the ground at $z = 0$ from a signal source at height $z = L$. The first term in the parentheses is the geometric distance between the source and the ground while the second integral denotes the excess path length traveled by the signal due to the neutral atmosphere. It is this excess path length, in units of meters, that we refer to as

neutral atmospheric delay because, dividing this term by the speed of light c yields the additional time required for the propagating wave to reach the ground. We note that GPS signal ray paths need not coincide with the vertical direction, in which case the integration in Eq. (4.4) is along the slanted ray path. For non-nadir incidence, we can neglect effects of ray bending due to refraction in the atmosphere as this effect is small compared to the excess path length in Eq. (4.4) (Hanssen (1998)).

Zenith neutral atmospheric delay (ZND) measured over time by a GPS receiver on the ground is

$$I_{NA}^{GPS,z}(x,y,t) \approx 10^{-6} \int_0^L N(x,y,z,t) dz \quad (4.5)$$

where we have now explicitly included the time-dependence of neutral atmospheric refractivity. GPS-derived measures of the vertical integration of refractivity above a point (x,y) on the ground are approximate because, as explained in Chapter 3, GPS-derived ZNDs are actually weighted averages of a conical volume of atmosphere above the receiver, as shown in Figure 3.1.

The atmospheric phase observed in the SAR interferogram is given by

$$\phi_{NA}^{INSAR}(x,y;t_1,t_2) = \frac{4\pi}{\lambda \cos \theta} 10^{-6} \left(\int_0^L N(x,y,z,t_1) dz - \int_0^L N(x,y,z,t_2) dz \right) \quad (4.6)$$

where t_1 and t_2 denote the two SAR observation times; these are spaced 2 months apart for the InSAR data shown in Figure 3.6. The $\frac{1}{\cos \theta}$ factor in the above is a mapping function that projects zenith-directed neutral atmospheric delay differences to the radar line-of-sight (LOS), defined by the look angle θ nominally 23° for ERS-2. The additional factor of 2 is due to two-way propagation of the radar signal through the neutral atmosphere. From Eqs. (4.5) and (4.6), we see that GPS measures time variation of ZND at a fixed location while InSAR measures the spatial variations of atmospheric phase, which is proportional to the difference at two observation times of neutral atmospheric delays.

In Chapter 3, we alluded to the decomposition of neutral atmospheric effects in GPS and InSAR observations into hydrostatic and water-vapor-dependent components, Eqs. (3.4) and (3.8). We now explain this decomposition physically by examining the dependence of neutral atmospheric refractivity on pressure, temperature and humidity. The refractivity N

is given by Thayer (1974)

$$N = k_1 \frac{P_d}{T} + \left(k_2 \frac{e}{T} + k_3 \frac{e}{T^2} \right) + 1.45W \quad (4.7)$$

where P_d is pressure of dry air in hecto-Pascals (hPa), T is absolute temperature in Kelvin, e is the partial pressure of water vapor in hPa and W is liquid water content in g/m^3 . The constants are $k_1 = 77.6 \text{ KhPa}^{-1}$, $k_2 = 71.6 \text{ KhPa}^{-1}$ and $k_3 = 3.75 \times 10^5 \text{ K}^2\text{hPa}^{-1}$. Noting that total atmospheric pressure (in hPa) $P = P_d + e$, an alternate formula for neutral atmospheric refractivity is given by Davis et al. (1985)

$$N = k_1 \frac{P}{T} + \left(k'_2 \frac{e}{T} + k_3 \frac{e}{T^2} \right) + 1.45W \quad (4.8)$$

where $k'_2 = k_2 - R_d/R_v k_1$. Here, $R_d = 287.053 \text{ J K}^{-1}\text{kg}^{-1}$ and $R_v = 461.524 \text{ J K}^{-1}\text{kg}^{-1}$ are the gas constants of dry air and water vapor respectively. We will use Eq. (4.8) in this dissertation.

The first term in Eq. (4.8) above is commonly referred to as *hydrostatic refractivity* because the atmosphere, particularly dry air, is approximately in hydrostatic equilibrium where the downward force of gravity on the air column is balanced by an upward-directed pressure gradient force. Thus, from Eq. (4.8), the corresponding *zenith hydrostatic delay* (ZHD) is

$$I_{hyd}^z = 10^{-6} \int_0^L N_{hyd} dz = 10^{-6} \int_0^L k_1 \frac{P}{T} dz \quad (4.9)$$

where we have suppressed the (x, y, z, t) dependence of the various quantities above for simplicity. ZHD can be approximated to an accuracy of 1 mm (Bevis et al. (1992)) given accurate surface measurements of atmospheric pressure, P_s , using the Saastamoinen model (Saastamoinen (1972))

$$I_{hyd}^z = k_1 10^{-6} \frac{R_d}{g_m} P_s \quad (4.10)$$

where g_m is the local gravity at the center of the atmospheric column and P_s is in units of hPa. Hydrostatic delay is the largest component of total ZND, typically around 2.1 meters. Also, because of its dependence on surface pressure (Eq. (4.10)), hydrostatic delay is strongly dependent on altitude because the total amount of air contained in a column of atmosphere decreases with increasing height.

In Eq. (4.8), the term in parentheses denotes the contribution due to water vapor. The associated delay, zenith wet delay (ZWD), is

$$l_{wet}^z = 10^{-6} \int_0^L N_{wet} dz = 10^{-6} \int_0^L \left(k_2' \frac{e}{T} + k_3 \frac{e}{T^2} \right) dz \quad (4.11)$$

where, again, we have we suppressed the (x, y, z, t) dependence. The magnitude of wet delay is much smaller than hydrostatic delay, typically less than 30 cm (Hanssen et al. (1999)) as shown in Figure 3.2. We note from Eq. (4.11) that wet delay also depends on temperature. However, the sensitivity of wet delay to a 1°C change in temperature is 4-20 times smaller than a corresponding 1 hPa change in water vapor partial pressure (Hanssen (1998)).

We now show that ZWD is proportional to total column water vapor. Following Bevis et al. (1992), we define *weighted mean temperature* T_m as follows

$$T_m = \frac{\int_0^H (e/T) dz}{\int_0^H (e/T^2) dz} \quad (4.12)$$

where H denotes the thickness, or *scale height*, of a layer of troposphere where water vapor is most abundant. The equation of state for water vapor is $e = \rho_v R_v T$, where ρ_v is water vapor density (kg/m^3). Using the equation of state and Eq. (4.12) in Eq. (4.11), ZWD can be expressed as

$$l_{wet}^z = 10^{-6} R_v (k_2' + k_3/T_m) \int_0^H \rho_v dz \quad (4.13)$$

The integral in Eq. (4.13) is total column water vapor above a point on the ground. Bevis et al. (1992) found that the weighted mean temperature T_m is well-approximated by surface temperature measurements using the empirical formula

$$T_m \approx 70.2 + 0.72T_s \quad (4.14)$$

where T_s is surface temperature in Kelvin. This empirical formula was derived from analysis of 8718 radiosonde profiles spanning a two-year interval from sites in the United States. Using the empirical formula above, the scale factor in Eq. (4.13) can be determined to an accuracy of 2%. However, assuming a constant nominal value of T_m for all areas and

seasons causes Eq. (4.13) to be accurate to about 15% (Bevis et al. (1992)). Thus, given measurements of surface temperature, we see that ZWD from GPS and InSAR can be used to accurately measure total column water vapor temporally or spatially.

The final term in Eq. (4.8) indicates the contribution of liquid water to neutral atmospheric delay. This term essentially determines the impact of clouds on delay measurements. ZND due to clouds is given by (Hanssen (1998))

$$I_{cloud}^z = 1.45WL_{cloud} \quad (4.15)$$

where L_{cloud} is the height of the cloud in meters. Hanssen (1998) shows that for certain types of clouds, cumulus congestus and cumulonimbus in particular, this component of delay can reach 0.5 cm. However, for most other types of clouds, the corresponding ZND is typically < 1 mm.

Atmospheric phase distortions in InSAR, shown in Figure 3.6, are similarly modeled as

$$\begin{aligned} \phi_{NA}^{INSAR}(x, y) = & \frac{4\pi}{\lambda \cos \theta} 10^{-6} k_1 \left(\int_0^L \frac{P}{T} |_{t_1} - \frac{P}{T} |_{t_2} dz \right) + \\ & \frac{4\pi}{\lambda \cos \theta} 10^{-6} \left(\int_0^L k_2' \frac{e}{T} |_{t_1} + k_3 \frac{e}{T^2} |_{t_1} - k_2' \frac{e}{T} |_{t_2} - k_3 \frac{e}{T^2} |_{t_2} dz \right) \end{aligned} \quad (4.16)$$

where we have suppressed the (x, y, z) dependence in the various meteorological quantities above and we have neglected the contribution due to liquid water. The terms in the first parenthesis show hydrostatic delay difference at the two SAR observation times, ϕ_{hyd}^{INSAR} , while the terms in the second parenthesis denote wet delay difference, ϕ_{wet}^{INSAR} in Eq. (3.8), Chapter 3. As in GPS, the hydrostatic delay difference in InSAR is correlated with topography because of the altitude-dependence of surface pressure. Hereafter, we shall use the term atmospheric phase to denote the observed phase signature in Figure 3.6 multiplied by $\lambda \cos(\theta)/(4\pi)$. That is, atmospheric phase will be expressed as equivalent zenith-directed neutral atmospheric delay difference in millimeters.

In Figure 4.2, we plot the difference in GPS ZWD at the SAR overpass times, indicated in Figure 3.2, against the InSAR atmospheric phase distortions averaged in a box of pixels centered on the GPS receiver locations. The correlation coefficient between these two measurements is 0.91. Thus, GPS and InSAR measurements of neutral atmospheric delay

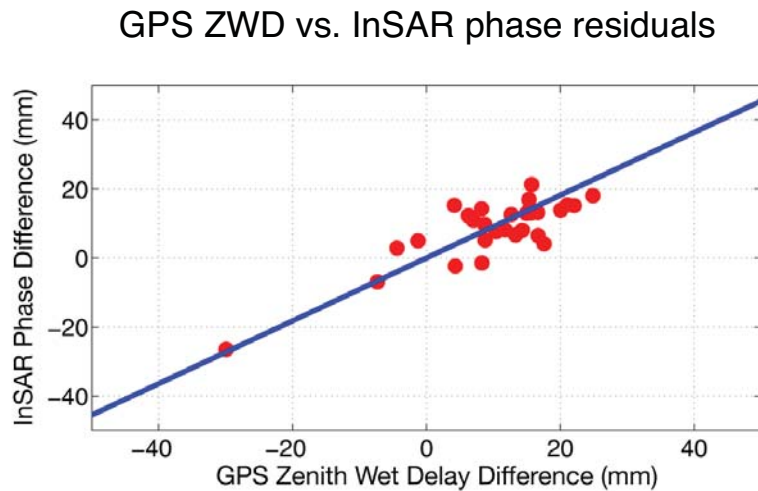


Figure 4.2 InSAR atmospheric phase plotted against GPS ZWD difference from the 29-receiver SCIGN network at the SAR overpass times. The phase residuals are averaged in 8 km by 8 km blocks reflecting the fact that GPS ZWD combines many observations in a reversed cone above the receiver. The use of 8 km by 8 km averaging windows exceeds the corresponding circular area of the 8 km-diameter cone by about 28%. The slope of the line in the figure is 0.91, and not 1.0 due to noise in both data sets.

are in reasonable agreement although there is noise in both datasets. The error in the GPS measurements is about 5.6 mm. While neutral atmospheric delay can be estimated directly from GPS data (Chapter 3), atmospheric phase distortions remain a major source of error in InSAR images of crustal deformation. Therefore, Eq. (4.16) can, in principle, be used to estimate the atmospheric contribution to observed interferometric phase. The suggested method for calculating the neutral atmospheric contribution to InSAR observations, Eq. (4.16), requires accurate measurements of atmospheric pressure, temperature, humidity and liquid water content at the spatial resolution of InSAR. Slowly-varying surface pressure can be measured using ground-based sensors and thus the hydrostatic delay difference contribution ϕ_{hyd}^{INSAR} , although generally minimal, can be reliably inferred. However, conventional meteorological instruments such as ground-based sensors, radiosondes and satellite-based spectroradiometers cannot measure water vapor content at the fine resolution required to characterize its variability. This limits the accuracy of wet delay difference ϕ_{wet}^{INSAR} maps. Instead, in this work, we approach the problem of InSAR atmospheric phase reduction by

focussing on the temporal and spatial variability of neutral atmospheric delay measured at high-resolution by GPS and InSAR. As will be discussed in the following section, this variability is driven primarily by water vapor fluctuations in the lower atmosphere.

4.3 Spatial and temporal variability

Hydrostatic and wet delay vary both spatially and temporally. From Eq. (4.10), hydrostatic delay follows the variation of atmospheric pressure at the surface. Since surface pressure varies slowly over time and space, hydrostatic delay, while relatively large in magnitude, shows smooth variation and can be estimated even with low-resolution meteorological sensor measurements.

However, wet delay is more spatially and temporally variable than hydrostatic delay. Daily variability of wet delay exceeds that of hydrostatic delay by an order of magnitude (Elgered et al. (1991)). These variations are caused by transport and mixing of water vapor in the neutral atmosphere in the lower atmosphere. These motions occur over a range of spatial scales. Turbulent wind vortices are small-scale flow irregularities that efficiently transport and mix water vapor and heat. At larger scales, weather systems determine the flow characteristics. Since water vapor is an approximate tracer of atmospheric motions (Ishimaru (1978)), its flow-induced spatial and temporal variations occupy a range of scales as well. It is due to this variability that water vapor cannot be predicted with sufficient accuracy using only surface measurements of humidity (Bevis et al. (1992)).

We saw in Chapter 3 that time variations of wet delay can be estimated from GPS data. The GIPSY software we used models the temporal variability of wet delay as a first-order Gauss-Markov stochastic process; reduction of these data yielded the estimated ZWD timeseries shown in Figure 3.2. Here we assume that the short-scale temporal fluctuations in the ZWD timeseries are due to the mixing of water vapor in the atmosphere by irregular flow patterns. As we assume a nominal value of 2.1 meters for hydrostatic delay in this work, the timeseries of ZWD shown in Figure 3.2(b) may be biased by unmodeled hydrostatic effects. These unmodeled hydrostatic delays depend on surface pressure. Consequently, they vary slowly in time relative to water vapor turbulent fluctuations and are strongly correlated with the altitude of the GPS station. As we shall see in Chapter 5, these errors can

be minimized by correcting the GPS data for altitude-dependent delay.

Hydrostatic delay is quite repeatable in time (Zebker et al. (1997)) and, therefore, hydrostatic delay minimally contributes to InSAR atmospheric phase variability and manifests as slowly-varying phase trends similar to signatures caused by orbit inaccuracies. Moreover, residual hydrostatic delay will be correlated with topography. Water vapor, in contrast, varies significantly both spatially and temporally and so its contribution is *not* minimized in the difference of two SAR observations forming the interferometric phase. In fact, several authors such as Williams et al. (1998), Hanssen (1998) and Zebker et al. (1997)) note that the spatial distribution of water vapor is uncorrelated on time scales greater than one day. In repeat-pass SAR interferometry, radar observations are made more than one day apart and, therefore, the neutral atmospheric water vapor distribution on both passes are uncorrelated. Therefore, we will assume that the short-scale variations in the observed atmospheric phase distortions shown in Figure 3.6 are primarily due to the difference in water vapor spatial distribution at the SAR overpass times.

We do not aim in this work to derive quantitative estimates of water vapor content from InSAR and GPS data because: (1) InSAR atmospheric phase is a relative measurement of water vapor at two imaging times and, thus, the measurements contain an arbitrary bias, (2) we do not calibrate the data for hydrostatic effects as surface pressure measurements were unavailable and (3) determination of absolute levels of water vapor content from GPS and InSAR data requires surface temperature measurements over the study area (Bevis et al. (1992)).

Instead, we seek to reproduce the spatial variability of atmospheric phase observed in the InSAR data using timeseries of ZWD measured from a GPS network. We show below that GPS measurements of ZWD and InSAR atmospheric phase distortions display variability due to: (1) a topography-dependent variation resulting from the mean vertical stratification of the neutral atmosphere and (2) short-scale variability caused by transport and mixing of water vapor by turbulent wind vortices. Hereafter, we refer to the component of InSAR atmospheric phase variability dependent on the vertical stratification of the neutral atmosphere as *topography-dependent atmospheric phase*. We refer to the component showing short-scale variability as *turbulently-mixed atmospheric phase*. In Chapter 5, we will use the GPS ZWD measurements acquired exactly at the SAR overpass times to

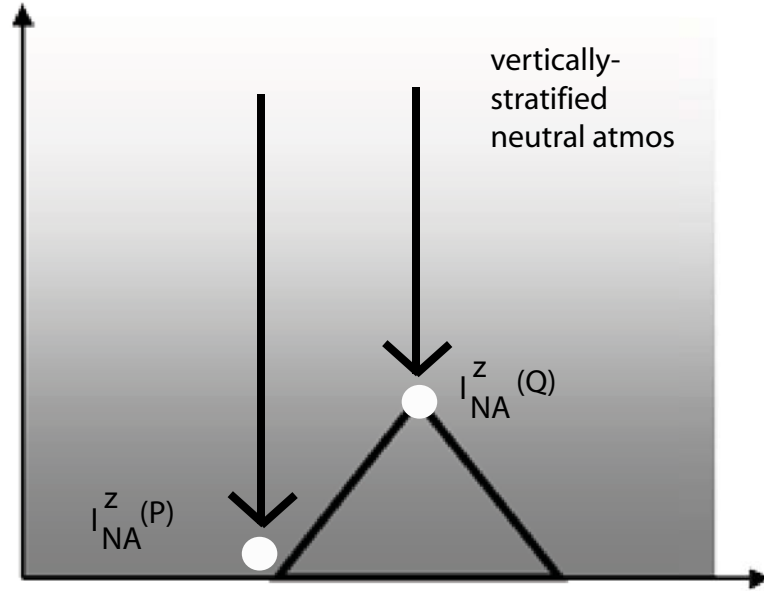


Figure 4.3 Zenith neutral atmospheric delays measured at the top (Point Q) and base (Point P) of a mountain assuming a vertically-stratified neutral atmosphere indicated by the shading. The arrows indicate microwave signals incident on the measurement locations in the zenith direction. The delay due to the stratified neutral atmosphere measured at Q is denoted $l_{NA}^z(Q)$ while the corresponding delay at P is $l_{NA}^z(P)$

estimate both these types of variations observed in the InSAR data.

4.3.1 Vertically-stratified neutral atmosphere

Now, we discuss the effect of a neutral atmosphere that varies only in the z -direction on estimates of ZWD. Consider measurements of zenith neutral atmospheric delay made at points P and Q, respectively at the base and top of a mountain of height h as shown in Figure 4.3. The difference in zenith delay between points P and Q is given by

$$\begin{aligned} l_{NA}^z(P) - l_{NA}^z(Q) &= 10^{-6} \int_0^h N dz \\ &= (l_{hyd}^z(P) - l_{hyd}^z(Q)) + (l_{wet}^z(P) - l_{wet}^z(Q)) \end{aligned} \quad (4.17)$$

Based on the formula for refractivity N , Eq. (4.8), we see that the difference in measured

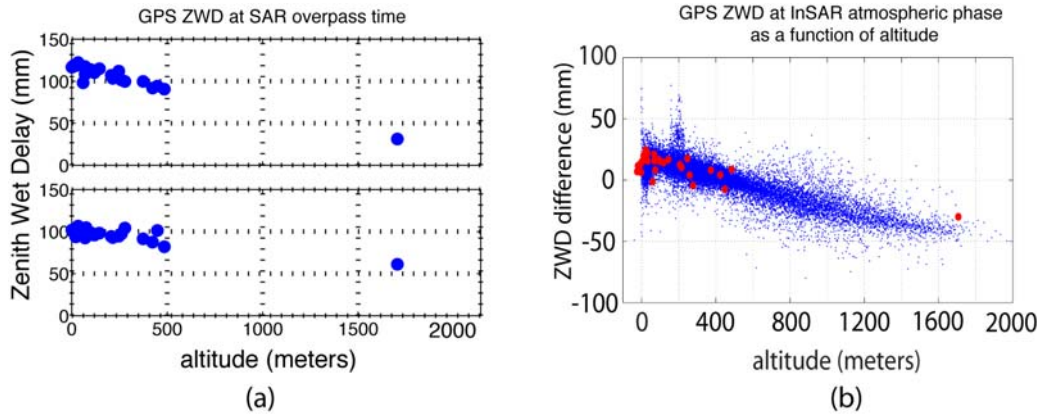


Figure 4.4 (a): GPS ZWD at the SAR overpass times plotted as a function of altitude. (b): Atmospheric phase (blue) and GPS ZWD differences (red) plotted as a function of altitude.

delays between points P and Q depends on the vertical profile of pressure, temperature and humidity. Since hydrostatic delay can be modeled accurately using surface pressure measurements alone, the expressions in the first parentheses above are proportional to the difference in surface pressure P_s at the altitudes of points P and Q. The difference in wet delays between points P and Q is mainly determined by the vertical distribution of water vapor in the lower atmosphere, although we note that temperature also decreases with increasing height at an environmental lapse rate of $6.5^\circ\text{C}/\text{km}$.

As water vapor column and surface pressure both decrease with increasing height, then we expect $I_{NA}^z(P) > I_{NA}^z(Q)$. We observe this behavior in Figure 4.4(a), where we have plotted GPS ZWD, acquired at the times of SAR overpass against altitude. Thus, from Figure 4.4(a), ZWD estimates from the GPS network measure the mean vertical stratification of water vapor in the neutral atmosphere, albeit with a smaller dependence on surface pressure due to unmodeled hydrostatic effects. Similarly, the InSAR atmospheric phase exhibits a strong dependence on surface elevation, as shown in Figure 4.4(b). This quantity is proportional to neutral atmospheric delay differences at the two SAR observation times (2 months apart). Also in Figure 4.4(b), we plot GPS ZWD differences in red and we observe that GPS and InSAR show similar sensitivities to the mean vertical profile of the neutral atmosphere. The high correlation between InSAR and GPS measurements in Figure 4.2 is

thus largely explained by the similar vertical profiles shown in Figure 4.4(b).

We expect the topography-dependent component of ZWD variations in GPS and InSAR observations to vary slowly in time, relative to the fluctuations caused by turbulent mixing. This can be seen from the characterization of neutral atmospheric delay by Williams et al. (1998) as a sum of the effects of a homogeneous and heterogeneous troposphere. The authors note that the height-dependence of neutral atmospheric delay from GPS and InSAR is due to homogeneous troposphere, which is time-invariant and dependent on the overall thickness of the neutral atmosphere plus some mean, constant atmospheric parameters. In contrast, the short-scale spatial and temporal delay fluctuations are due to the heterogeneous troposphere, which results from atmospheric turbulence. Emardson et al. (2003) found that mean vertical stratification of neutral atmospheric water vapor, exhibited by height-dependence of GPS ZWD measurements, correlated over longer time scales than horizontal variations.

We demonstrate the effects of the homogeneous and heterogeneous troposphere on delay measurements by comparing the time-variation of the vertical trend of ZWD and fluctuations of ZWD about this vertical trend. Figure 4.5 shows a histogram of the temporal change in ZWD as a percentage of measured ZWD at a given time from all timeseries shown in Figure 3.2(b). In particular, the plot in blue shows the distribution corresponding to relative change of the ZWD vertical-stratification while the plot in red shows the distribution of the relative change of the scatter about the vertical profile. Here, we have used an exponential model to describe the vertical profile of ZWD. Thus, the histogram in blue shows the relative change of the ZWD component described by the exponential model. We will explain this model in further detail in Chapter 5. For now, we use this model to illustrate the differences between relative rate of ZWD change between the exponential vertical trend of ZWD and the ZWD scatter about this trend. We observe from Figure 4.5 that the relative temporal change of the vertical-dependence shows a smaller dispersion than that of the residuals. This suggests that the scatter about the ZWD vertical profile shows greater variability in time than the vertical profile itself. Therefore, we conclude that the topography-dependent component of ZWD variations in GPS and InSAR observations to vary slowly in time, relative to the fluctuations caused by turbulent mixing of water vapor.

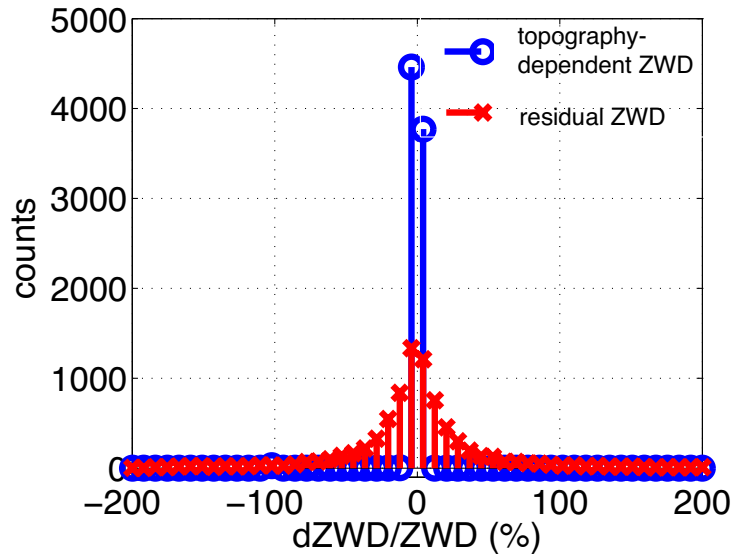


Figure 4.5 Histogram of temporal changes of ZWD as a percentage of ZWD measured at a given time. Blue denotes the relative change of vertical (linear) trend of ZWD while red shows the relative change of ZWD scatter about the vertical trend.

4.3.2 Variability due to turbulent mixing

Now, we discuss the short-scale spatial variation of wet delay caused by turbulent mixing of water vapor in the neutral atmosphere. Turbulence is the phenomenon associated with random perturbations of the mean flow of air in the atmosphere. Turbulence is a process of the planetary boundary layer (PBL), which is the lowest 1-2 km of the troposphere. Within the PBL, the atmosphere is directly influenced by the Earth's surface and responds to surface forcings with a timescale of an hour or less (Stull (1988)). Turbulence occurs as the result of solar heating of the Earth's surface, causing convection and wind shear (Hanssen (1998)). Turbulence efficiently transports and mixes water vapor and, since water vapor is concentrated in the lower atmosphere, the spatial and temporal fluctuations of water vapor, measured respectively by InSAR and GPS, are thus mainly driven by turbulent processes. In the following, we will show that this is indeed the case by comparing several types of power spectra, computed from the InSAR atmospheric phase and GPS ZWD timeseries, with the corresponding predictions from theory.

The temporal and spatial phase fluctuations resulting from electromagnetic signal propagation in a turbulent neutral atmosphere can be described by the power spectral density (PSD) and structure functions of those fluctuations. The theoretical expressions for these quantities assume a random model for a turbulent atmosphere whose statistics follow Kolmogorov turbulence theory. This theory predicts the mathematical form of the 3D structure function and PSD of turbulent wind fluctuations. Since water vapor is an approximate tracer for turbulent motions in the atmosphere (Ishimaru (1978)), then the corresponding structure function and PSD of the water-vapor component of neutral atmospheric refractivity N_{wet} also follows Kolmogorov statistics. The theoretical expressions for the PSD and structure function of wet delay were originally presented in Tatarskii (1961). We summarize in the following these theoretical results as applied to the two-dimensional InSAR atmospheric phase one-dimensional and GPS ZWD timeseries. The derivation of these results is given in Appendix B. For further details, the reader is referred to Hansen (1998).

First, however, we recall that the correlation function of a wide-sense stationary random function g of three dimensions is given by

$$C(\mathbf{r}) = \langle g(x, y, z)g(x', y', z') \rangle, \quad \text{where } \mathbf{r} = \begin{bmatrix} x - x' \\ y - y' \\ z - z' \end{bmatrix} \quad (4.18)$$

By the Wiener-Khinchin theorem, the PSD of g is the Fourier transform of $C(\mathbf{r})$

$$S(\mathbf{k}) = \int_{-\infty}^{\infty} \int_{-\infty}^{\infty} \int_{-\infty}^{\infty} C(\mathbf{r}) e^{-j\mathbf{k} \cdot \mathbf{r}} d\mathbf{r}, \quad \text{where } \mathbf{k} = \begin{bmatrix} k_x \\ k_y \\ k_z \end{bmatrix} \quad (4.19)$$

is the three-dimensional wavevector. The structure function of g is defined as follows

$$D(\mathbf{r}) = \langle (g(x, y, z) - g(x', y', z'))^2 \rangle \quad (4.20)$$

Since g is a second-order stationary process (Tatarskii (1961)), then

$$D(\mathbf{r}) = 2C(\mathbf{0}) - 2C(\mathbf{r}) \quad (4.21)$$

For the structure function of a random function g to exist, the function need not necessarily be wide-sense stationary. In fact, the mean of the function g can vary linearly with position. A transform relation between the structure function and the PSD is as follows

$$D(\mathbf{r}) = 2 \int_{-\infty}^{\infty} \int_{-\infty}^{\infty} \int_{-\infty}^{\infty} S(\mathbf{k})(1 - e^{j\mathbf{k}\cdot\mathbf{r}}) d\mathbf{k} \quad (4.22)$$

The structure function for atmospheric refractivity is

$$D(\mathbf{r}) = C^2 \|\mathbf{r}\|^{2/3}, \quad l_i < \|\mathbf{r}\| < l_o \quad (4.23)$$

where l_i and l_o are the inner and outer scales of turbulence, respectively. l_i is typically less than 100 meters while l_o is on the order of the thickness of the boundary layer where most water vapor resides, typically 1-2 km (Hanssen (1998)). This range of spatial scales is called the *inertial subrange*. The associated PSD for N_{wet} is

$$S(\mathbf{k}) \propto \|\mathbf{k}\|^{-11/3}, \quad k_o < \|\mathbf{k}\| < k_i \quad (4.24)$$

where k_o and k_i are the wavenumbers corresponding to the outer and inner scales of turbulence respectively. We see then that Kolmogorov theory predicts wet refractivity turbulent variations with statistics that are isotropic, follow a power law, and are valid only within a certain range of spatial scales.

To compute the corresponding quantities for the turbulently-mixed atmospheric phase, we first assume equal structure functions and PSDs for the wet refractivity random functions at both SAR acquisition times. Also, we assume that the two refractivity distributions are uncorrelated. Then, using Eqs. (4.11), (4.23) and (4.24), the turbulently-mixed atmospheric phase structure function D_ϕ is given by

$$D_\phi(\mathbf{R}) = D_\phi(\|\mathbf{R}\|) \propto 2 \int_0^L (L-z)[D(\mathbf{R},z) - D(\mathbf{0},z)] dz, \quad \text{where } \mathbf{R} = \begin{bmatrix} x-x' \\ y-y' \end{bmatrix} \quad (4.25)$$

The factor of two in the above is due to the superposition of identical delay power spectra

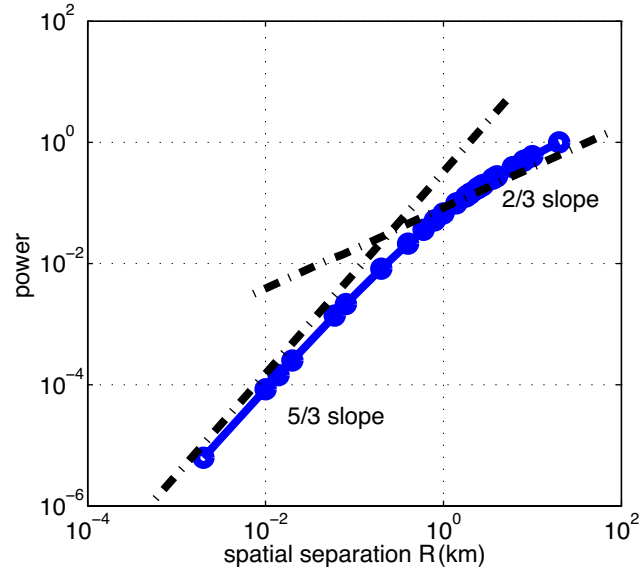


Figure 4.6 The Treuhaft-Lanyi structure function model Eq. (4.25) for neutral atmospheric delay fluctuations due to turbulent variations of atmospheric water vapor

from the two SAR observations. The corresponding power spectrum

$$S_{\phi}(\mathbf{u}) = S(\mathbf{u}, 0) \propto \|\mathbf{u}\|^{-11/3}, \quad \text{with } \mathbf{u} = \begin{bmatrix} k_x \\ k_y \end{bmatrix} \quad (4.26)$$

where \mathbf{u} is the wavevector in the $x - y$ plane of the atmospheric phase. The structure function model, Eq. (4.25), was first derived in Treuhaft and Lanyi (1987) and used to study fluctuations of wet delay observed in Very-Long-Baseline-Interferometry (VLBI). In Figure 4.6, we have numerically evaluated Eq. (4.25) and plotted the log of the result versus $\log(\|\mathbf{R}\|)$. We note that the slope of $D_{\phi}(\mathbf{R})$ is not constant and varies from 5/3 at short spatial scales to about 2/3 at larger scales. Stotskii (1973) notes that, at spatial separations larger than the thickness of the PBL (1 – 2 km), turbulent eddies can be regarded as effectively two-dimensional and this results in the lower structure function slopes at those scales.

Next, we discuss the statistics of temporal ZWD measurements. As GPS ZWD are temporal observations, the empirical structure functions and PSDs computed are functions

of time (seconds) and temporal frequency (Hz) respectively. However, we note that Kolmogorov turbulence theory predicts only the spatial statistics of wet refractivity fluctuations. The frozen-flow hypothesis is commonly used to convert from spatial to temporal statistics (Tatarskii (1961), Ishimaru (1978), Treuhft and Lanyi (1987), Hanssen (1998)). This hypothesis states that delay fluctuations observed over time at a fixed point are due to spatial fluctuations of a refractivity random field moving across that fixed point by wind with velocity \mathbf{V} . Moreover, this hypothesis assumes that the spatial statistics of the moving refractivity field are unchanged by its passage across the fixed point. As a consequence, temporal frequency (in Hz) is related to spatial wavenumber by the following

$$f \text{ (Hz)} = \mathbf{k} \text{ (cycles/meter)} \cdot \mathbf{V} \text{ (meters/second)} \quad (4.27)$$

By the frozen-flow hypothesis, temporal fluctuations of wet delay measured at a point are equivalent to a 1D profile through the 2D wet delay field Eq. (4.11) in the direction of wind \mathbf{V} . Assuming an observation location at $(x, y) = (0, 0)$ and the direction of motion along the x -axis only, then the structure function of GPS ZWD timeseries is

$$D_{GPS}(\tau) = (1/2)D_{\phi}(x - x', 0)|_{x-x'=V_x\tau} \quad (4.28)$$

The factor of $1/2$ arises because GPS observations are made at a single time while InSAR atmospheric phase is a difference of observations at two times. Thus, the temporal structure function of ZWD essentially follows the Treuhft-Lanyi model except that the spatial coordinate is replaced by $V_x\tau$. The corresponding equation for the PSD is

$$S_{GPS}(f) = (1/2) \int_{-\infty}^{\infty} S_{\phi}(k_x, k_y) dk_y|_{k_x=f/V_x} \quad (4.29)$$

Thus, $S_{GPS}(f) \propto f^{-8/3}$ for frequencies within the inertial subrange.

In Figure 4.7(a), we show the rotationally-averaged spatial structure function computed from InSAR atmospheric phase (green line). Computation of a corresponding spatial structure function profile from the GPS ZWD data is incomplete due to the sparse and irregular distribution of the SCIGN GPS network. Reliable estimation is restricted to a few, unequally-spaced samples of the 2D structure function. We have developed a method for

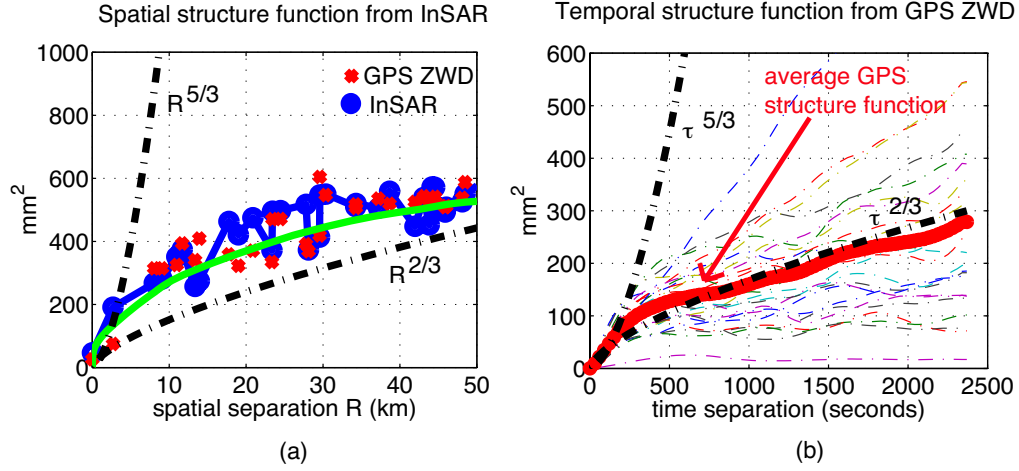


Figure 4.7 (a): Rotationally-averaged spatial structure function profile from InSAR atmospheric phase (green), empirical structure function at sparse lags from GPS ZWD at the SAR overpass times (red) and averaged InSAR structure function values at those lags used in the estimation of GPS structure function (blue). The black dashed lines indicate theoretical power law structure functions from the Treuhaft-Lanyi model. (b): Temporal structure functions computed from the 29 SCIGN GPS ZWD timeseries in a 6-hour time window centered around the SAR overpass times. Shown also are theoretical $5/3$ and $2/3$ power law structure functions. The thick red line is the average of structure function profiles from all GPS receivers

computing structure function values from the sparse array of measurements. In Chapter 5 and Chapter 6, we use this method to derive sparse estimates of the spatial auto- and cross-correlation functions of ZWD.

In our approach, we first define a small set of points $\{\mathbf{R}_k\}$ over the extent of the structure function where the value of the function is estimated. To estimate the function value, we average squared differences of ZWD difference $\Delta l_{wet}^{GPS,z}$ data from all pairs of GPS receivers in the network whose spatial separations are approximately equal to \mathbf{R}_k . Figure 4.8 shows a contour map of the InSAR atmospheric phase 2D structure function, range-azimuth separations (lags) of all pairs of GPS sites (black crosses) and the set of points $\{\mathbf{R}_k\}$ where we estimate structure function (red circles). We chose the set of estimation locations, $\{\mathbf{R}_k\}$, by applying the *k-means* (Gersho and Gray (1992)) clustering algorithm to all range-azimuth lags derived from pairs of GPS sites (black crosses in Figure 4.8).

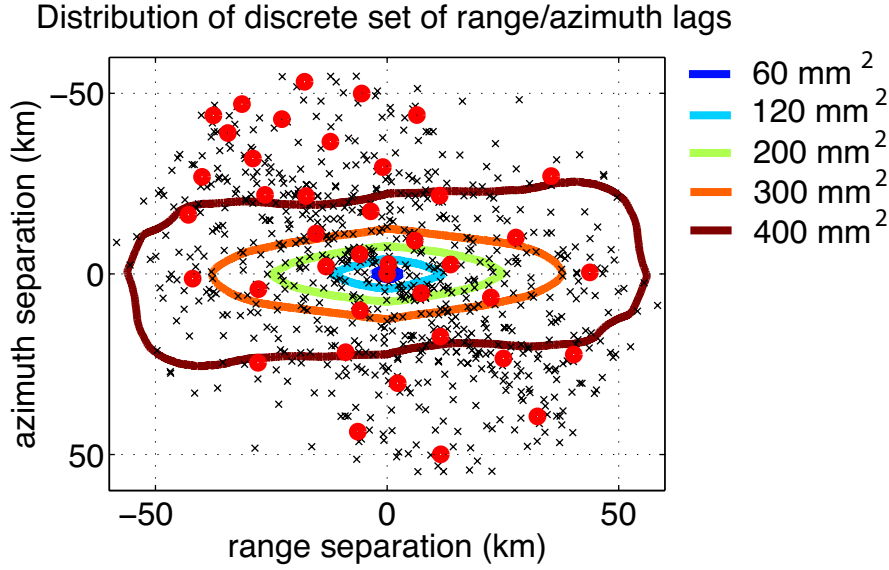


Figure 4.8 Contour map of 2D structure function of the phase residuals. The black crosses denote the range-azimuth separations (lags) of all pairs of GPS sites. The red circles indicate the locations $\{\mathbf{R}_k\}$ where the 2D function is estimated by averaging products of GPS ZWD data whose spatial separations are close to the designated points.

We let $\hat{D}_l(\mathbf{R}_k, t_i)$ denote that GPS ZWD-derived estimate of the 2D structure function at location \mathbf{R}_k , computed as follows

$$\hat{D}_l(\mathbf{R}_k) = \frac{1}{|S(\mathbf{R}_k)|} \sum_{(a,b) \in S(\mathbf{R}_k)} |S(\mathbf{R}_k)| (l_{wet}^{GPS,z}(\rho_a) - l_{wet}^{GPS,z}(\rho_b))^2 \quad (4.30)$$

where

$$S(\mathbf{R}_k) = \{(\rho_a, \rho_b) : \rho_a - \rho_b \approx \mathbf{R}_k\} \quad (4.31)$$

Here, $S(\mathbf{R}_k)$ refers to the set of all of GPS site-pairs $\{(\rho_a, \rho_b)\}$ whose difference is approximately equal to \mathbf{R}_k . The number of elements in the set $S(\mathbf{R}_k)$ is denoted $|S(\mathbf{R}_k)|$.

Using this method, we obtained estimates of ZWD difference structure function from GPS shown as red crosses in Figure 4.7(a). At a given \mathbf{R}_k , the red crosses denote $\hat{D}_l(\mathbf{R}_k)$ while the blue circles denote corresponding values from the 2D InSAR atmospheric phase structure function averaged over those range-azimuth lags of the GPS sites contributing to

the estimate of $\hat{D}_l(\mathbf{R}_k)$. We observe a qualitative agreement between the structure function profiles computed from GPS and InSAR. Both profiles seem to follow a $R^{2/3}$ dependence for large spatial scales. In particular, the $2/3$ -dependence starts from $R \sim 2$ km, which is around the thickness of the PBL. At shorter spatial scales, the structure function profile slope is steeper, but does not appear to conform to the expected $5/3$ slope as predicted by (Treuhaft and Lanyi (1987)). We note that short-scale decorrelation noise may impact the shape of the structure function at these scales. In Williams et al. (1998), the authors state that spatial structure functions computed from the SCIGN ZND data they used generally conformed to the Treuhaft-Lanyi model at large scales. RMS InSAR atmospheric phase values computed by Zebker et al. (1997) and Goldstein (1995) also appear to conform to the model. In Hanssen (1998), however, the spatial structure functions from eight interferograms over the Netherlands appear to follow a $5/3$ slope at large scales.

In Figure 4.7(b), we show temporal structure functions computed from the 29 GPS ZWD difference timeseries shown in Figure 3.2(b). We used GPS data acquired in a time window 6 hours long centered on the SAR overpass times to compute these statistics. The temporal structure functions appear to follow $\tau^{2/3}$ for large time separations and this is consistent with the Treuhaft-Lanyi model because, for a typical wind speed of 10 m/s, large time separations correspond to large spatial scales by the frozen-flow hypothesis. Thus, we expect the temporal structure function of ZWD timeseries to follow a $2/3$ -dependence for large time separations. Williams et al. (1998) showed temporal structure functions computed from SCIGN ZND timeseries which conformed to the Treuhaft-Lanyi model at large time-separations.

In Figure 4.9(a), we show rotationally-averaged power spectra computed from the atmospheric phase shown in Figure 3.6. We computed the power spectrum from phase values in a box of pixels $10 \text{ km} \times 10 \text{ km}$ in size in the center of the study area shown in Figure 3.6. We subtracted a low-order polynomial trend from these phase values before computing the PSD. We observe that the empirical PSD generally follows a $-8/3$ slope on a log-log scale, particularly in the range of wavelengths from ~ 500 meters to 1.4 km. In the wavelength range between 1.4 km to about 3 km, the slope approaches $-5/3$ indicating the “flattening” of phase spectra caused by propagation through two-dimensional, instead of 3D, turbulent water-vapor fields, as suggested by Stotskii (1973). At high frequencies, we observe

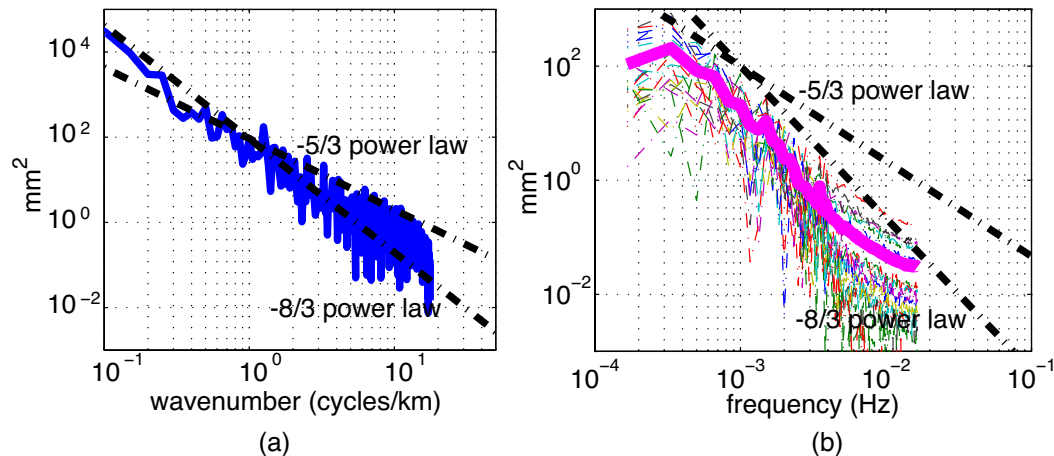


Figure 4.9 (a): Rotationally-averaged spatial power spectrum computed from a $10 \text{ km} \times 10 \text{ km}$ window of detrended InSAR atmospheric phase. The black dashed lines show $-8/3$ and $-5/3$ power laws. (b): Temporal power spectra computed from 29 detrended GPS ZWD timeseries in a 2-hour time window centered on the SAR overpass times.

a similar flattening and this may be due to short-scale decorrelation noise, as noted by Hanssen (1998). In Hanssen (1998), the author computed PSD from eight interferograms over the Netherlands and found slopes of $-8/3$ for wavelengths between 0.5 km to 2 km, slopes of $-5/3$ for scales greater than 2 km and slopes of $-2/3$ for scales less than 0.5 km. Goldstein (1995) observed a PSD computed from phase signatures over the Mojave Desert, CA showing a $-8/3$ -dependence on spatial frequency. In Figure 4.9(b), we show temporal power spectra computed from the 29 GPS ZWD timeseries in a 2-hour time window centered on the SAR overpass times. We detrended the GPS data by subtracting a low-order polynomial from the timeseries prior to computing the spectra. The empirical power spectra display slopes that vary between $-5/3$ to $-8/3$ on a log-log scale. The deviation at low frequencies is most likely the result caused by detrending. Williams et al. (1998) observed a $-5/3$ dependence on the temporal power spectra computed from SCIGN ZND.

From the discussion above, we see that the short-scale fluctuations of GPS ZWD and InSAR atmospheric phase show a power-law dependence in their respective temporal and spatial PSD. We note that the slope of our empirical atmospheric PSD differs from the slope

predicted by Kolmogorov turbulence theory by 1. This is a consequence of the rotational-averaging we applied to the 2D atmospheric phase spectrum. The theoretical slope of the ZWD timeseries spectra is $-8/3$, from Eq. (4.29), while our measured slopes vary between $-8/3$ and $-5/3$. We also observe that corresponding temporal and spatial structure functions computed from these data appear to conform to the Treuhaft-Lanyi structure function model. Thus, we conclude that the short-scale temporal and spatial fluctuations of GPS ZWD and InSAR atmospheric phase are most likely due to turbulent mixing processes of water vapor in the atmosphere.

4.4 Overview of other existing approaches

Existing approaches for correction atmospheric phase distortions in InSAR interferograms can be categorized into two classes: (1) stacking and (2) calibration. Stacking involves averaging multiple independent interferograms, formed from distinct SAR image-pairs, of the same scene. Since the neutral atmosphere is uncorrelated on time scales greater than one day (Hanssen (1998)), the level of atmospheric noise in interferograms can be reduced by a factor of $1/\sqrt{N}$ by averaging N independent interferograms. The reader is referred to Sandwell and Price (1998) and Sandwell and Sichoix (2000) for details on stacking.

Calibration approaches involves direct modeling of the atmospheric phase distortions using independent sources of data, such as PW measurements from GPS. Several authors such as Williams et al. (1998), Hanssen (1998) and Emardson et al. (2003) have proposed using GPS data to correct InSAR atmospheric phase distortions. This proposition is the primary focus of this dissertation and, in the previous section, we have presented an initial demonstration of using GPS ZWD measurements to correct InSAR atmospheric phase distortions. We now review some existing calibration approaches using GPS as well as direct meteorological measurements to reduce atmospheric effects in InSAR images.

Williams et al. (1998) showed that structure functions and power spectra computed from timeseries of ZND obtained from a network of 50 GPS receivers as well as InSAR atmospheric phase RMS fluctuations reported by Zebker et al. (1997) and Goldstein (1995) conformed to the Treuhaft-Lanyi statistical model (Treuhaft and Lanyi (1987)). This suggests that the short-scale fluctuations in GPS and InSAR measurements of wet delay are

turbulence-driven. The authors also demonstrated an altitude-dependence in GPS ZND data they used and they assumed a model of ZND that decreases linearly with height. Williams et al. (1998) did not present InSAR observations of atmospheric phase, however. They did propose, however, to reduce atmospheric distortions in InSAR by using GPS ZWD estimates. Williams et al. (1998) point out that the low spatial density of continuous GPS networks compared to the scales of water vapor irregularities and resolution of InSAR may not necessarily preclude using GPS ZWD measurements to correct atmospheric artifacts in InSAR. The power-law dependence of the atmospheric phase PSD indicates that the largest amplitudes of atmospheric phase distortions are contained at low frequencies. Therefore, even spatially-sparse ZWD observations from GPS can be used to correct these long-wavelength components. Williams et al. (1998) note further that the ability of GPS ZWD measurements to reduce atmospheric phase distortions also depends on the effectiveness of the interpolator used to predict delay at an unsampled location as well as on the accuracy of the measurements themselves. Through a 1D simulation, Williams et al. (1998) found that when the accuracy of the control points was significantly less than the RMS variations of the target profile, the improvement in interpolation error approached $1/\sqrt{N}$ where N denotes the number of control points used in the interpolation. In contrast, when the accuracy of the measurements were on the order of the RMS variations of the profile, the improvement did not decrease below 20% even as the number of control points were increased. The authors note that, in the two-dimensional case, the actual distribution of control points impacts the predictive performance of the interpolator. Finally, Williams et al. (1998) found that kriging interpolation and bilinear interpolation yields lower residuals than inverse distance weighting (IDW) interpolation.

Hanssen (1998) compared the atmospheric phase signatures from a tandem interferogram (acquired from SAR observations one day apart) with GPS ZWD differences acquired from four receivers in the study area. He reported an RMS difference of 3 mm between the GPS and InSAR measurements. The author also interpolated the point measurements from GPS using isotropic harmonic spline interpolation and found a minimal reduction in atmospheric phase dispersion after correction with the interpolated map. Hanssen mentioned that the effectiveness of interpolating a IWV difference map from GPS depends on the spatial density of GPS observations. However, the upper limit on the spatial variation of ZWD

reproducible from GPS depends on the width of the averaging cone. The author also noted that interpolating ZWD measurements from a GPS network can introduce ambiguous short wavelength variations due to limitations of the interpolator and the irregular distribution of the receivers.

In another calibratory approach, Wadge et al. (2002) reported used forward models of atmospheric flow over Mt. Etna to calculate a three-dimensional water vapor field at two SAR overpass times from which they obtained an estimate of InSAR atmospheric phase. They also compared their result with measurements of wet delay acquired from a network of GPS receivers on the mountain. The authors note that standard numerical weather prediction models cannot adequately resolve the spatial variability of water vapor at the resolution of InSAR and that this variability, as observed in InSAR atmospheric phase distortions, is strong over Mt. Etna due to variable thickness of the neutral atmosphere and complex local air flow over the mountain. They used a higher-resolution NH3D model that incorporates orography of the mountain. This model was initialized using radiosonde data acquired 150 km away from the mountain and 5 hours before the SAR overpass times. The authors report that the range of spatial variation of ZWD differences produced by the model was 50% greater than the variation observed from InSAR. The GPS and InSAR data agreed to within 19 mm and subtracting the forward model output from the InSAR data reduced the RMS phase fluctuations from 46 mm to 18 mm. The authors note that the quality of the NH3D prediction is limited by errors in the radiosonde data used to initialize the model.

Delacourt et al. (1998) used a semi-empirical model for tropospheric delay, originally developed for GPS to correct atmospheric phase artifacts in a SAR interferogram also over Mt. Etna. This model assumed a “static” troposphere and used ground-based measurements of pressure, temperature and humidity to model wet delay. The model contained two parameters calibrated for their case study from radiosonde soundings. The authors corrected atmospheric phase signatures obtained from 20 interferograms using their model and found an average RMS residual of 28 mm. The authors interpret the residual atmospheric phase as due to temporal inhomogeneities of water vapor which the ground-based model cannot resolve.

Emardson et al. (2003) used ZWD measurements from the SCIGN GPS network to infer the covariance matrix of InSAR atmospheric phase distortions at temporal and spatial scales

commensurate with InSAR studies of deformation. However, the authors do not compare GPS-derived statistics of ZWD with actual InSAR observations nor do they attempt to use the ZWD measurements to correct InSAR atmospheric phase. The authors mention that GPS cannot measure atmospheric phase at the resolution of InSAR because of the “cone-averaging” effect in GPS estimation of ZWD. The authors analyzed timeseries of ZND from 126 SCIGN GPS stations over a two year period. They computed empirical structure functions from data obtained from different pairs of GPS receivers and found that the ZWD data become uncorrelated at time scales > 1 day. Using a timescale of 7 days, they modeled the empirical structure functions as $c \|\mathbf{R}\|^\alpha + kz$ where $\|\mathbf{R}\|$ denotes horizontal length scale determined by separation of the GPS receivers and z is the height difference between receivers. The authors found that the structure function dependence on z was negligible compared to the length scale dependence. However, they found also that mean vertical stratification of the neutral atmosphere, modeled by the z -dependence in the above, remained correlated over time scales > 1 day compared to horizontal variations that decorrelate at shorter time scales.

Li et al. (2006) mention that the reduction of atmospheric phase distortions in InSAR using GPS is limited by: (1) the spatial resolution of GPS ZWD observations and (2) limitations imposed by the choice of spatial interpolator. The authors present a statistical minimum-variance interpolator, similar to kriging, for estimating the atmospheric phase using GPS ZWD. The authors used the structure model derived in Emardson et al. (2003) to characterize the covariance matrix of ZWD acquired from the SCIGN GPS network. They assumed that this statistical model also describes atmospheric phase variations observed in InSAR interferograms. Through a cross-validation procedure, the authors found that their estimator reproduced GPS ZWD measurements with lower error compared to simple IDW interpolation. The authors test their method of three interferograms over Southern California and achieved about 1.2 mm atmospheric phase RMS reduction averaged over all three cases. The authors note that their estimator cannot reproduce atmospheric phase variations with wavelengths shorter than the GPS station spacing.

In all the studies mentioned above, the authors used independent data from GPS, ground-based meteorological measurements and radiosondes to either explicitly model InSAR atmospheric phase or statistically characterize its fluctuations.

In Wadge et al. (2002), however, the authors showed dynamical models of atmospheric motions can be applied to meteorological data acquired at times around the SAR overpass to infer atmospheric phase distortions in an interferogram. Extending this idea, a major focus of this work is to use GPS ZWD measurements acquired before and after the SAR overpass times to improve the estimation of InSAR atmospheric phase distortions.

In studies concerning explicit interpolation of GPS ZWD measurements acquired from a network, Emardson et al. (2003) note that the minimum wavelength of atmospheric phase variations that can be reproduced is determined by the inter-site spacing as well as the cone-averaging effect from GPS estimation of ZWD. Thus, GPS data are most suitable to correct longer-wavelength and higher power components of atmospheric phase.

Chapter 5

Estimating atmospheric phase signatures from GPS

5.1 Introduction

In this chapter, we present a simple method to reduce InSAR atmospheric phase distortions using GPS ZWD measurements. InSAR atmospheric phase, Figure 3.6, can be regarded as a “snapshot” of the difference between the states of the neutral atmosphere at the two overpass times. The GPS ZWD measurements acquired at the SAR overpass times, shown in Figure 3.2(b), are point measurements of the difference atmospheric phase field limited to the locations of the 29 receivers. The InSAR phases, in contrast, are spatially resolved to 40 meters over the entire image field. Therefore, to reduce InSAR atmospheric phase distortions, we need to accurately infer ZWD at locations not coincident with the available GPS stations. Here we examine interpolation methods to estimate ZWD between the GPS locations, but still limited to the precise SAR overpass times. In Chapters 6 and 7 following, we will present two algorithms that use ZWD measurements acquired before and after the SAR overpass time to estimate a ZWD difference map that better approximates the observed atmospheric phase distortions.

We saw in Chapter 4 that the atmospheric phase observed in the radar interferogram shows spatial variability most likely due to two distinct physical processes: (1) topographic-modulation of the mean ZWD and (2) turbulent mixing of water vapor in the atmosphere. In

this chapter, we use the GPS ZWD point measurements to estimate two maps, one showing topography-dependent spatial variations of wet delay and another approximating the variations due to turbulent mixing. Each of these maps is proportional to that component of total column water vapor from Eq. (4.13) at the SAR overpass times. Thus, in this dissertation, we refer to the ZWD map as estimated from the sparse GPS data as an *integrated water vapor (I WV) map* and the difference of two I WV maps at the two SAR overpass times as an *I WV difference map*. We will show that these maps can be used to reduce the global RMS of atmospheric phase distortions observed in the interferogram.

5.2 Topography-dependent atmospheric phase

We have previously shown that GPS and InSAR delay data display similar altitude dependence (Figure 4.4(b)). We now estimate this component of delay variation by fitting a model of the vertical profile of neutral atmospheric delay to the GPS ZWD measurements.

The dependence of GPS ZWD on altitude has been observed previously by Elosegui et al. (1998). The authors assumed an exponential law for water vapor density to model the average vertical refractivity profile. Following this approach, we adopt a more general model,

$$l_{vert}(z) = Ce^{-\alpha z} + z\alpha Ce^{-\alpha z} + l_{min} \quad (5.1)$$

The bias l_{min} above refers to the ZWD recorded at the highest-altitude station and equaled 31.2 mm for data acquired at the station WLSN on February 5th, 2000 and 61.2 mm for data obtained on November 27th, 1999. We found empirically that the above model fits the GPS ZWD observations better, at lower altitudes, than a simple exponential law. It is important to correct the ZWD height dependence accurately because we need to remove topography-related trends. Then, the residual fluctuations can be interpreted as turbulent variations of water vapor. This motivates the use of the additional terms apart from the first term in Eq. (5.1). In particular, since most GPS observations of ZWD occur at altitudes less than 600 meters, we included the bias term l_{min} to minimize the weight of the sole high-altitude wet delay observation acquired at station WLSN in fitting Eq. (5.1) to ZWD data measured at all other low-altitude GPS sites.

Figure 5.1 shows the resulting fit to the GPS ZWD data. The fit parameters are shown in Table 5.1. We also show in Table 5.1 the goodness-of-fit of Eq. (5.1) $l_{vert}(z_i)$ to the GPS ZWD observations $l_{wet}^{GPS,z}(z_k, t_i)$ at the SAR overpass times in terms of the reduced chi-square statistic

$$\chi_{27}^2 = (1/27) \sum_{k=1}^{29} \frac{(l_{wet}^{GPS,z}(z_k, t_i) - l_{vert}(z_k))^2}{\sigma_{GPS}^2} \quad t_i = \{t_1, t_2\} \quad (5.2)$$

The factor of $1/27$ in the above corresponds to 27 degrees of freedom from 29 GPS observations and 2 model parameters, and σ_{GPS} denotes the GPS ZWD estimation error of 4 mm. The parameter C in Eq. (5.1) is proportional to the amount of precipitable water vapor measured at sea-level while α denotes the decay rate of the vertical water vapor profile with height. This rate is probably related to the scale height of the troposphere. While explicit determination of the tropospheric scale height from GPS ZWD data is outside the scope of this work, we note here that the approximately equal decay rate values on both dates shown in Table 5.1 should not be interpreted to indicate similar atmospheric states on both dates. Rather, the fits are primarily constrained by most of the ZWD measurements at lower altitudes, and these measurements exhibit similar altitude-dependence (Figure 5.1). Excluding the bias term l_{min} from the model, we find $C = 114.1$ mm, $\alpha = 1.7$ km⁻¹ for the fit to data on February 5th, 2000 and $C = 100.7$ mm, $\alpha = 0.79$ km⁻¹ for the fit to ZWD observations acquired on November 27th, 1999. In this study, we use the model in Eq. (5.1) with the parameters shown in Table 5.1 to correct altitude-dependent ZWD in GPS data and the topography-dependent component of InSAR atmospheric phase.

In Table 5.2, we show parameters inferred from a direct fit of the model in Eq. (5.1) to the observed InSAR atmospheric phase. The resulting fit is shown in black in Figure 5.1(b). The RMS atmospheric phase fluctuation after removing the topography-dependent model is 8.6 mm, compared to 16.1 mm when the topography correction is ignored.

We use the parameters C and α inferred from the fits to the GPS ZWD data and a DEM of

Table 5.1 Parameter estimates and goodness-of-fit for altitude-dependent atmospheric delay model from GPS ZWD at the SAR overpass times

	C (mm)	α (km^{-1})	l_{min} (mm)	χ_{27}^2
t_1 , Feb. 5th 2000	83.8	2.38	31.2	2.78
t_2 , Nov 27th 1999	39.5	2.35	61.2	2.40

Table 5.2 Parameter estimates for altitude-dependent atmospheric phase inferred from a direct fit to observed InSAR phase

	C (mm)	α (km^{-1})	l_{min} (mm)
t_1 , Feb. 5th 2000	110.0	1.3	30
t_2 , Nov 27th 1999	66.7	0.5	0

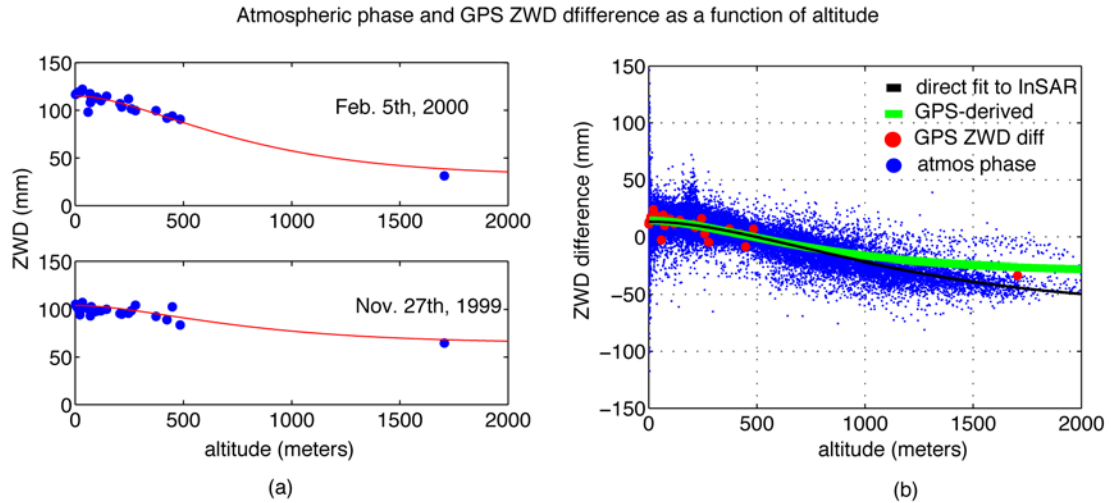


Figure 5.1 (a): GPS zenith wet delay measurements (blue) plotted as a function of station altitude at the SAR overpass times on Feb. 5th, 2000 (top) and Nov. 27th, 1999 (bottom). Shown in red are least squares fits of Eq. (5.1) to the GPS ZWD data at the two SAR overpass times. (b): InSAR atmospheric phase (blue) and GPS ZWD differences (red) as a function of altitude. In green, we show a topography-dependent IWBV difference map inferred using model parameter estimates shown in Table 5.1 and a DEM of the area. This map is depicted in Figure 5.2(b). In black, we show a topography-dependent model inferred from a direct fit of Eq. (5.1) to the InSAR atmospheric phase

the area to estimate topographic-dependence of atmospheric phase, and the result is shown in Figure 5.2(a). We subtract this topography-dependent atmospheric phase model, Figure 5.2(a), from the total atmospheric phase observed by InSAR (Figure 5.2(b)) to yield the turbulently-mixed atmospheric phase shown in Figure 5.2(c). As mentioned above, removing the topography-dependent component of spatial variation reduces global root-mean-square (rms) atmospheric phase fluctuations from 16.1 mm to 8.6 mm, a 46% reduction. This is the single most important correction to apply to interferograms to compensate for atmospheric phase effects.

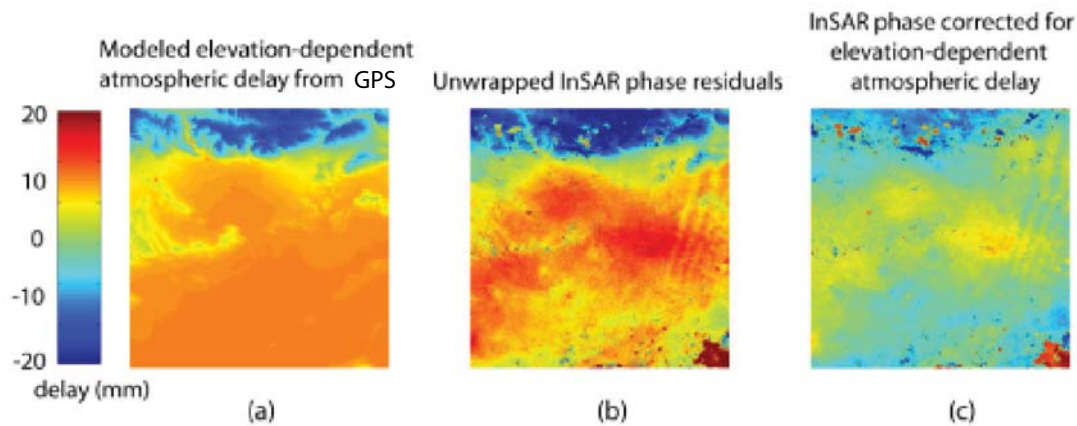


Figure 5.2 (a): Map of altitude-dependent ZWD delay difference derived from parameters obtained from least-squares fit of refractivity model to GPS ZWD measurements. (b): Unwrapped atmospheric phase (box in Figure 3.6, Chapter 3) showing altitude-dependence. (c): Turbulently-mixed atmospheric phase

5.3 Magnitude and correlation of the turbulent component

After removing the component of spatial variation due to vertical stratification of the neutral atmosphere, the GPS and InSAR residuals represent measurements of the turbulently-mixed portion of ZWD variability. Here we compare these residuals in terms of their magnitude and spatial correlation. In the following section and in Chapter 6, we will use the results of this statistical comparison to reduce turbulently-mixed InSAR atmospheric phase using GPS ZWD measurements.

In Figure 5.3, we plot GPS ZWD differences and turbulently-mixed atmospheric phase at the positions of the GPS receivers. We see that GPS ZWD measurements and turbulently-mixed atmospheric phase are quite similar. The GPS ZWD residuals at the 29 receiver locations constrain the turbulently-mixed atmospheric phase field from InSAR. To quantify

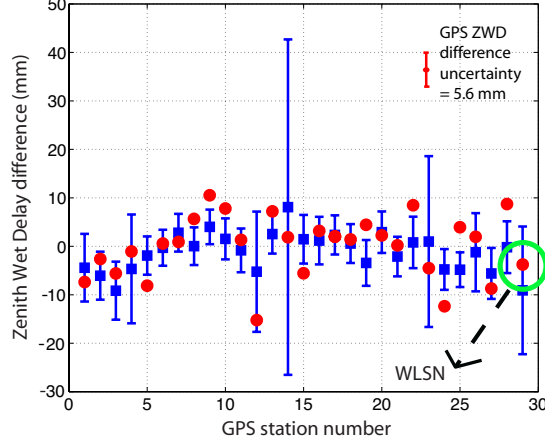


Figure 5.3 Comparison of GPS ZWD differences (red circles) and colocated turbulently-mixed atmospheric phase measurements (blue squares) from the data shown in Figure 5.2(c). The blue squares indicate phase measurements averaged in 8 km by 8 km blocks, so that the results will be comparable to GPS zenith wet delay estimates which combine many observations over an inverted cone above the receiver. The blue errorbars denote standard deviation of the phase samples in the 8 km by 8 km blocks.

this constraint, we start with the formal correlation of these data, γ , defined as follows

$$\gamma = \frac{\langle (l_{wet}^{GPS,z}(x_a, y_a, t_1) - l_{wet}^{GPS,z}(x_a, y_a, t_2)) \Delta l_{wet}^{INSAR}(x_a, y_a) \rangle}{\sqrt{\langle (l_{wet}^{GPS,z}(x_a, y_a, t_1) - l_{wet}^{GPS,z}(x_a, y_a, t_2))^2 \rangle \langle \Delta l_{wet}^{INSAR}(x_a, y_a)^2 \rangle}} \quad (5.3)$$

where t_1 and t_2 are the SAR overpass times, (x_a, y_a) is a location of a GPS receiver and $\Delta l_{wet}^{INSAR} = \frac{\phi_{wet}^{INSAR} \lambda \cos \theta}{4\pi}$. We assume that GPS ZWD difference data and turbulently-mixed atmospheric phase from InSAR are both noisy measurements of actual ZWD difference between the SAR overpass times, $\Delta l_{wet} = l_{wet}(x_a, y_a, t_1) - l_{wet}(x_a, y_a, t_2)$.

$$\begin{aligned} \Delta l_{wet}^{INSAR}(x_i, y_i) &= \Delta l_{wet} + n_{SAR} \\ l_{wet}^{GPS,z}(x_a, y_a, t_1) - l_{wet}^{GPS,z}(x_a, y_a, t_2) &= \Delta l_{wet} + n_{GPS} \end{aligned}$$

where n_{SAR} and n_{GPS} are zero-mean and mutually-uncorrelated measurement noise with

variances σ_{SAR}^2 and σ_{GPS}^2 respectively. Inserting the above into Eq. (5.3), the correlation coefficient is expressed as follows

$$\gamma = \frac{1}{\sqrt{1 + \frac{\sigma_{SAR}^2 \sigma_{GPS}^2}{\Delta l_{wet}^4} + \frac{\sigma_{SAR}^2 + \sigma_{GPS}^2}{\Delta l_{wet}^2}}} \quad (5.4)$$

GPS ZWD estimation error, σ_{GPS} , is available from GIPSY processing of GPS carrier phase observables. The uncertainty in the GPS ZWD estimates was about 4 mm. The red error bar in Figure 5.3 shows the ZWD difference estimation error for data processed from each GPS receiver. Assuming the ZWDs are uncorrelated at the two SAR overpass times, the individual ZWD estimation errors of 4 mm sum together to give a ZWD difference uncertainty of $\sqrt{2} \times 4 = 5.6$ mm, as shown in Figure 5.3. The blue errorbars in Figure 5.3 indicate the standard deviation of atmospheric phase samples within a $8 \text{ km} \times 8 \text{ km}$ averaging window. If we assume that the variance of noise in the phase measurements, σ_{SAR}^2 , is negligibly small due to the averaging of many samples of turbulently-mixed atmospheric phase in an 8 km by 8 km region, then

$$\gamma = \frac{1}{\sqrt{1 + \frac{\sigma_{GPS}^2}{\Delta l_{wet}^2}}} = \frac{1}{\sqrt{1 + \frac{1}{SNR}}} \quad (5.5)$$

where $SNR = \frac{\Delta l_{wet}^2}{\sigma_{GPS}^2}$, the ratio of ZWD difference magnitude squared to GPS estimation error variance. Figure 5.4 shows a plot of Eq. (5.5) and we note that the correlation between GPS ZWD difference and InSAR turbulently-mixed atmospheric phase increases with increasing SNR. The linear correlation coefficient between GPS ZWD and the turbulently-mixed atmospheric phase (Figure 5.3) was 0.54. At this level of correlation, $SNR \approx 0.5$ from Figure 5.4.

The statistical significance of the linear correlation coefficient value of 0.54 can be quantified by computing the following t-statistic (Press et al. (1986))

$$t = \gamma \sqrt{\frac{N-2}{1-\gamma^2}} \quad (5.6)$$

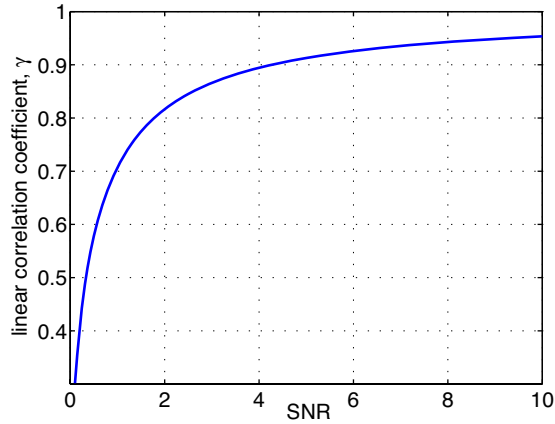


Figure 5.4 Relationship between the linear correlation coefficient and SNR assuming the additive-noise model of GPS and InSAR observations of atmospheric delay.

where $N = 29$, the number of GPS sites in the study area. With $\gamma = 0.54$, $t = 3.33$. If the InSAR turbulently-mixed atmospheric phase and GPS ZWD measurements are uncorrelated and normally-distributed, the statistic above is distributed according to the two-tailed t-distribution, with $N - 2 = 27$ degrees of freedom. At a significance level of 0.01, the critical value is 2.771 and, thus, the hypothesis of no correlation between the two datasets is unlikely. Therefore, the linear correlation of 0.54 between InSAR atmospheric phase and GPS measurements of ZWD is statistically significant. Such a high degree of correlation confirms that GPS ZWD measurements, corrected for vertically-dependent trends, represent point measurements of turbulently-mixed atmospheric phase from InSAR.

We now examine the spatial correlation of GPS ZWD measurements that have been corrected for altitude-dependence. In Figure 5.5(a), we present the 2D spatial autocorrelation function measured directly from the turbulently-mixed InSAR atmospheric phase. We compare this result with the spatial correlation function of ZWD differences derived from the GPS measurements. We derive the 2D GPS-derived spatial autocorrelation function of ZWD by fitting a smooth function to a limited set of autocorrelation estimates obtained using the method described in Chapter 4, but computing autocorrelation instead of structure function values. The functional form we use to model the spatial autocorrelation function of wet delay derives from geostatistical variogram models. In particular, we choose to

model the spatial autocorrelation function of ZWD as a product of an exponential correlation model and a “hole-effect” model to approximate the observed spatial autocorrelation function of the InSAR turbulently-mixed atmospheric phase (Goovaerts (1997)),

$$\hat{C}(R_x, R_y) = C e^{-\sqrt{\left(\frac{R_x}{\tau_x}\right)^2 + \left(\frac{R_y}{\tau_y}\right)^2}} \cos\left(\pi\left(\frac{R_x}{W_x} + \frac{R_y}{W_y}\right)\right) \quad (5.7)$$

We estimate the model parameters τ_x , τ_y , W_x , W_y and C from the best fit of the model above to the limited set of autocorrelation estimates from the GPS ZWD data at each SAR overpass time. We construct two empirical autocorrelation function models, one each for ZWD data from GPS acquired on November 27th 1999 and February 5th 2000 respectively, and form a two-acquisition model of the spatial autocorrelation function of atmospheric phase distortions. Table 5.3 displays the least-squares solution for model parameters. The parameter set, τ_x , τ_y , W_x , W_y and C , reflects the spatial correlation of neutral atmospheric path delays between GPS sites on each SAR overpass time. We observe that the model parameter estimates are markedly different for the two dates considered, implying dissimilar inter-site ZWD correlations on both dates. Interpreting the theoretical structure of spatial correlation of water-vapor signal delays from GPS is outside the scope of this report and remains for future work.

In Figure 5.5(b), we show the spatial autocorrelation function inferred from GPS ZWD. Figure 5.5 shows that our model for the autocorrelation function, derived by fitting Eq. (5.7) to sparse autocorrelation estimates from the GPS data, agrees with the empirical autocorrelation computed from the turbulently-mixed atmospheric phase. Note that our choice of model is motivated solely by the need to interpolate the sparse network of GPS ZWD data to a regular two-dimensional grid, and not to validate theoretical autocorrelation models of water-vapor-induced delays with GPS and InSAR observations. Rather, a reasonable autocorrelation function model that agrees with observations allows us to estimate the turbulently-mixed atmospheric phase artifacts observed in SAR interferograms.

The relatively high correlation observed between GPS ZWD measurements and InSAR

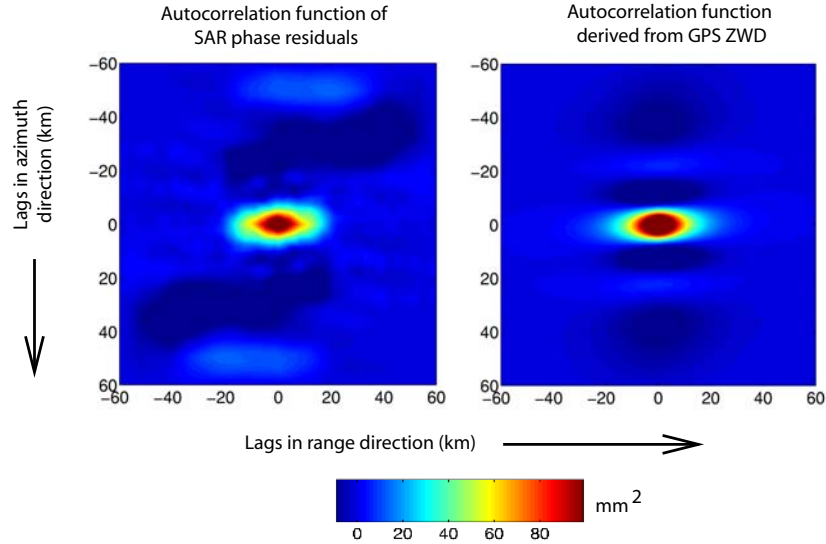


Figure 5.5 (a): 2D spatial autocorrelation function of turbulently-mixed atmospheric phase computed from the InSAR phase (b): 2D autocorrelation function model inferred from least-squares regression of Eq. (5.7) of autocorrelation function estimates computed from the sparse GPS ZWD measurements.

phase residuals, plus the close correspondence between the spatial autocorrelation functions inferred from these data, permits us to estimate an IWV difference map from the GPS ZWD measurements at the SAR overpass times. We will use this map to reduce the distortions caused by turbulently-mixed InSAR atmospheric phase variations.

5.4 Estimating the turbulently-mixed atmospheric phase

We wish to reduce the turbulent component of InSAR atmospheric phase variations by subtracting a GPS-derived IWV difference map approximating the short-scale fluctuations. To estimate this map at the InSAR resolution, we must model the ZWD at locations not covered by the sparse GPS receiver network. Our approach follows from the characterization of turbulence-driven 3D wet refractivity fluctuations as a stochastic process with a structure

Table 5.3 Spatial autocorrelation parameters of turbulently-mixed atmospheric phase inferred from irregularly-spaced GPS autocorrelation samples

	C (mm ²)	τ_x (km)	τ_y (km)	W_x (km)	W_y (km)
t_1 , Feb. 5th 2000	0.11	41.54	13.19	42.5	381.9
t_2 , Nov 27th 1999	0.75	7.92	7.86	12.83	363.2

function and PSD derived from Kolmogorov turbulence theory, as we described in Chapter 4. We use a statistical interpolation method, called *kriging* (see Goovaerts (1997) for an overview), to generate a minimum-variance estimate of ZWD at unsampled locations using the 29 available GPS ZWD measurements. We apply this interpolation twice, for data sets acquired at both SAR overpass times, and compute the difference of the results.

The kriging algorithm forms an estimate of ZWD $\hat{l}_{wet}(x_0, y_0)$ at an unsampled location (x_0, y_0) using a linear combination of the 29 available GPS ZWD measurements,

$$\hat{l}_{wet}(x_0, y_0) = \mathbf{w}^T \mathbf{l}_{wet}^{GPS,z}, \quad \mathbf{w} = \begin{bmatrix} w_1 \\ \cdot \\ \cdot \\ \cdot \\ w_{29} \end{bmatrix}, \quad \mathbf{l}_{wet}^{GPS,z} = \begin{bmatrix} l_{wet}^{GPS,z}(x_1, y_1) \\ \cdot \\ \cdot \\ \cdot \\ l_{wet}^{GPS,z}(x_{29}, y_{29}) \end{bmatrix} \quad (5.8)$$

The weights w_i are chosen to minimize the mean-squared-error between the estimate \hat{l}_{wet} and the random process l_{wet}

$$\mathbf{w} = \min_{\mathbf{w}}^{-1} \langle (l_{wet} - \mathbf{w}^T \mathbf{l}_{wet}^{GPS,z})^2 \rangle, \quad \text{such that } \sum w_i = 1 \quad (5.9)$$

The constraint $\sum w_i = 1$ is to ensure lack of bias in the estimator. It can be shown

(Goovaerts (1997)) that the optimal set of weights is given by

$$\mathbf{w} = \mathbf{C}^{-1} \mathbf{d} \quad (5.10)$$

where

$$[\mathbf{C}]_{ij} = \langle l_{wet}^{GPS,z}(x_i, y_i) l_{wet}^{GPS,z}(x_j, y_j) \rangle = C(x_i - x_j, y_i - y_j) \quad (5.11)$$

and

$$d_i = \langle l_{wet}(x_0, y_0) l_{wet}^{GPS,z}(x_i, y_i) \rangle = C(x_0 - x_i, y_0 - y_i) \quad (5.12)$$

In the above, $C(x, y)$ is the spatial autocorrelation function of the stochastic process l_{wet} . We assume that the GPS ZWD at both SAR overpass times and InSAR turbulently-mixed atmospheric phase are samples of two, mutually uncorrelated stochastic processes with a common autocorrelation function C . We use the spatial correlation function computed directly for the turbulently-mixed atmospheric phase, as shown in Figure 5.5(a). In principle, the theoretical forms of power spectra predicted by Kolmogorov theory can be used to obtain a correlation model for kriging. However, the Kolmogorov model is idealized in that the spatial correlation of the ZWD field is assumed to be isotropic. Neglecting directional-dependence in the assumed autocorrelation model may result in an inferred map that poorly approximates the observed InSAR turbulently-mixed atmospheric phase. In general, anisotropic turbulent variations have been studied (Celani and Seminara (2006)) but treatment of the physical basis underlying anisotropic water vapor spectra is beyond the scope of this work.

In Figure 5.6(b), we show a ZWD difference map generated using kriging from the 29 GPS measurements at the two SAR overpass times. Figure 5.6(c) shows the error magnitude resulting from subtracting the interpolated map from the observed turbulently-mixed atmospheric phase, Figure 5.6(a). The RMS residual of the turbulently-mixed atmospheric phase is 8.6 mm, and after correction with the IWV difference map generated by krig interpolation, we observe a 0.5 mm reduction. But this reduction in RMS residual is for the full range of wavelengths in the PSD of turbulently-mixed atmospheric phase. At higher spatial frequencies in particular, the fluctuations are dominated by short-spatial-scale variations due to decorrelation as well as possible interpolation errors. Furthermore, there is

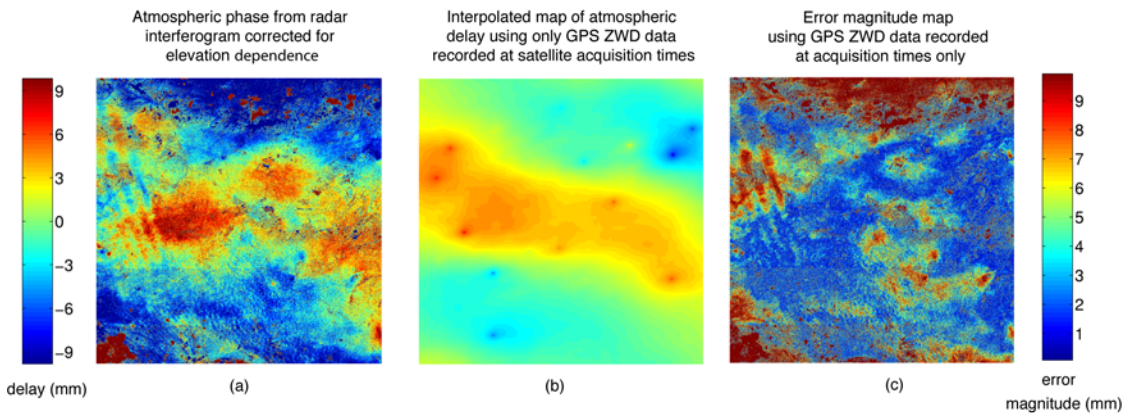


Figure 5.6 (a): Turbulently-mixed InSAR atmospheric phase over study area. (b): IWV difference map kriging interpolated from the 29 GPS ZWD difference measurements acquired at the SAR overpass times. (c): error magnitude after correcting the turbulently-mixed atmospheric phase (a) with IWV difference map (b)

an upper bound on the spatial frequency of turbulently-mixed atmospheric phase variations that can be reproduced by interpolation of the GPS ZWD measurements. The IWV difference maps can therefore only be compared with turbulently-mixed atmospheric phase variations at spatial frequencies less than this maximum, since fluctuations at higher frequencies can be considered as noise.

The maximum spatial frequency of the useful phase signatures is about $1/8 \text{ km}^{-1}$. This value of the cut-off frequency follows from noting that the measurements of ZWD from GPS are actually averages of the atmosphere in an inverted cone, with an 8 km diameter at its base assuming a tropospheric scale height of 1 km (Figure, 3.1, Chapter 3). Therefore, we filter out the shorter-scale variations using a box-car filter of dimensions $8 \text{ km} \times 8 \text{ km}$, as suggested by the GPS averaging cone. This smoothing operation is desired if the deformation map can be averaged to similar resolution and still maintain geophysical significance, as is the case quite often. After filtering, the RMS residual of turbulently-mixed atmospheric phase was 4.7 mm. Subtracting the (similarly filtered) kriged map from the filtered phase yielded a residual RMS of 3.9 mm. Thus, with prior smoothing, we achieve a 0.8 mm reduction in RMS residual, compared to 0.5 mm without filtering. This suggests

Table 5.4 RMS atmospheric phase fluctuations before and after GPS-derived corrections

Atmospheric phase distortions (mm RMS)	16.1	
	Entire spectrum	Low-pass filtered
Corrected for topography-dependence (mm RMS)	8.6	4.7
Corrected for turbulently-mixed variations (mm RMS)	8.1	3.9

that “kriging” sparse data introduces into the IWV difference maps spurious high-frequency artifacts which limit the RMS phase fluctuation reduction.

In Table 5.4, we summarize our results we obtained for this approach to reduce turbulently-mixed atmospheric phase using GPS ZWD measurements.

5.5 Summary

In this chapter, we have used GPS ZWD measurements acquired at the SAR overpass times to reduce atmospheric phase distortions in a radar interferogram. As GPS and InSAR are similarly sensitive to the neutral atmosphere, and water vapor in particular, our approach to reducing InSAR atmospheric phase distortions focused on reproducing two types of spatial variations of these signatures from GPS ZWD measurements. Specifically, we used GPS ZWD measurements to estimate the topography-dependent (Figure 5.2) and turbulently-mixed (Figure 5.6) components of atmospheric phase. Correcting the observed InSAR atmospheric phase with the topography-dependent estimate yielded a reduction in RMS phase fluctuations of about 7.5 mm. In other studies concerning calibration approaches using ground-based meteorological data, various authors have shown that standard models used to extrapolate surface measurements of pressure, temperature and humidity in the vertical can only be used to account for the topography-dependent atmospheric phase. In these studies, the accuracy of the modeled atmospheric phase artifacts depends on the quality of the various meteorological data used in the models. Here, we have shown that GPS ZWD

measurements can be used to accurately estimate the topography-dependent component of atmospheric phase spatial variation.

The extrapolation models used by the authors in other studies mentioned in Chapter 4 regard the lower atmosphere as static and, consequently, short-scale atmospheric phase variations caused by turbulent mixing of water vapor cannot be adequately predicted using ground-based meteorological measurements. Here, we estimated the turbulently-mixed atmospheric phase component using a statistical approach (kriging) similar to that used by Li et al. (2006). As shown in Table 5.4, we achieved a 0.5 mm reduction in turbulently-mixed atmospheric phase distortion RMS error. We noted a slightly larger reduction when prior smoothing was applied. This supports the observation made by Li et al. (2006), Emardson et al. (2003) and Hanssen (1998) that the minimum wavelength of variation reproducible from interpolating GPS ZWD measurements is determined by the width of the averaging cone used in GPS data reduction. Also, we find that interpolation can introduce spurious high-frequency variations in the results which can contaminate the phase residuals after correction. The accuracy of interpolating GPS ZWD measurements has been repeatedly shown to be limited by the sparsity of the network, which sets a limit on our ability to compensate InSAR data for atmospheric effects. In the following chapters, we propose two algorithms that use GPS measurements of ZWD acquired before and after the SAR overpass times to increase the effective sampling density of GPS observations.

Chapter 6

The “frozen-flow” algorithm

6.1 Introduction

In this chapter, we present an algorithm to derive a ZWD difference map from GPS time-series exhibiting less turbulently-mixed InSAR atmospheric phase than with our approach in chapter 5. Here, we concentrate on the turbulence-driven component of atmospheric phase spatial variation. As shown in chapter 5, the topography-dependent component is fairly well approximated by modeling the vertical-dependence of GPS ZWD data acquired only at the SAR overpass times, because the vertical stratification of the neutral atmosphere varies slowly relative to the fluctuations caused by turbulent mixing. In this and the following chapters, we use GPS ZWD timeseries that have already been corrected for vertical-dependence.

In our algorithm, we follow the approach of Chapter 5 and model turbulent wet refractivity fluctuations, and consequently the turbulently-mixed atmospheric phase, as a stochastic process. We assume that this process is characterized by the spatial autocorrelation function as shown in Figure 5.5(a). However, in addition we allow a temporal evolution of this random wet refractivity field. Time-dependence is modeled here by the frozen-flow hypothesis, introduced previously in Chapter 4. The SCIGN GPS network tracks the refractivity field over time by measuring timeseries of ZWD at those receiver locations in Figure 3.2(a). In the algorithm presented in this chapter, we leverage the dense temporal sampling of GPS ZWD observations, via the frozen-flow hypothesis, to infer denser networks of

point measurements from GPS for inferring IWV maps. We hereafter refer to these ZWD point measurements in a network as *control points*. We noted in the previous chapter that the accuracy of interpolating the ZWD difference maps is limited by the sparsity of the GPS network. Our method here incorporates additional GPS ZWD data recorded prior to and after the individual SAR overpass times into the spatial interpolation procedure, resulting in a denser network of control points. The additional GPS measurements enable estimation of IWV difference maps that better match (in terms of RMS residual) the turbulently-mixed atmospheric phase distortions observed in the InSAR data (Figure 5.6(a)).

In Chapter 4, we used the frozen-flow hypothesis to relate temporal statistics computed from GPS ZWD timeseries to Kolmogorov theory. Several authors have used frozen-flow to relate temporal and spatial fluctuations of wet delay. Treuhaft and Lanyi (1987) used the hypothesis assuming a wind speed of 8 m/s to compare the temporal statistics computed from VLBI observables with their spatial structure function model, Eq. (4.25). Hanssen (1998) applied frozen-flow to correlate timeseries of ZWD differences from four GPS receivers with one-dimensional slices through the 2D InSAR atmospheric phase. These cuts were taken along the mean horizontal wind direction and stretched by mean wind speed as measured co-locally with the GPS receivers by radiosondes and surface-based sensors. He found correlation levels greater than 0.75 between the GPS ZWD timeseries and retrieved InSAR profiles. Here, we use the frozen-flow hypothesis to, first, infer flow speed and direction from the GPS ZWD timeseries acquired from the network and, second, to use ZWD measurements acquired before and after the SAR overpass times to increase the density of the GPS network in the statistical estimation of IWV difference maps.

In Section III below, we describe how, based on the frozen-flow hypothesis and the spatial autocorrelation functions of atmospheric delay, to include measurements of atmospheric path delay from GPS, recorded prior to and after the SAR acquisition times, in the spatial interpolation of atmosphere delay maps. Finally, in Section IV, we present spatially-interpolated maps of atmospheric path delay which we then compare to the observed phase screen in the radar interferogram.

6.2 The “frozen-flow” algorithm

6.2.1 Estimating mean wind from the GPS network data

The frozen-flow hypothesis applied to 3D wet refractivity may be stated as follows (Hanssen (1998), Williams et al. (1998), Ishimaru (1978) and Treuhaft and Lanyi (1987)):

$$N_{wet}(x, y, z, t) = N_{wet}(x - V_x t, y - V_y t, z, 0) \quad (6.1)$$

The frozen-flow hypothesis posits that a local slab of wet refractivity $N_{wet}(x, y, z)$ is transported, or *advected*, across an area by mean horizontal wind $\mathbf{V} = [V_x \ V_y]^T$, and that the spatial statistics of this refractivity field are unaffected by passage of the column across the area. We assume here that the mean wind \mathbf{V} is spatially constant but time-varying over the study area shown in Figure 3.6. Following Emardson and Webb (2002), we also assume that the sparse network of GPS receivers measures this wind-driven, advecting refractivity field over time, and further that wet delay possesses homogeneous statistics in space and wide-sense stationary statistics in time. Under these assumptions, the cross-correlation between GPS ZWD $l_{wet}^{GPS,z}(x, y, t)$ at two locations in space and consecutive time instances is,

$$\begin{aligned} C(\mathbf{R}, \Delta T) &= \left\langle l_{wet}^{GPS,z}(\boldsymbol{\rho} + \mathbf{R}, t + \Delta T) l_{wet}^{GPS,z}(\boldsymbol{\rho}, t) \right\rangle \\ &= \left\langle l_{wet}^{GPS,z}(\boldsymbol{\rho} + \mathbf{R} - \mathbf{V}\Delta T, t) l_{wet}^{GPS,z}(\boldsymbol{\rho}, t) \right\rangle \\ &= C(\mathbf{R} - \mathbf{V}\Delta T) \end{aligned} \quad (6.2)$$

$$\approx C(\mathbf{R}) - \nabla C|_{\mathbf{R}} \cdot (\mathbf{V}\Delta T) \quad (6.3)$$

where the autocorrelation function of ZWD measurements is given by

$$C(\mathbf{R}, t) = \left\langle l_{wet}^{GPS,z}(\boldsymbol{\rho} + \mathbf{R}, t) l_{wet}^{GPS,z}(\boldsymbol{\rho}, t) \right\rangle, \quad \boldsymbol{\rho} = [x \ y]^T, \quad \mathbf{R} = [R_x \ R_y]^T \quad (6.4)$$

with $t = \{t_{master}, t_{slave}\}$. We see from Eq. (6.2) that the 2D cross-correlation function of the ZWD field at consecutive time instants is related to the 2D autocorrelation function Eq. (6.4) by a simple translation dependent on the mean wind. If we assume that the translation

is small, in addition, the cross-correlation function can be linearized (Eq. 6.3). Our method of using timeseries measurements of ZWD from GPS for estimating the spatial atmospheric distortions from InSAR is to solve Eq. (6.3) for mean wind $\mathbf{V}(t)$ over time, and then relate timeseries of ZWD to locations at the SAR overpass times, using Equation (6.1). This provides a spatially denser network of control points for interpolation of ZWD difference map than is possible by considering only ZWD data recorded at the SAR overpass times.

We solve Eq. (6.3) for mean wind in a least-squares sense by fitting the autocorrelation function model shown in Figure 5.5(a) to empirical cross-correlations of GPS ZWD data at consecutive time instants. Analogous to the method we used in Chapter 4 to estimate structure functions from sparse GPS ZWD data (Eq. (4.30)), we compute cross-correlation functions of ZWD measurements at consecutive times t_i^n and t_i^{n-1} about the individual SAR overpass times t_i as follows

$$\hat{P}_l(\mathbf{R}_k, t_i^n) = \frac{1}{|S(\mathbf{R}_k)|} \sum_{(a,b) \in S(\mathbf{R}_k)} l_{wet}^{GPS,z}(\rho_a, t_i^n) l_{wet}^{GPS,z}(\rho_b, t_i^{n-1}) \quad t_i = \{t_1, t_2\} \quad (6.5)$$

where $S(\mathbf{R}_k) = \{(\rho_a, \rho_b) : \rho_a - \rho_b \approx \mathbf{R}_k\}$. We process GPS ZWD temporal observations from all 29 receivers in the area of study, within a period of $T_{window} \cdot \Delta T$ seconds (T_{window} samples) prior to and after the SAR overpass times of t_1 and t_2 . That is,

$$t_i^n \in \{t_i^{-T_{window}/2}, \dots, t_i^{-1}, t_i, t_i^1, \dots, t_i^{T_{window}/2}\} \quad (6.6)$$

In Eq. (6.5) above, $\hat{P}_l(\mathbf{R}_k, t_i)$ refers to estimates of the 2D cross-correlation function of GPS ZWD data recorded at receivers separated by about $\{\mathbf{R}_k\}$ and at consecutive times t_i^n and t_i^{n-1} . Following Eq. (6.3) and using the 2D spatial autocorrelation function model, we solve for a timeseries of mean wind estimates $\{\hat{\mathbf{V}}(t_i^n)\}$ in a least-squares sense as follows

$$\hat{\mathbf{V}}(t_i^n) = \min_{\mathbf{V}} \sum_k \left(\hat{P}_l(\mathbf{R}_k, t_i^n) - \left(\hat{\mathbf{C}}(\mathbf{R}_k) - \nabla \hat{\mathbf{C}}(\mathbf{R}_k) \cdot (\mathbf{V} \Delta T) \right) \right)^2 \quad t_i = \{t_1, t_2\} \quad (6.7)$$

In Figure 6.1, we present mean wind estimates over time obtained by applying Eq. (6.5)

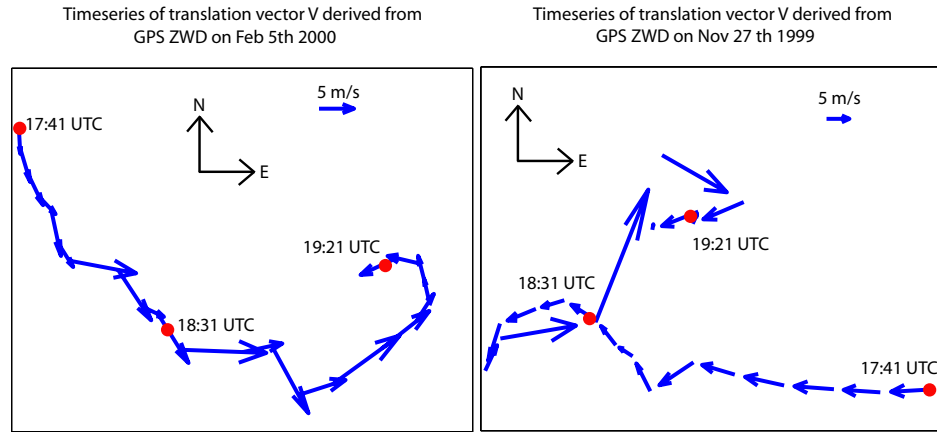


Figure 6.1 Left: Mean wind vectors $\hat{\mathbf{V}}(t_n^1)$ estimated from timeseries of GPS ZWD observations on February 5th 2000. Right: Mean wind vectors $\hat{\mathbf{V}}(t_n^2)$ estimated from timeseries of GPS ZWD observations on November 27th 1999. In the figure above, least-squares estimation of mean wind parameters $\mathbf{V}(t)$ was applied to GPS ZWD observations acquired 50 minutes prior to and 50 minutes after the radar acquisition times, 18:31 UTC, on both dates

and Eq. (6.7) to the GPS ZWD timeseries recorded 50 minutes ($T_{window} \cdot \Delta T = 3000$ seconds) prior to and after the SAR overpass times on February 5th 2000 and November 27th 1999. We interpret these vectors as a vertical average of wind in the lower atmosphere since the GPS ZWD measurements from which the wind estimates are inferred are themselves proportional to total amount of water vapor contained in a vertical column of air. In Chapter 7, we will show analytically that this interpretation is plausible. The vectors shown in Figure 6.1 are instantaneous estimates of wind direction and magnitude affecting the entire ZWD field which is sampled over time by the sparse and irregularly-spaced network of GPS receivers.

6.2.2 Generating dense networks of ZWD control points

By the frozen-flow hypothesis, the timeseries of mean wind estimates shown in Figure 6.1 is then used to translate temporal observations of GPS ZWD spatially across the range-azimuth grid of the radar interferogram, forming a denser network of GPS ZWD control

points for subsequent interpolation (see Figure 6.2 below). A ZWD measurement made at time t_i^n from a GPS receiver located (x_a, y_a) will be advected to a new position (x, y) at the time of SAR overpass $t_i = \{t_1, t_2\}$ determined by the vector summation of all mean wind estimates between time t_i^n and t_i ,

$$\begin{bmatrix} x \\ y \end{bmatrix} = \begin{bmatrix} x_a \\ y_a \end{bmatrix} + \hat{\mathbf{V}}(t_i^n)\Delta T + \hat{\mathbf{V}}(t_i^{n-1})\Delta T + \dots + \hat{\mathbf{V}}(t_i)\Delta T \quad (6.8)$$

To illustrate, in Figure 6.2 we plot the resulting denser networks of GPS ZWD control

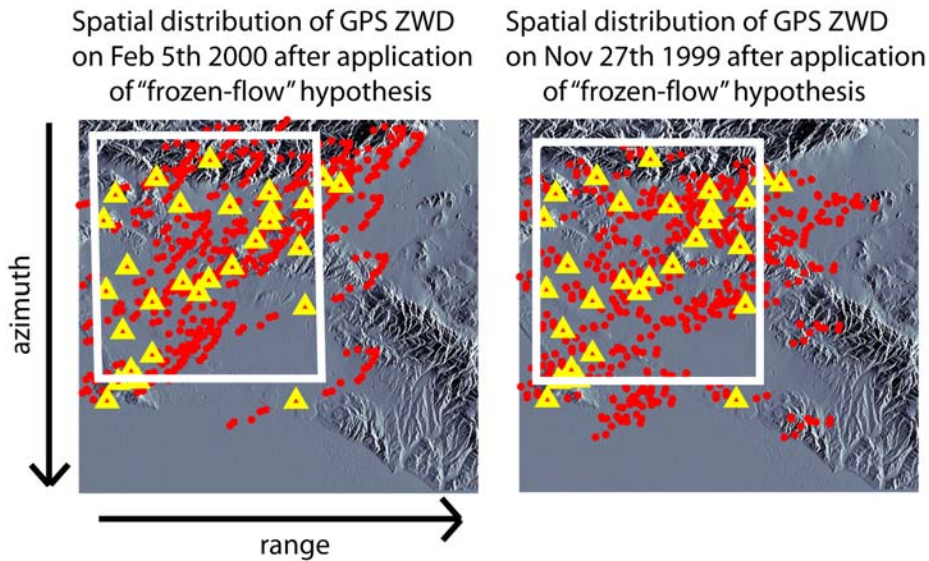


Figure 6.2 Left: Denser network of GPS control points inferred from observations collected 65 minutes about t_1 on February 5th 2000, using corresponding mean wind timeseries estimates. Right: Denser network of GPS ZWD control points inferred from GPS observations recorded 30 minutes about t_2 on November 27th 1999, by applying mean wind timeseries estimates in according to Eq. (6.8). Yellow triangles indicate locations of the 29 continuous GPS stations in the SCIGN network. Red dots are locations of new control points obtained after application of the “frozen-flow” hypothesis. The box denotes the region of study. Points spatially-translated out of the region of interest (Figure 3.6) are discarded.

points after applying the timeseries mean wind estimates to temporal measurements of delay recorded 30 minutes about the slave acquisition time and 65 minutes about the master

acquisition time. The reason we used a time window that is asymmetric with respect to the SAR overpass times will be explained in the following section. The yellow triangles are the locations of actual GPS receivers, while the red dots are the inferred GPS estimates obtained by advecting the measurements at the triangles to the SAR overpass times. With more control points available, we then use interpolation to generate an IWV difference map that better reduces the turbulently-mixed atmospheric phase distortions observed in the interferogram, Figure 5.6(a). We note that other interpolation techniques can be used to generate the IWV difference map. Here, we choose kriging because we model the turbulently-varying wet delay field as a stochastic process with a known autocorrelation function. We note that we interpolate using only those points that fall within the study area, including GPS ZWD samples originating from outside the region of interest. While GPS ZWD observations translated outside the region of study may contain useful information for the interpolation procedure, we find that these samples are less correlated with the unwrapped phase samples within the area of study. Accordingly, we exclude those external points from the interpolation procedure.

6.3 Interpolating a IWV difference map

In this section, we compare the atmospheric phase corrected for topography-dependent spatial variation (Figure 5.6(a)) with an IWV difference map generated from the denser GPS ZWD control point network (red dots in Figure 6.2) inferred by our frozen-flow method. We find that the larger set of GPS ZWD control points produces interpolated maps with lower interpolation error RMS than the IWV difference map generated by interpolating ZWD data acquired only at the SAR overpass times. Figure 6.3(a) shows the turbulently-mixed atmospheric phase, displayed previously in Chapter 5. Figure 6.3(b) shows the result obtained in Chapter 5 by interpolating the 29 GPS ZWD measurements acquired only at the SAR overpass times. In Figure 6.3(c), we show the IWV difference map generated by interpolation of the denser network of GPS ZWD observations. Figures 6.3(d) and (e) show interpolation error magnitudes obtained by subtracting the interpolated maps from Figure 6.3(a). As can be seen, the IWV difference map obtained from the denser network of ZWD observations produced by our method better compensates the small-scale phase artifacts

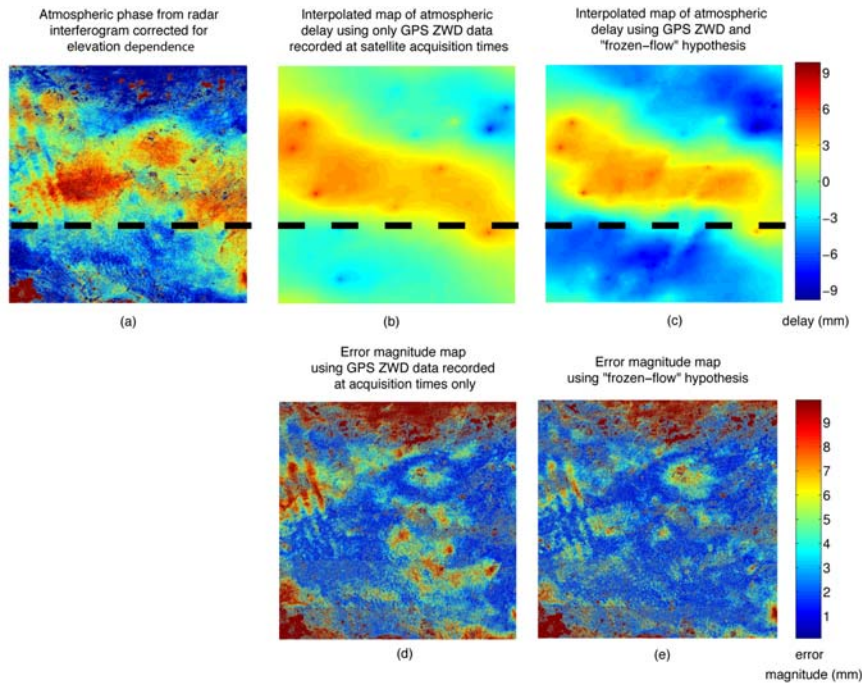


Figure 6.3 (a): Turbulently-mixed atmospheric phase in the area of study as shown previously in Figure 5.6(a) (b): Kriging-interpolated IWV difference map from network of GPS ZWD measurements recorded only at the SAR overpass times. (c): Kriging-interpolated IWV difference map from denser network of GPS ZWD measurements (Figure 6.2) obtained from application of “frozen-flow” hypothesis to timeseries recorded at 29 SCIGN GPS stations. (d): Error magnitude from correcting observed atmospheric phase (a) with the IWV difference map in (b). (e): Error magnitude from correcting observed atmospheric phase (a) with the IWV difference map (c). The dotted line across panels (a), (b) and (c) denotes location of a profile of turbulently-mixed atmospheric phase that is compared with corresponding profiles from the kriging IWV difference maps in Figure 6.4

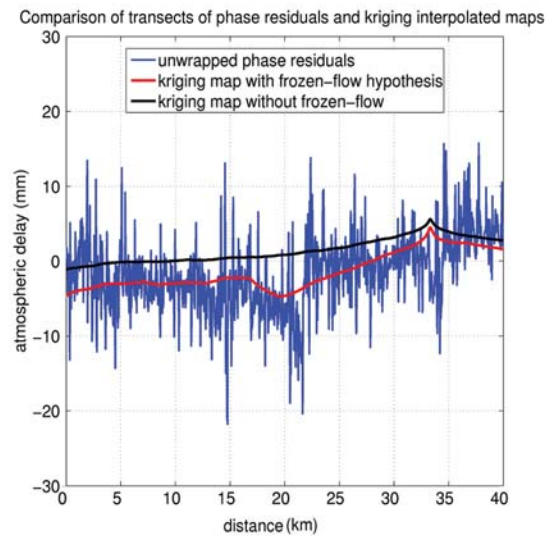


Figure 6.4 Cuts in the range direction through the turbulently-mixed atmospheric phase and interpolated map. The phase residuals are shown in blue. The red curve represents a transect through the krigged map interpolated from a denser network of GPS ZWD observations. The black curve is the corresponding transect through the krigged map obtained without consideration of the “frozen-flow” hypothesis, and follows the data less well than the curve derived from the denser network.

compared to the map generated from GPS ZWD measurements recorded only at the SAR overpass times.

Figure 6.4 displays a transect through the turbulently-mixed atmospheric phase and the kriging maps generated with and without application of the “frozen-flow” hypothesis, along the dotted line in Figure 6.3.

We quantify the extent to which GPS ZWD measurements match observed atmospheric phase distortions by computing the RMS of residual fluctuations, averaged over the 60 km by 60 km area of study shown in Figure 3.6, before and after interpolated maps of GPS ZWD are used to correct the InSAR phase. Our choice of RMS residual fluctuation as a quantitative measure of agreement between the observed turbulently-mixed atmospheric phase and the interpolated IWV difference maps from GPS assumes (1) that the observed phase variations are due solely to turbulent atmospheric fluctuations and (2) that these fluctuations are reproducible by spatially interpolating samples of ZWD from GPS. In regard to

Table 6.1 RMS atmospheric phase fluctuations before and after GPS-derived corrections

	RMS error (mm)	
atmospheric phase	16.1	
	Entire spectrum	Low-pass filtered
corrected for topography-dependent variation	8.6	4.7
correction using GPS ZWD at SAR overpass times only	8.1	3.9
correction using “frozen-flow” method	7.5	2.7

(1), we know that crustal deformation due to groundwater level changes and oil field activity introduces significant deformation phase in radar interferograms acquired over the Los Angeles Basin area (Watson et al. (2002)). While such deformation signals may be present in the SAR data used here, the use of RMS interpolation error as a measure of similarity could incorrectly compare these non-atmospheric phase signatures with the interpolated maps generated from applying the frozen-flow hypothesis to GPS ZWD observations. That is, the RMS of the residuals may contain a component due to uncorrected crustal deformation phase.

We also note that globally-averaged RMS residual computed after correcting the observed phase with interpolated IWV difference maps will depend on spatial frequency (see discussion below) and does not reflect the variable density of GPS ZWD observations over the interferogram. These caveats notwithstanding, we use RMS residual phase fluctuation as an indicator of similarity between the observed atmospheric phase artifacts and the inferred delay maps.

Table 6.1 lists the RMS error after the interpolated IWV difference maps shown in Figures 6.3(b) and (c) are subtracted from the turbulently-mixed atmospheric phase. We note that the RMS residual of the turbulently-mixed InSAR atmospheric phase is 8.6 mm, if no correction is applied.

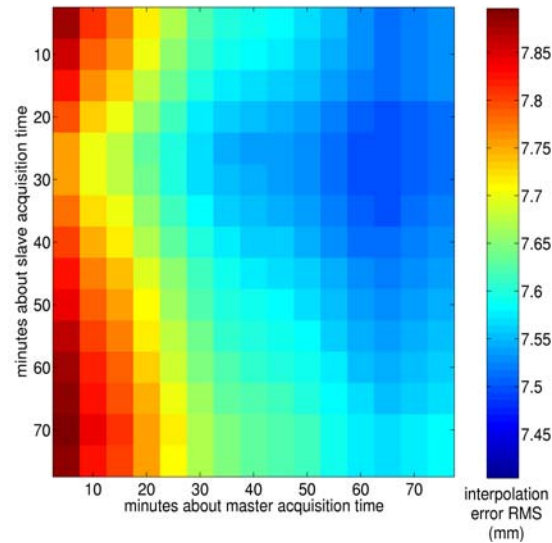


Figure 6.5 Error surface generated by applying the frozen-flow hypothesis to different durations of ZWD measurements about the SAR overpass times (label “master” and “slave”). The minimum RMS error of 7.5 mm is seen to occur when GPS ZWD data in a time window 65 minutes long around the master acquisition time t_1 and a window of length 30 minutes around the slave acquisition time t_2 is converted to equivalent spatial samples by our method.

Increasing the duration of time about the satellite acquisition times during which the frozen-flow hypothesis is applied results in denser networks of ZWD control points, as more samples of GPS ZWD measurements are translated spatially across the grid of the radar interferogram. However, the longer the time window about the acquisition times the greater the error in the positioning of ZWD data on the interferogram grid. This positioning error degrades the quality of interpolated maps of atmospheric delay. The result in Table 6.1 was obtained by examining different time window lengths about the master and slave acquisition times during which the frozen-flow hypothesis was applied. Figure 6.5 shows the error surface obtained after correcting the turbulently-mixed atmospheric phase for atmospheric delay using interpolated from ZWD networks with varying density of control points. There is undoubtedly a different optimal time window for any overpass time, and determining this in the general case remains for future work. We find that applying our method to the November 27th 1999 GPS ZWD timeseries 30 minutes about the radar observation time

and 65 minutes about the satellite acquisition time on the February 5th 2000 GPS ZWD timeseries produces the lowest residual delay map. This map is displayed in Figure 6.3(b) and the associated magnitude of the residuals is shown in Figure 6.3(d).

GPS ZWD differences recorded only at the SAR overpass times reduces fluctuations of atmospheric phase in the radar interferogram from 8.6 mm to 8.1 mm rms, if the entire spatial phase spectrum is preserved (see Chapter 5). With prior smoothing, the corresponding reduction is from 4.7 to 3.9 mm. From Table 6.1, incorporation of timeseries observations of ZWD from GPS, using the frozen-flow hypothesis, reduces the magnitude of phase distortions to 7.5 mm rms for the full spectrum of the signal, and to 2.7 mm rms for the averaged signal.

The results in Table 6.1 show quite clearly that prior smoothing of the unwrapped phase residuals results in greater reduction in RMS of atmospheric phase after correction by the interpolated maps, as we had noted in Chapter 5. Physically, this follows because there is an upper bound on the spatial frequency of turbulently-mixed atmospheric phase fluctuations that can be reproduced in the IWV difference maps obtained from GPS measurements. This upper bound corresponds to the width of the GPS averaging cone. In addition, the sample rate of GPS ZWD timeseries also dictates a maximum spatial frequency that is reproducible by interpolation. For example, assuming a nominal wind speed of 8 ms^{-1} , the maximum frequency of atmospheric delay spatial signatures that can be recovered by interpolation is $\frac{1}{8 \text{ ms}^{-1} \times 300 \text{ s}} = 1/2.4 \text{ km}^{-1}$. Finally, the finest-scale fluctuations observed in the interferogram are due to temporal decorrelation and system noise which cannot be accounted for by GPS ZWD measurements.

Application of our proposed method to ZWD data from a larger collection of GPS receivers over the same study area will likely provide better insight into the validity of frozen-flow hypothesis as applied to GPS and InSAR data in addition to providing better statistics. In Chapter 8, we will present results obtained from applying the frozen-flow algorithm described in this chapter to ZWD measurements from a larger collection of GPS sites. With the network used here, our results demonstrate that incorporation of additional ZWD control points from GPS timeseries data yields interpolated maps that correct observed phase distortions to lower RMS error than maps interpolated from the few measurements recorded only at the radar observation times.

6.4 Discussion

Analysis of ZWD timeseries from a sparse network of GPS receivers permits a frozen-flow algorithm as presented in this chapter, which proceeds in three steps:

- (1) wind estimation,
- (2) translation of temporal ZWD measurements to equivalent spatial samples to form a dense network, i.e. Eq. (6.8),
- (3) statistical (kriging) interpolation

The utility of IWV difference maps produced by our algorithm for reducing turbulently-mixed InSAR atmospheric phase distortions depends on several factors:

- (i) number of GPS ZWD control points
- (ii) measurement noise in the GPS ZWD control points
- (iii) accuracy of GPS ZWD at representing InSAR atmospheric phase
- (iv) accuracy of the interpolator

The number of control points is set by the application of Step 2 to timeseries of ZWD, given estimates of wind from Step 1. Thus, our method surmounts the limitations imposed by the inherent sparseness of GPS networks in estimating the turbulently-mixed atmospheric phase variations by using ZWD measurements acquired before and after the SAR overpass times.

The ZWD measurement noise level depends on the noise level of the GPS carrier phase observations. For this study, the measurement noise in the ZWD estimates was about 4 mm, as determined by GIPSY processing of the raw GPS observables.

Even assuming no measurement noise in GPS observables, we note that GPS and InSAR infer wet delay in different ways. This may affect the the accuracy of dense ZWD networks, as generated by our method, for representing point measurements of observed InSAR atmospheric phase. GPS and InSAR are similarly sensitive to water vapor in the neutral atmosphere. However, InSAR directly measures wet delay as a component of total

pixel interferometric phase. In contrast, ZWD is estimated by combining phase observations of the GPS carrier signal incident on a receiver at many different angles. Thus, GPS ZWD estimates depend on the choice of parameters used in the estimation procedure, and this affects its consistency with InSAR atmospheric phase observations.

Specifically, as noted in chapter 3, GPS ZWD are weighted averages of a (conical) volume of neutral atmosphere overlying the receiver while InSAR measures wet delay only along the radar LOS. The minimum elevation angle γ_{GPS} is a GIPSY parameter and determines the size of the conical volume of neutral atmosphere that is averaged to yield a ZWD estimate, as indicated by Figure 3.1. Decreasing this minimum elevation angle causes a larger volume of neutral atmosphere to be averaged in the estimation of ZWD. This may result in a more accurate measurement of mean ZWD for that volume. However, for data acquired from a network of receivers, such as the SCIGN network used in this work, reducing the minimum elevation angle will underestimate the spatial variation of ZWD measured across the network relative to the observed variation of turbulently-mixed InSAR atmospheric phase. This in turn leads to additional disagreement between ZWD networks generated by our algorithm and the observed InSAR atmospheric phase, limiting the effectiveness of the final GPS-derived atmospheric correction. In general, the error level between GPS and InSAR observations of wet delay depends on the length scale of water vapor variations in the neutral atmosphere. If the neutral atmosphere varies slowly horizontally, then GPS and InSAR measurements of the associated delay should be approximately equal. However, since we have assumed turbulent-mixing of water vapor, then wet refractivity varies significantly at short-scales and, thus, we expect GPS cone-averaged ZWD to underestimate the variations of InSAR LOS wet delay measurements.

The drift rate parameter α in Eq. (3.5), which is another GIPSY processing parameter, can also impact the similarity between ZWDs estimated at the SAR overpass times and InSAR atmospheric phase measurements. This is because α controls the amount of time-variation in the estimated ZWD timeseries.

Finally, GPS ZWD data may be biased due to unmodeled hydrostatic delays. We recall from chapter 3 that in GIPSY-estimation of ZWD, stable hydrostatic delay is assigned a nominal value while ZWD is estimated from the raw carrier phase as time-varying (stochastic) fluctuations about this nominal value. Nominal hydrostatic delay is another GIPSY

parameter, and so the magnitude of hydrostatic bias in the ZWD timeseries depends on the accuracy of this assumed value. Hydrostatic biases in GPS and InSAR are topography-dependent since surface pressure decreases with increasing altitude. As we have corrected the GPS and InSAR delay measurements for altitude-dependent trends, we expect residual hydrostatic biases to be small. Nevertheless, the hydrostatic bias in the GPS and InSAR observations of wet delay may be present and its magnitude is approximately equal to the difference between our inferred model for vertical stratification of neutral atmosphere, as shown in Figure 5.1, and the actual vertical distribution of surface pressure from which hydrostatic delays can be computed using the Saastamoinen model, Eq. (4.10).

Additional error between GPS ZWD networks and InSAR atmospheric phase may be introduced in the formation of networks by Steps 1 and 2 of our method. This error is reflected in the agreement between empirical spatial autocorrelation functions computed from the dense network and the assumed model.

Errors in estimates of wind obtained in Step 1 can cause the empirical autocorrelation function of the dense ZWD network to deviate from the assumed model. The optimal set of wind vector estimates in a given time window T_{window} around the SAR overpass times minimizes the difference between the empirical spatial autocorrelation computed from the resulting dense ZWD network and the assumed model. The least-squares wind estimation procedure described above minimizes this disparity at consecutive time steps only. Figure 6.6 shows the empirical spatial autocorrelation function computed from the sparse SCIGN ZWD observations at the SAR overpass times (red) and the autocorrelation (black) estimated from the resulting dense network shown in Figure 6.2. In blue, we plot the rotationally-averaged profile of the assumed 2D spatial autocorrelation model, Figure 5.5. The RMS errors between the empirical spatial autocorrelations and the reference model are 11.7 mm^2 and 7.4 mm^2 for the dense and sparse SCIGN networks respectively. Hence, the spatial autocorrelation of the dense ZWD control points is less similar to the assumed model as than the autocorrelation of GPS data acquired only at the SAR overpass times. Thus, a possible improvement to our implementation is to couple Steps 1 and 2 by incorporating a constraint so that the error between the assumed autocorrelation model and empirical spatial autocorrelations computed from an expanding network is minimized as

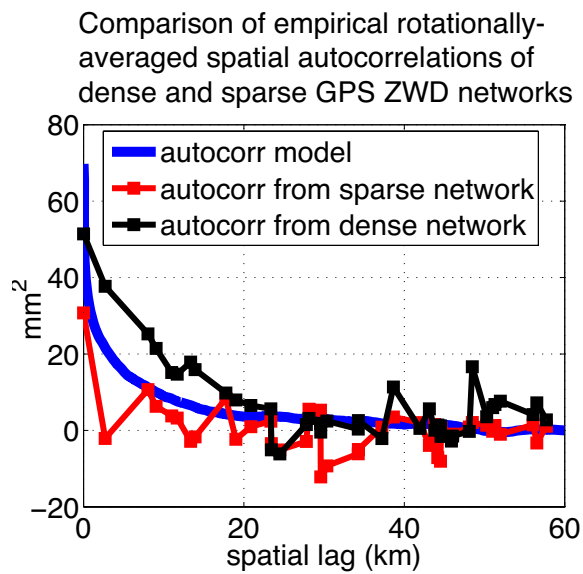


Figure 6.6 (Red): Empirical spatial autocorrelation computed from GPS ZWD observations at the SAR overpass times obtained from the relatively sparse SCIGN network. (Black): empirical spatial autocorrelation function inferred from the dense network in Figure 6.2. Profile of the spatial autocorrelation model assumed is shown in blue

the time window T_{window} is increased. Also, wind estimates from independent meteorological observations could be used instead of the vector estimates obtained by correlation analysis.

The systematic error between the dense network control points and InSAR atmospheric phase may also depend on the accuracy of the frozen-flow hypothesis in Step 2, as represented by Eq. (6.8). We use Eq. (6.8) to generate the dense network of control points from GPS ZWD timeseries and estimates of wind. Our approach in Step 2 is essentially an idealized Lagrangian transport model (Wilson and Sawford (1996)). In Lagrangian transport problems, individual air parcels are tracked along trajectories $\mathbf{x}(t)$ determined by wind

$$\mathbf{x}(t) = \rho_a + \int_0^t \mathbf{V}(\tau) d\tau \quad (6.9)$$

where ρ_a here refers to the location of a GPS receiver and $t = 0$ denotes a SAR overpass time. By applying a Lagrangian approach, we essentially track columns of water vapor, proportional to the measured ZWD from GPS, along trajectories determined by mean wind estimates from Step 1. Our approach here is idealized because the frozen-flow hypothesis as applied in Step 2 physically states that the total amount of water vapor contained in a column of air stays constant as the column is advected over the study area by mean wind. However, we note that the frozen-flow hypothesis is best applied to characterize the spatio-temporal statistics of wet refractivity. The hypothesis may unrealistically describe actual transport of total column water vapor over time as this hypothesis does not include the effects of turbulent diffusion of water vapor into and out of the advecting columns. A further idealization is the assumption of spatially-constant wind. Thus, a possible improvement for this step in our algorithm is to incorporate better transport models, such as stochastic Lagrangian trajectory models (Wilson and Sawford (1996)), that include effects of water vapor diffusion and spatially-variable wind to generate the dense ZWD network. We note that the objective to be met in applying more sophisticated transport models is to minimize the error between empirical spatial autocorrelations inferred from the resulting dense control point networks and the assumed autocorrelation model. The application of better Lagrangian models to the formation of dense ZWD networks for interpolating GPS-derived IWV maps remains for future work. In Chapter 7, we will present a generalized algorithm,

based on an Eulerian transport model, that includes turbulent diffusion and advection by spatially-variable wind to describe the evolution of water vapor over the study area around the SAR overpass times.

The autocorrelation model we assume may be biased by non-atmospheric phase signatures in the radar interferogram, such as due to ground deformation. Thus, the spatial autocorrelation in Figure 5.5(a) may not accurately represent spatial variations of wet delay fluctuations and this may also explain some of the observed differences between autocorrelations inferred from GPS and InSAR data.

The final factor influencing the accuracy of IWV difference maps inferred by our method is the kriging interpolator itself. From the results shown in Tables 6.1, we observed that prior smoothing of the frozen-flow ZWD difference map yielded a greater reduction in atmospheric phase RMS relative to the map interpolated from GPS ZWD data acquired only the SAR overpass times compared to when no smoothing was applied. This suggests that the interpolator introduces spurious high-frequency artifacts in the resulting maps even when additional control points are available, as noted by Hanssen (1998) and Li et al. (2006).

We demonstrate, by means of numerical simulation, the dependence of kriging interpolation performance with respect to:

- (1) number of control points
- (2) measurement noise level
- (3) similarity between the autocorrelation of the control points and the target map
- (4) assumed autocorrelation model and
- (5) 2D sampling pattern.

We compute a simulation, quantifying krig-interpolation RMS error as a function of the five factors listed above. The target map that we approximate by interpolation is 300×300 pixels in size and is shown in Figure 6.7(a). This map was generated as a sum of two Von

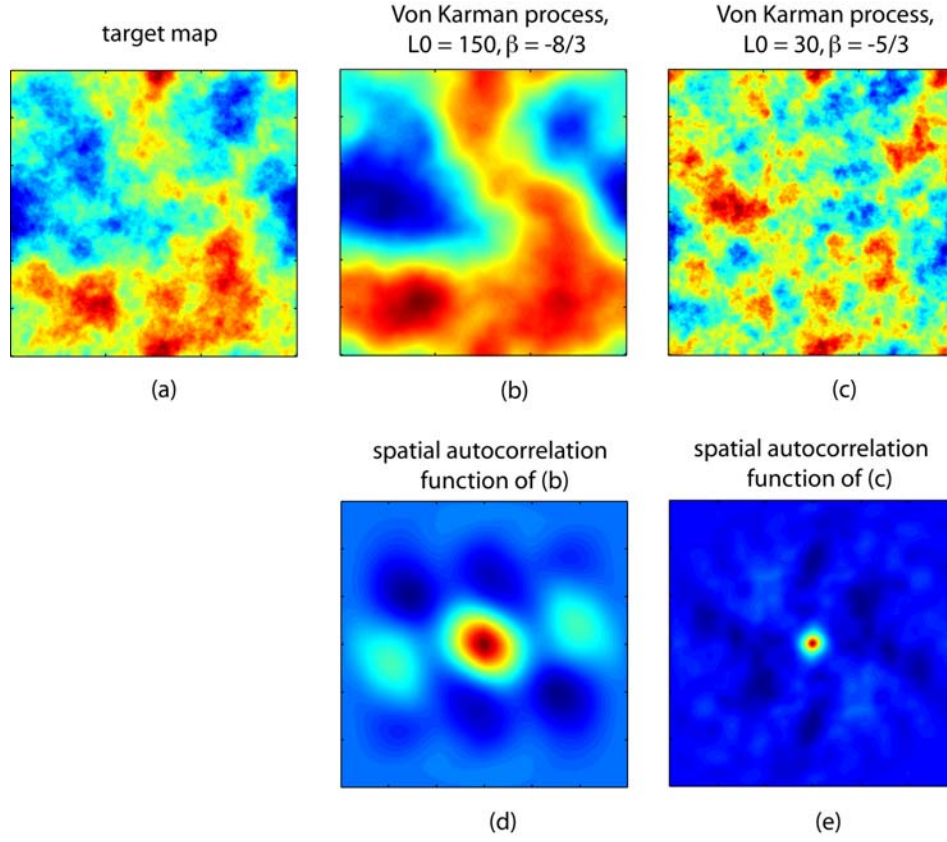


Figure 6.7 (a): target map used in simulation is the sum of two Von Karman random process realizations. (b): realization of Von Karman random process with $L_0 = 150, \beta = -8/3$. (c): realization of Von Karman process with $L_0 = 30, \beta = -5/3$. (d): spatial autocorrelation function of (b). (e): spatial autocorrelation function of (c)

Karman random process realizations with PSD given by (Ishimaru (1978))

$$S(k_x, k_y) \propto \frac{1}{(\sqrt{(1/L_0)^2 + k_x^2 + k_y^2})^\beta} \quad (6.10)$$

We used $L_0 = 150, \beta = -8/3$ to generate the first map, shown in Figure 6.7(b), while the second map in Figure 6.7(c) was formed with parameters $L_0 = 30, \beta = -5/3$. The spatial autocorrelation functions of these two realizations are shown in Figures 6.7(d) and (e). In this simulation, we extract control points from the map in Figure 6.7(a). These

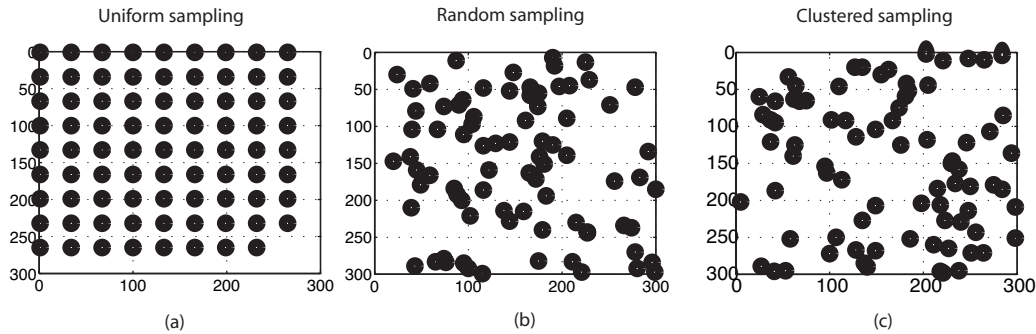


Figure 6.8 (a): uniform sampling pattern. (b): random sampling pattern. (c): clustered sampling pattern.

control points were corrupted with Gaussian noise with standard deviation proportional to the RMS fluctuations of the map itself. The number of control points we used in this experiment was below 0.05% of the total number of grid cells. This percentage is on the order of the proportion of total number of control points used in the frozen-flow algorithm to generate the IWV difference map shown in Figure 6.3(c). We extracted these control points according to three sampling patterns: (1) uniform (Figure 6.8(a)), (2) random (Figure 6.8(b)) and (3) clustered (Figure 6.8(c)). We generated the clustered sampling pattern as a realization of a Poisson point process (Zimmerman et al. (1999)). We also used two types of control points: (1) control points obtained directly from Figure 6.7(a) and (2) control points obtained from the same map smoothed with a 40×40 boxcar filter to simulate the cone-averaging effect in GPS ZWD estimation.

Figure 6.9(a) shows the RMS error from krig interpolation of networks of control points. Here, we use the sum of spatial autocorrelation functions, Figures 6.7(d) and (e), as the autocorrelation model for kriging. The three colors denote the ratio of standard deviation of Gaussian noise corrupting the control points to RMS residual of the target map (0.27), i.e. $1/\text{SNR}$. The plots with circles show the results we obtained by using control points extracted from the target map, Figure 6.7(a). The plots with diamonds show the corresponding results when smoothed control points were used. We plot RMS error as a function of number of control points to simulate interpolating denser networks of ZWD

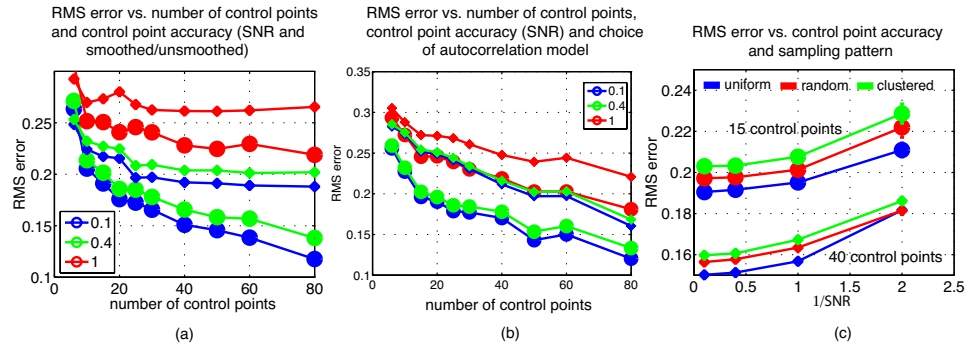


Figure 6.9 (a): RMS kriging interpolation error curves of the target map, Figure 6.7(a) as a function of number of control points. The three colors denote $1/\text{SNR}$ levels of Gaussian noise added to the control points. The diamonds indicate results obtained using smoothed control points, while circles show RMS error curves using unsmoothed control points. (b): RMS kriging interpolation error curves as a function of number of control points. Curves with circles show error curves using the correct autocorrelation model with kriging, the sum of Figures 6.7(d) and (e). Curves with diamonds show RMS error using autocorrelation model Figure 6.7(d) only. (c): RMS error as a function of $1/\text{SNR}$ for the three sampling patterns shown in Figure 6.8.

point measurements generated by the frozen-flow algorithm. We ran a total of 600 simulations to produce average RMS interpolation error curves shown in this figure. The results in Figure 6.9(a) indicate that:

- (1) interpolating smoothed control points significantly degrades the improvement in RMS interpolation error relative to the improvement obtained by using unsmoothed control points. The degradation is particularly severe when the noise level is low and a large number of control points are used.
- (2) the improvement in RMS error with increasing number of control points is marginal when the noise level is high. Assuming unsmoothed control points, only an 11% improvement in RMS residual, relative to when zero control points are used, is realized using 80 control points at a $\text{SNR} = 1$.

The results in Figure 6.9(b) illustrate the impact on RMS interpolation error improvement when the spatial autocorrelation of control points used in the interpolation differs from the assumed model. In Figure 6.9(b), we examine the effect of an error in the assumed autocorrelation model used in the krig-interpolation procedure. Error curves with

circles in Figure 6.9(b) indicate results obtained by using the correct autocorrelation model, while the corresponding error curves with diamonds were obtained by using the autocorrelation model shown in Figure 6.7(d) only. Here we use unsmoothed control points in the interpolation. The results shown here suggest that krig-interpolation error performance is sensitive to the choice of assumed autocorrelation model.

This result has implications for the general applicability of the frozen-flow algorithm described in this chapter. In this study, we have assumed that the autocorrelation model shown in Figure 5.5(a) describes the spatial fluctuations of wet delay difference in the interferogram. However, as this model was measured directly from the InSAR atmospheric phase, Figure 5.5 may be biased by other unmodeled phase signatures, due to ground deformation for example, and thus may not accurately represent turbulent variations of wet delay. For improved reduction in the turbulently-mixed atmospheric phase component of observed interferometric phase, it is thus necessary to use an accurate spatial autocorrelation model as the results in Figure 6.9(b) indicate.

Figure 6.9(c) shows RMS interpolation error at different noise levels and different spatial configurations of control points in the network. We show results from interpolating 15 and 40 control points. The curves in blue, red and green denote uniform, random and clustered sampling patterns respectively. We can thus expect such sampling patterns to arise when using the “frozen-flow” algorithm to generate a dense network of control points. Figure 6.9(c) indicates that there is small dependence on interpolation performance due to the configuration of the control point network.

6.5 Conclusions

We present a method for generating a spatially dense set of ZWD measurements from time-series of GPS data. We find that interpolating this denser network of GPS data produced maps that more closely match local atmospheric phase fluctuations in the SAR interferogram than those derived by interpolating GPS ZWD measurements acquired only at the SAR overpass times.

The turbulently-mixed atmospheric phase component from the radar interferogram in Figure 3.6 showed spatial fluctuations of 8.6 mm RMS. We correct the phase distortions

with maps proportional to total column water vapor interpolated from networks of GPS ZWD measurements. Interpolating the few GPS ZWD measurements recorded only at the SAR overpass times reduced overall fluctuation magnitude to 8.1 mm rms. In contrast, interpolating the denser network of atmospheric delay measurements from GPS, obtained by applying the “frozen-flow” hypothesis to timeseries of GPS data, reduces the magnitude of phase fluctuations to 7.5 mm rms. When the data are averaged to remove short-scale decorrelation effects, the corresponding error values are 4.7 mm, 3.9 mm, and 2.7 mm rms, respectively.

The degree of spatial detail in the interpolated delay maps depends on the number of control points available for interpolation. When we assume that the GPS ZWD data are spatio-temporal measurements of a static wet refractivity field flowing across the region of study under the action of time-varying mean wind, temporal observations of path delay from GPS can be translated to additional spatial measurements by estimating the time-varying mean wind from the suite of ZWD timeseries. This increases the number of control points available for subsequent interpolation of delay maps. Comparison of wind estimates with surface measurements and numerical weather prediction models remains for future work.

We find that the performance of the frozen-flow algorithm is limited by the systematic differences between InSAR and GPS measurements of wet delay. These differences cause the dissimilarity between empirical autocorrelations computed from the ZWD control point network and the assumed model obtained directly from the InSAR phase. Through a numerical simulation, we showed that improvement in RMS error reduction achieved by using additional control points is limited by accuracy of the control points at representing actual point measurements of the target surface as well as by error in the assumed autocorrelation model. Estimation of time-varying mean wind and formation of the dense network of control points from GPS ZWD timeseries and the frozen-flow transport model also impacts the agreement between the autocorrelations of these data. Characterization of the spatial autocorrelation function of wet delay remains for future work. We also find that krig-interpolation introduces spurious high-frequency artifacts in the interpolated result. In the following chapter, we present a deterministic method for estimating IWV maps from GPS ZWD timeseries. This method does not rely on interpolation nor require an a priori

spatial autocorrelation model to describe variations of water-vapor-induced delay. These variations are inferred directly from advection and turbulent diffusion of wet delay.

Chapter 7

Advection-diffusion modeling of wet delay

In some cases, we may not have sufficient knowledge of the autocorrelation function of the turbulently-mixed component of atmospheric water vapor, precluding the approach of the previous chapter. Here, we examine a physically-based method for compensating InSAR images for phase distortion, that does not rely on such knowledge or assumptions.

The frozen-flow algorithm, described in Chapter 6 relates IWV difference maps from GPS ZWD timeseries to atmospheric phase distortions in a radar interferogram. We previously modeled turbulently-mixed InSAR atmospheric phase as a stationary and homogeneous stochastic process with a known spatial autocorrelation function, and our approach was to interpolate GPS point measurements of this random process statistically. We increased the effective sampling density of GPS measurements using the frozen-flow hypothesis, constructed a space-time ZWD autocorrelation model, and developed an idealized Lagrangian transport model that incorporates GPS data acquired before and after the SAR overpass times into the interpolation procedure.

We found that the accuracy of the atmospheric correction depends on the number of control points available. We also found that the performance of the frozen-flow algorithm depends on (1) the agreement between the empirical spatial autocorrelation computed from the inferred dense network of ZWD control points and the assumed model and (2) the krig interpolator used to generate IWV difference maps at InSAR resolution. The error

between the empirical and model autocorrelation functions depends on the diffuse GPS sampling of neutral atmospheric water vapor due to the cone-averaging effect (see Chapter 3), errors in the estimates of wind, and the simplicity of the frozen-flow transport model we used to generate the dense network. Our transport model neglects physical effects such as spatially-variable wind fields and turbulent diffusion of water vapor. We also note that the interpolation algorithm introduces spurious high-frequency artifacts in the interpolated result, lessening the expected improvement resulting from additional control points.

In this chapter, we develop another approach to estimate the turbulently-mixed InSAR atmospheric phase distortions from GPS ZWD timeseries. Instead of interpolating individual samples of ZWD - which are each proportional to total column water vapor - as parcels of troposphere transported in a “frozen” sense by a mean, spatially-constant wind, we now estimate ZWD fields directly from measurements acquired at the fixed GPS receiver locations and recorded over an interval near the SAR overpass times using a physically-based model.

This second algorithm uses a two-dimensional Eulerian transport model (Emeis (1997)) for total column water vapor, which describes the spatial and temporal variations of ZWD fields deterministically. Whereas the Lagrangian approach in Chapter 6 tracks the trajectory and composition of individual columns of water vapor (assumed time-invariant in the frozen-flow transport model), the Eulerian model here describes the spatial and temporal fluctuations of entire fields of IWV that result from advection and diffusion of water vapor in the atmosphere by mean laminar flow and turbulent flow, respectively.

Our Eulerian transport model for ZWD is a conservation equation for mean IWV and is derived from the conservation of mass and humidity in the atmosphere. As with mass, the amount of moisture contained in a particular volume element of air is approximately conserved as it is displaced by atmospheric flow (Ishimaru (1978)). The conservation equation equates time rate of change of the average level of columnar water vapor with net transport of moisture into that column. This transport is the sum of (1) advective transport due to mean laminar atmospheric flow and (2) diffusive transport resulting from the mixing of humidity by turbulent flow perturbations. We do not explicitly consider turbulent fluctuations of flow in this work because such perturbations are typically modeled statistically and are beyond the scope of this work. Also, the spatially-sparse GPS ZWD measurements cannot

resolve fine-scale turbulent fluctuations. Instead, we consider only the effect of turbulent flow fluctuations on mean level of IWV in a column of air by modeling turbulent mixing of water vapor with a diffusive transport term in the IWV conservation equation.

Thus, our transport model is parametrized by spatially-variable two-dimensional mean laminar flow, which is related to vertically-integrated wind in the atmosphere, and a diffusion coefficient which incorporates the effects of turbulent mixing of moisture. We assume that the ZWD timeseries measured at the SCIGN receiver locations are point measurements of a ZWD field evolving according to the transport model. The turbulently-mixed atmospheric phase observed in the radar interferogram is the difference of two evolving fields evaluated at the SAR overpass times. The IWV difference map follows from least-squares fitting of the transport model to ZWD timeseries measured at the receiver locations. The spatial variation of turbulently-mixed atmospheric phase observed in the radar interferogram is obtained from GPS ZWD timeseries through considering 2D advection by mean flow and turbulent diffusion of water vapor, rather than a statistical characterization as we used in the a priori spatial autocorrelation function model.

Inverse problems involving two-dimensional transport models for passive tracers in geophysical flows are found in numerous fields, including oceanography, precipitation studies and meteorology. Corpetti et al. (2002) estimated 2D flow fields from a sequence of Meteosat IR images by regularized inversion of a transport model for air mass density. Jinno et al. (1993) used a 2D transport model for rainfall intensity to estimate velocity, diffusion and decay of small-scale rain cells from a network of rain gage measurements. Ostrovskii and Piterbarg (1995) used a 2D transport equation to estimate spatially-variable flow and turbulent diffusion of sea-surface temperature (SST) anomalies from sparse measurements of ocean temperature covariances in the Pacific Ocean. Eskes et al. (1999) used a 2D transport model in a 4D variational assimilation scheme for total column ozone measurements from the GOME satellite.

In this chapter, we first present the derivation of the ZWD transport model used in this work. This transport model is a conservation equation of mean IWV, and incorporates turbulent mixing effects. We then describe the implementation of an algorithm where we estimate IWV difference maps at the SAR overpass times using the GPS ZWD data and the ZWD transport model. This algorithm iteratively combines maps obtained by least-squares

inversion of the GPS ZWD measurements acquired before and after the SAR overpass times. Following this, we describe how we estimate spatially-variable wind, required as an input by our algorithm, using the same transport model and the GPS measurements.

7.1 Derivation of the 2D ZWD transport model

In this section, we derive a 2D ZWD transport model that describes the spatial and temporal variations of mean ZWD fields, as measured by the GPS network. The derivation here proceeds in two steps.

- First, we derive a conservation equation for IWV (proportional to ZWD), which equates the time rate of change of total IWV in a column of air with net transport of IWV into that column by total atmospheric flow.
- Second, we constrain the conservation equation to describe variations of only the mean level of IWV in a column of air. By decomposing total atmospheric flow into mean (laminar) and fluctuating (turbulent) components, the modified IWV conservation equation equates time variations of mean IWV in a column with a sum of (1) advective transport by laminar flow and (2) diffusive transport resulting from the turbulent mixing into the column. We use this modified conservation equation for mean IWV as our ZWD transport model.

7.1.1 Conservation of IWV

Spatial variation of water vapor content results from the transport of water vapor by processes in the lower atmosphere such as convection, advection by mean wind and mixing by turbulent wind vortices. These processes are characteristic of the planetary boundary layer (PBL), which is the lowest 1-2 km of the atmosphere and is directly influenced by the Earth's surface. Since atmospheric moisture is primarily concentrated near the ground and atmospheric mixing is strongest within the PBL, the magnitude and fluctuations of wet delay observed in GPS and InSAR are influenced by boundary layer processes. In general, the partial pressure of water vapor e contained in a volume element of moist air is not conserved as the parcel undergoes irregular motion in the PBL. However, specific humidity,

defined as the mass of water vapor per unit mass of moist air, is approximately conserved (Tatarskii (1961), Ishimaru (1978)). That is, the specific humidity q of water vapor in a parcel of air remains approximately constant as it is displaced by turbulent motions assuming no evaporation or condensation of water takes place. Thus, q can serve an approximate tracer of motion of air masses in the boundary layer.

Wet delay, as measured by GPS and InSAR, is proportional to specific humidity q averaged over the depth of the lower atmosphere, as

$$l_{wet}^z = \frac{1}{\kappa} \int_0^H \rho q dz \quad (7.1)$$

where ρ is the density of moist air and

$$1/\kappa = 10^{-6}[k_2 + k_3/T_m]R_v \quad (7.2)$$

We recall from Chapter 4 that the constants k_2 and k_3 in the above relate neutral atmospheric refractivity to water vapor partial pressure e and atmospheric temperature T , Eq. (4.11) in Chapter 4. T_m is the weighted mean temperature which is a function of surface temperature (Bevis et al. (1992)) and R_v is the specific gas constant for water vapor. In the above, H denotes the scale height of that portion of the troposphere in which the majority of water vapor resides. The derivation of Eq. (7.1) is given in Appendix A. We note that the quantity represented by the integral above is IWV, proportional to measured ZWD. Following our approach in Chapter 4, IWV in Eq. (7.1) is a sum of a time-invariant, topography-dependent component (due to neutral atmosphere vertical stratification) and a dynamic component resulting from water vapor transport. We ignore the vertically-stratified component because we assume that the ZWD measurements have been compensated for altitude-dependent delay. Our focus now is to describe the time-varying component of IWV.

First, we derive the conservation equation for IWV. Neglecting molecular diffusion of humidity (as opposed to turbulent diffusion which we will incorporate into the conservation equation later), the conservation of specific humidity and mass in the lower atmosphere can

be expressed as follows (Stull (1988))

$$\frac{\partial q}{\partial t} + \nabla \cdot (\mathbf{V}^{3D} q) = 0 \quad (7.3)$$

$$\frac{\partial \rho}{\partial t} + \nabla \cdot (\mathbf{V}^{3D} \rho) = 0 \quad (7.4)$$

where $\mathbf{V}^{3D} = [u \ v \ w]^T$ is the three-dimensional flow field in the PBL.

The equations above state that the temporal rate of change of mass and specific humidity in a infinitesimal volume element is given by the net flux of mass and humidity through the surfaces of that volume element (Brown (1991)). The conservation equations above can be illustrated using the 1D example in Figure 7.1, where we show a hypothetical infinitesimal volume element of air at a fixed location embedded in a 1D atmospheric flow V in the positive x -direction. The time rate of change of a scalar quantity such specific humidity q within that volume is equal to the difference in flux, ΔqV , into and out of the parcel sides at x_0 and $x_0 + dx$,

$$\frac{dq}{dt} \approx - \frac{(q \cdot V)|_{x_0+dx} - (q \cdot V)|_{x_0}}{dx} \quad (7.5)$$

This can be generalized to three dimensions, yielding Eqs (7.3) and (7.4) above.

We assume that $\nabla \cdot \mathbf{V}^{3D} = 0$. Physically, this condition represents incompressible flow, which is approximately satisfied for mesoscale PBL flows because density variations in the lower atmosphere are typically small (Stull (1988), Brown (1991)). Note that assuming a constant density of air in Eq. (7.4) yields the incompressibility condition. Adding Eq. (7.3) multiplied by q to Eq. (7.4) multiplied by ρ gives

$$\begin{aligned} \rho \frac{\partial q}{\partial t} + q \frac{\partial \rho}{\partial t} + \mathbf{V}^{3D} \cdot [\rho \nabla q + q \nabla \rho] &= 0 \\ \Rightarrow \frac{\partial \rho q}{\partial t} + \mathbf{V}^{3D} \cdot \nabla \rho q &= 0 \\ \Rightarrow \frac{\partial \rho q}{\partial t} + \nabla \cdot (\mathbf{V}^{3D} \rho q) &= 0 \end{aligned} \quad (7.6)$$

The last two lines in Eq. (7.6) are equivalent if we assume incompressibility of the flow.

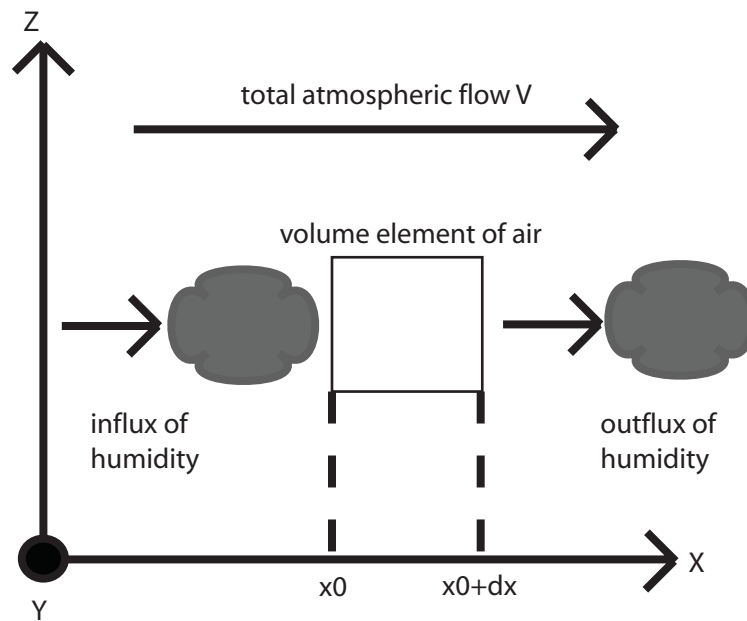


Figure 7.1 One-dimensional schematic illustration of the conservation of a humidity q within a parcel of air embedded in total atmospheric flow V . It is assumed that the flow V is uniform in all three dimensions

Integrating in the vertical direction, we obtain

$$\frac{\partial}{\partial t} \left(\int_0^H \rho q \, dz \right) + \frac{\partial}{\partial x} \left(\int_0^H u \rho q \, dz \right) + \frac{\partial}{\partial y} \left(\int_0^H v \rho q \, dz \right) + w \rho q|_H - w \rho q|_0 = 0 \quad (7.7)$$

The last two terms in Eq. (7.7) were obtained by applying Liebnitz's rule to the integral of spatial derivatives in the vertical direction in Eq. (7.6). Physically, these terms represent humidity sources such as surface evaporation and entrainment of dry air from above resulting in net flux of water vapor into the PBL.

We define vertically-averaged, weighted horizontal flow components U and V as follows

$$U = \frac{\int_0^H u \rho q \, dz}{\int_0^H \rho q \, dz}, \quad V = \frac{\int_0^H v \rho q \, dz}{\int_0^H \rho q \, dz} \quad (7.8)$$

Substituting Eq. (7.8) and Eq. (7.1) into Eq. (7.7), we arrive at a conservation equation for IWV

$$\frac{\partial(IWV)}{\partial t} + \frac{\partial(U \cdot IWV)}{\partial x} + \frac{\partial(V \cdot IWV)}{\partial y} + \text{moisture sources} = 0; \quad (7.9)$$

where, from Eq. (7.1), $IWV = \kappa l_{wet}^z$. Therefore, using the conservation of mass and humidity, we have derived an equivalent two-dimensional conservation equation for IWV.

The conservation of IWV is illustrated in Figure 7.1 if, instead of a 3D volume, we consider an infinitesimal 2D area element of dimensions $dx \times dy$ representing the base of a column of water vapor. Eq. (7.9) states that the change in IWV measured within that column is given by the net horizontal flux of IWV into that column. The horizontal flow components U and V are vertical averages of the three-dimensional atmospheric flow field, weighted by vertical profiles of moisture and air density.

In the special case of constant horizontal flow, no sources and an initial IWV distribution IWV_0 at time $t = 0$, Eq. (7.9) yields

$$IWV(x, y, t) = IWV_0(x - Ut, y - Vt) \quad (7.10)$$

which is a mathematical statement of the frozen-flow hypothesis used in Chapter 6. Thus, the conservation equation Eq. (7.9) generalizes frozen-flow transport by incorporating variable atmospheric flow.

The conservation equation for IWV can be expressed as a corresponding equation in terms of ZWD, assuming κ in Eq. (7.1) does not vary spatially or temporally. Bevis et al. (1992) empirically found that κ depends on surface temperature. We assume in the following that surface temperature varies slowly than variations in humidity. Thus, κ is effectively constant and we can replace the dependent variable IWV in Eq. (7.9) with ZWD, l_{wet}^z .

7.1.2 Incorporating turbulent mixing effects

The total atmospheric flow $[U \ V]^T$ in Eq. (7.9) can be decomposed into laminar flow, wave, and random turbulent fluctuations, each of which contribute to overall IWV (and, hence, ZWD) transport. Here, we neglect wave motion and consider only the effect of mean laminar flow and turbulence on the transport of IWV. Total horizontal flow and measured wet delay are decomposed into mean laminar and fluctuating turbulent parts, as follows (Stull (1988))

$$\begin{aligned} U &= \bar{U} + U' \\ V &= \bar{V} + V' \\ l_{wet}^z &= \bar{l}_{wet}^z + l_{wet}^{\prime z} \end{aligned} \quad (7.11)$$

where the \bar{U} , \bar{V} , and \bar{l}_{wet}^z denote mean values for horizontal flow and wet delay averaged over an area on the ground, which we denote as a grid cell. Physically, the size of this grid cell corresponds to the dimensions of the base of a column containing water vapor and, in the following, we consider the conservation of IWV averaged over this column. In the following section, we will describe an algorithm for generating maps of IWV from the GPS ZWD measurements. The size of the grid cell determines the spatial resolution of these maps.

We constrain the conservation equation for IWV, Eq. (7.9), to describe only the spatial and temporal variations of mean IWV. We do not explicitly consider the subgrid turbulent component of IWV, $l_{wet}^{\prime z}$, because the spatially-sparse observations of ZWD from the

GPS network cannot resolve these short-scale fluctuations. Similarly, we limit our consideration to advective transport due to the mean laminar component of total atmospheric flow, $\bar{\mathbf{V}}$, and ignore resolving the fluctuating components, U' and V' . Nevertheless, we do incorporate the effect of turbulence in the conservation equation for mean IWV because, apart from advection by the mean flow field, turbulence is also an effective mechanism for transporting and mixing water vapor in the atmosphere (Stull (1988)). That is, turbulence also contributes to overall spatio-temporal variation of observed ZWD. We model the effect of turbulent mixing through an additional diffusion term in the conservation equation, as shown below.

We follow the procedure of Reynolds averaging (Stull (1988), Brown (1991)) to modify the conservation equation Eq. (7.9) to incorporate turbulent effects. Substituting Eq. (7.11) into the conservation equation, and using l_{wet}^z in place of IWV , we get

$$\frac{\partial \bar{l}_{wet}^z}{\partial t} + \frac{\partial l_{wet}^{z'}}{\partial t} + \nabla \cdot \bar{\mathbf{V}} \bar{l}_{wet}^z + \nabla \cdot \bar{\mathbf{V}} l_{wet}^{z'} + \nabla \cdot \mathbf{V}' \bar{l}_{wet}^z + \nabla \cdot \mathbf{V}' l_{wet}^{z'} = 0 \quad (7.12)$$

where $\nabla = \partial/\partial x + \partial/\partial y$ and the vector $\mathbf{V} = [U \ V]^T$. We assume that the turbulent perturbations of flow U', V' and wet delay $l_{wet}^{z'}$ are zero mean. Averaging the above equation over the size of a grid cell yields

$$\frac{\partial \bar{l}_{wet}}{\partial t} + \nabla \cdot \bar{\mathbf{V}} \bar{l}_{wet} = -\nabla \cdot \overline{\mathbf{V}' l_{wet}^{z'}} \quad (7.13)$$

The equation above describes a conservation of mean ZWD when transport by total atmospheric flow consists of both laminar and turbulent components. This equation states that the time variation of mean IWV in a column of air (of size equal to a grid cell) is balanced by the sum of net IWV transport through that column due to mean laminar flow and average turbulent flux. The right-hand-side term in Eq. (7.13) denotes this average flux of IWV due to transport driven by random, short-scale turbulent eddies. We schematically illustrate laminar and turbulent transport in Figure 7.2(a). In this figure, the time-rate of change of a mean scalar such as IWV in the infinitesimal volume is now the sum of two net fluxes into that volume: (1) a flux gradient due to advection of that mean scalar by average flow $\bar{\mathbf{V}}$ and (2) a gradient of the smaller turbulent flux caused by random flow perturbations V' .

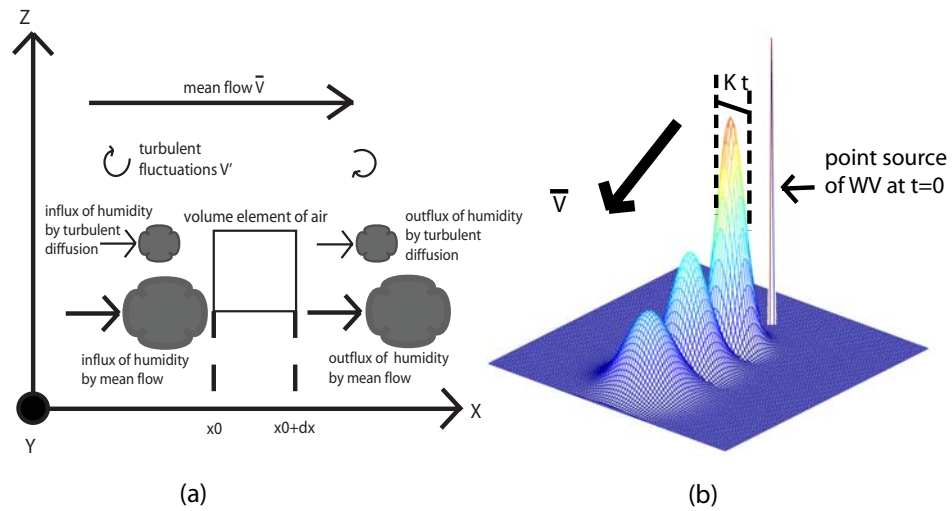


Figure 7.2 (a): One-dimensional schematic illustration of the conservation of IWV in a volume element of air embedded in a mean flow \bar{V} . The turbulent fluctuations of flow, V' , also induces transport of IWV into the volume via diffusion, in addition to advective transport by mean flow \bar{V} . (b): Spatial distribution of mean scalar field \bar{F} at three time instants, assuming a point source at $t = 0$

Therefore, we see that turbulent transport of IWV also affects the level of mean IWV in a column, in addition to the effects of advective transport caused by mean laminar flow.

Since we cannot explicitly resolve turbulent flow perturbations \mathbf{V}' or IWV fluctuations l'_{wet} in Eq. (7.13), we instead model the strength of average turbulent IWV flux, $\overline{\mathbf{V}'l'_{wet}}$, using the flux-gradient or K-theory approach (Stull (1988)), where

$$\overline{\mathbf{V}'l'_{wet}} = -K\nabla\bar{l}_{wet} \quad (7.14)$$

According to the model, the turbulent flux of ZWD is parametrized as proportional to the negative local gradient of mean ZWD. The model states that turbulent transport of ZWD is directed from regions of high IWV to areas of lower concentrations.

Substituting Eq. (7.14) in Eq. (7.13), we arrive at our transport model for mean ZWD

$$\frac{\partial\bar{l}_{wet}^z}{\partial t} + \frac{\partial\bar{U}\bar{l}_{wet}^z}{\partial x} + \frac{\partial\bar{V}\bar{l}_{wet}^z}{\partial y} = K \left(\frac{\partial^2\bar{l}_{wet}^z}{\partial x^2} + \frac{\partial^2\bar{l}_{wet}^z}{\partial y^2} \right) \quad (7.15)$$

The ZWD transport model above is known as an advection-diffusion equation. K represents the turbulent diffusion coefficient in units of m^2/s .

As an illustration of the spatial and temporal variation of mean ZWD described by the transport model, Eq. (7.15), we show in figure 7.2(b) the evolution of \bar{l}_{wet}^z at four successive time steps. In this simulation, we use a grid with a cell spacing of 0.1 meters, a mean velocity $V = 2$ m/s and a diffusion coefficient $K = 0.1$ m^2/s . At $t = 0$, mean ZWD is initially concentrated spatially at a single point. The spatial distribution of the mean ZWD evolves over time as an expanding 2D Gaussian function. The spread and amplitude of the Gaussian distribution respectively increase and decrease as Kt .

To apply this model to our data, we assume that the SCIGN GPS receivers measure ZWD fields that evolve according to Eq. (7.15). The receivers measure these fields at only the few, sparsely-distributed locations in the study area. Given estimates of mean laminar flow, \bar{V} , we apply an algorithm that iteratively generates an IWV difference map at the SAR overpass times by fitting Eq. (7.15) to the GPS ZWD measurements recorded in an interval about the SAR overpass times. Thus, the IWV difference maps we estimate from our algorithm show spatial variations of mean ZWD, l_{wet}^z , due to advection and turbulent

diffusion of water vapor. We then use this map to correct the turbulently-mixed atmospheric phase observed in the interferogram. We describe this algorithm in the next section.

7.2 Algorithm implementation

In this section, we describe our algorithm for estimating IWV difference maps. We will use these maps to reduce InSAR turbulently-mixed atmospheric phase distortions and we present our results in the following section.

Our algorithm proceeds in two steps:

- (1) estimating spatially-variable mean laminar flow from GPS ZWD data
- (2) generating IWV difference maps using the flow estimates and GPS ZWD timeseries measurements.

In both steps of our algorithm, we fit a finite-difference approximation of the ZWD transport model, Eq. (7.15), to GPS ZWD timeseries measurements. In this section, we first describe this finite-difference representation. Following that, we explain how we use this discrete model in both steps of our algorithm to estimate, respectively, mean laminar flow and IWV difference maps.

7.2.1 Finite-difference ZWD transport model

We begin the implementation by first sampling the continuous mean ZWD field, $\bar{l}_{wet}^z(x, y, t)$, on a discrete square grid over the study area with spacing Δ in both x and y dimensions and at discrete time steps separated by period Δt

$$x = i\Delta, \quad y = j\Delta, \quad t = k\Delta t \quad (7.16)$$

where

$$i = 1, \dots, M$$

$$j = 1, \dots, M$$

$$k = 0, 1, \dots, T_{window}$$

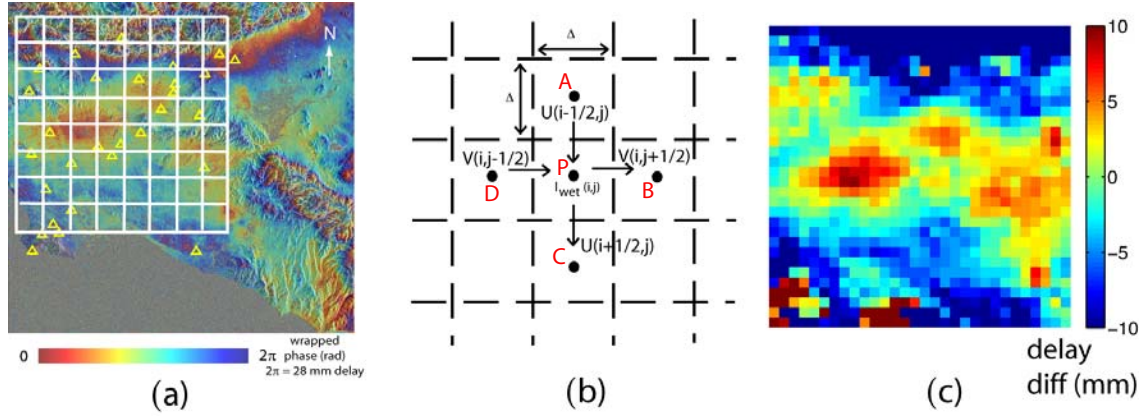


Figure 7.3 (a): Computational grid over the region of interest in the radar interferogram (Figure 3.6). The 8×8 grid shown here is for illustrative purposes only. In this work, we use a 30×30 study grid. (b): Structure of computational grid used in this study. The flow velocities are specified at the sides of the grid cells containing wet delay values. (c): Turbulently-mixed InSAR atmospheric phase (Figure 6.3(a)) downsampled to the resolution of the computational grid, $\Delta = 2.3$ km

Time $k = 0$ denotes a SAR overpass time and T_{window} refers to the time window in which we apply the ZWD transport model to the GPS ZWD timeseries. In this study, we use a 30×30 ($M = 30$) grid over the study area, as shown schematically in Figure 7.3(a). Figure 7.3(c) shows the turbulently-mixed InSAR atmospheric phase from Figure 6.3(a) downsampled to the spatial resolution of the assumed grid, $\Delta = 2.3$ km. The rms phase fluctuation of the downsampled image is 6.5 mm. We select the grid dimension M according to a trade-off between computational efficiency and the smallest wavelength of wet delay variations we can reproduce. The smallest wavelength of ZWD variations is determined by the spacing of the GPS receivers in the network and the width of the averaging cone. The IWV difference maps generated by our algorithm, which we describe later, then are spatially-resolved at a grid cell size of 2.3 km. While computational requirements associated with the implementation of our algorithm limit the spatial resolution, we will show that this resolution is sufficient to infer IWV maps that reduce the turbulently-mixed InSAR atmospheric phase distortions. In principle, specialized sparse matrix least-squares solvers could be used to reduce the number of computations required to estimate IWV maps at finer resolution. For simplicity, we use the coarser grid here. The time period Δt above is determined by the temporal sampling of wet delay measurements, as set by the GIPSY processing software,

and here $\Delta t = 30$ seconds.

The finite-difference approximation of the transport model Eq. (7.15) at a particular grid cell (i, j) is

$$\begin{aligned} \frac{l_{wet}^z(i, j, k+1) - l_{wet}^z(i, j, k)}{\Delta t} = & - \left[\frac{(l_{wet}^z \bar{U})|_{(i+\frac{1}{2}, j, k)} - (l_{wet}^z \bar{U})|_{(i-\frac{1}{2}, j, k)}}{\Delta} \right] \\ & - \left[\frac{(l_{wet}^z \bar{V})|_{(i, j+\frac{1}{2}, k)} - (l_{wet}^z \bar{V})|_{(i, j-\frac{1}{2}, k)}}{\Delta} \right] \\ & + K \left[\frac{l_{wet}^z|_{(i, j+1, k)} - 2l_{wet}^z|_{(i, j, k)} + l_{wet}^z|_{(i, j-1, k)}}{\Delta^2} \right] \\ & + K \left[\frac{l_{wet}^z|_{(i+1, j, k)} - 2l_{wet}^z|_{(i, j, k)} + l_{wet}^z|_{(i-1, j, k)}}{\Delta^2} \right] \end{aligned} \quad (7.17)$$

for $j = 1, \dots, M$ and $i = 1, \dots, M$. In the above, the spatial index is offset by $\frac{1}{2}$ to indicate that the mean laminar flow components, \bar{U} and \bar{V} , are evaluated on a separate grid offset by one half of a cell width with respect to the grid cell centers where mean wet delay \bar{l}_{wet}^z is given. This is shown schematically in Figure 7.3(b). This staggered arrangement of the two grids reduces oscillations when estimating the mean laminar flow velocities from the GPS ZWD data (Ferziger and Peric (1991)). We explain next our technique for estimating mean laminar flow.

7.2.2 Estimating spatially-variable mean flow

The first step of our algorithm involves estimating mean laminar flow parameters, \bar{U} and \bar{V} , of the ZWD transport model Eq. (7.15). We will use these estimates in the second step of algorithm, which estimates IWV difference maps.

We estimate mean flow velocities by fitting Eq. (7.15), through its discrete representation Eq. (7.17), to the measured ZWD from GPS. However, here we neglect turbulent diffusion of mean ZWD in the transport model, thereby limiting the model to only advective transport of mean IWV by laminar flow. That is, we set the turbulent diffusion coefficient K in Eq. (7.15) to zero. We neglect turbulent diffusion because decomposition of total atmospheric flow into laminar and turbulent components (Eq. (7.11)) allows us to

separate the transport mechanisms due to each of these flow components in the derivation of complete transport model, Eq. (7.15). GPS measures the spatial and temporal variation of IWV that result from both advective and turbulent diffusive transport, but here we fit only the advective transport component to the measured data to estimate mean flow.

In the discrete representation of the ZWD transport model, ignoring turbulent diffusion ($K = 0$), the set of finite-difference equations Eq. (7.17), for all grid cells (i, j) forms a system of linear equations given by

$$\frac{\mathbf{l}_{k+1} - \mathbf{l}_k}{\Delta t} = -\mathbf{A}_k \mathbf{v}_k \quad (7.18)$$

\mathbf{l}_k denotes an $M^2 \times 1$ vector whose elements are the wet delay values at all grid cells arranged in column-major order. We assume that ZWD is known at the center of every grid cell. Thus, the unknowns in Eq. (7.18) are the mean laminar flow velocities evaluated at the sides of grid cells, as depicted in Figure 7.3(b). Both components of these 2D flow unknowns are contained in the vector \mathbf{v}_k . In particular, the first $M^2 + M$ elements of the vector are all x -directed flow unknowns U evaluated on the auxiliary grid that is staggered in the x direction with respect to the ZWD grid by half a grid cell. The second set of $M^2 + M$ elements are all y -directed flow unknowns arranged on another auxiliary grid staggered in the y -direction by half a grid cell width.

The non-zero elements of the $M^2 \times 2(M^2 + M)$ matrix \mathbf{A}_k are the finite-difference approximations to ∇l_{wet}^z , but evaluated at the sides of all grid cells where the unknown flow velocities are to be estimated. Since wet delay are only known at grid cell centers, we infer values at grid cell sides by averaging mean ZWD from adjacent grid cells.

To illustrate, consider the grid cell P with adjacent cells A, B, C and D, as shown in Figure 7.3(b). If element m of the vector \mathbf{l}_k gives the mean ZWD of this grid cell, the m -th row of matrix \mathbf{A} is

$$\left[\dots \quad \frac{-(l_{wet}^z(A) + l_{wet}^z(P))}{2\Delta} \quad \frac{(l_{wet}^z(C) + l_{wet}^z(P))}{2\Delta} \quad \dots \quad \frac{-(l_{wet}^z(D) + l_{wet}^z(P))}{2\Delta} \quad \dots \quad \frac{(l_{wet}^z(B) + l_{wet}^z(P))}{2\Delta} \quad \dots \right] \quad (7.19)$$

The locations of the non-zero elements in the m -th row above correspond to the locations of unknowns $U(i - 1/2, j)$, $U(i + 1/2, j)$, $V(i, j - 1/2)$ and $V(i, j + 1/2)$ on the staggered

grid, which are given on the sides of grid cell P as shown in Figure 7.3(b). Wet delay values at the grid cell borders are inferred by averaging known mean ZWD of neighboring cells. The dot product of the m -th row above with the vector \mathbf{v}_k is the net ZWD advective flux into that grid cell P.

Our method for estimating spatially-variable mean flow fields consists of measuring the ratios of spatial gradients (Eq. (7.18) right-hand-side) to time rate of change (Eq. (7.18) left-hand-side) of ZWD at every grid cell. However, ZWD is measured by GPS at only a few, sparsely-distributed grid cells. Our method for computing mean flow assumes that mean ZWD is known at all grid cell locations. Therefore, we first infer wet delay at the grid cells outside the GPS network, and at each time step, using inverse distance weighted (IDW) interpolation of given ZWD data recorded at that time instant. This approximates the spatial gradients of the delay field which comprise the elements of the matrix \mathbf{A}_k . We mention here that without prior interpolation of wet delay at unsampled locations, it is necessary to supplement Eq. (7.18) with constraints on the expected gradients of the delay field. We chose the interpolation method because a priori wet delay spatial gradients are not available. While other interpolators such as kriging (Goovaerts (1997)) can often produce better representations of the wet delay field, here we use IDW for simplicity.

Using the sequence of measured and IDW-interpolated ZWD observations and their spatial gradients, we solve Eq. (7.18) in a least-squares sense for flow velocities. This system of equations is underdetermined, so that an infinite number of solutions is possible for flow velocities. We limit the solutions to flow fields satisfying the following constraints

$$\frac{\partial U}{\partial x} + \frac{\partial V}{\partial y} = 0 \quad (7.20)$$

$$\frac{\partial U}{\partial y} - \frac{\partial V}{\partial x} = 0 \quad (7.21)$$

The first constraint Eq. (7.20) corresponds to incompressible flow in two-dimensions discussed previously. The second constraint Eq. (7.21) assumes an irrotational flow field. These conditions are physically consistent with a description of mean laminar flow (Brown (1991)). We apply these regularization constraints to every location on the staggered flow grid where the velocities are estimated.

We also note that time, length, wet delay and flow speed quantities in Eq. (7.18) are not generally of the same order of magnitude. To avoid introducing bias in the least-squares estimates of mean flow, we equalize the magnitudes of the terms in Eq. (7.18) by scaling these quantities as follows

$$t \rightarrow t/T^*, \quad x \rightarrow x/L^* \quad l_{wet}^z \rightarrow l_{wet}^z/l^* \quad (7.22)$$

where T^* , L^* and l^* are characteristic time, length and wet delay scales. In the following, we fix $L^* = \Delta = 2.3$ km, the grid cell dimension, $l^* = 10$ mm and $T^* = \Delta t = 30$ seconds, the ZWD timeseries sampling period.

Using the finite-difference approximation Eq. (7.18), regularization constraints, Eqs. (7.20) and (7.21), as well as the non-dimensional quantities above, we estimate flow velocities as follows

$$\hat{\mathbf{v}} = \min_{\mathbf{v}} \left\| (\mathbf{l}_{k+1} - \mathbf{l}_k) - \frac{T^*}{L^* l^*} \mathbf{A}_k \mathbf{v} \right\|^2 + \left\| \frac{1}{L^*} \mathbf{H}_1 \mathbf{v} \right\|^2 + \left\| \frac{1}{L^*} \mathbf{H}_2 \mathbf{v} \right\|^2 \quad (7.23)$$

where \mathbf{H}_1 and \mathbf{H}_2 are $2M(M+1) \times 2M(M+1)$ matrices whose elements are the finite-difference approximations of the incompressibility and irrotationality constraints respectively. We note that choice of the characteristic scale factors effectively sets a weighting on the data term in the cost function Eq. (7.23) relative to the regularization terms. The impact of the characteristic scale factors in our mean flow field estimation procedure is discussed in a later section.

In the following section, we show mean laminar flow estimated from GPS ZWD data, through minimization of the cost function Eq. (7.23). Before presenting these results, however, we first explain the second step of our algorithm, which estimates IWV difference maps from the GPS ZWD timeseries.

7.2.3 Estimating IWV difference maps

The second step of our algorithm is an iterative least-squares inversion procedure where we fit the finite-difference approximation, Eq. (7.17), of the ZWD transport model to the sparse

GPS ZWD timeseries measurements. The inversion yields IWV difference maps spatially-resolved to the grid cell size of 2.3 km. Thus, in contrast to the first step of our algorithm, we do not explicitly interpolate IWV difference maps from the sparse GPS ZWD measurements. Rather, we infer ZWD through repeated fitting of the finite-difference transport model to the sparse GPS measurements, given estimates of spatially-variable mean flow obtained from the first step. In contrast to the first step also, we include turbulent diffusion in the finite-difference transport model ($K \neq 0$). We show estimated IWV difference maps in the following section.

At each time step k , the set of finite-difference equations Eq. (7.17) for all grid cells (i, j) , with K now as an additional nonzero parameter of the model, forms another system of linear equations, given by

$$\mathbf{I}_{k+1} = \mathbf{I}_k - \Delta t [\mathbf{B}_k \mathbf{I}_k + K \nabla^2 \mathbf{I}_k] \quad (7.24)$$

In Eq. (7.24), \mathbf{I}_k denotes the $M^2 \times 1$ vector of mean ZWD grid cells arranged in column-major ordering, as before. Here, the $M^2 \times M^2$ matrix \mathbf{B}_k contains flow-dependent weights that implement a finite-difference approximation of the $\nabla \cdot \overline{\mathbf{V}l_{wet}^z}$ term in Eq. (7.15). We note that since 2D mean flow are now known through the first step of our algorithm, the unknowns in Eq. (7.24) are ZWD at all grid cells where no GPS receivers are located.

We can explain the configuration of matrix \mathbf{B} by considering the m -th row of this matrix. From Eq. (7.24), the dot product of this row with \mathbf{I}_k contributes to the ZWD element m at the subsequent time step. Let the m -th element of \mathbf{I}_k correspond to grid cell P, as before. Grid cell P is shown in Figure 7.3(b). The m -th row of matrix \mathbf{B} is

$$\left[\dots \quad \frac{-U_A}{\Delta} \quad \frac{(U_P + V_P)}{\Delta} \quad \dots \quad \frac{-V_D}{\Delta} \quad \dots \right] \quad (7.25)$$

where we show only the non-zero elements of that row. In the above, V_A and V_P denote the y -directed mean flow velocities evaluated at the centers of grid cells A and P respectively. U_D and U_P denote the x -directed flow velocities at the centers of grid cells D and P respectively. Since we only evaluate flow velocities at the sides of grid cells in our implementation, we infer x - and y -directed flow at grid cell centers from bilinear interpolation of the bordering velocities. The weights in the m -th row of matrix \mathbf{B} above are positioned

according to the column-major ordering of grid cells mentioned previously. In particular, the weight $(V_P + U_P)/\Delta$ in the above constitutes the (m, m) element of matrix \mathbf{B} . Thus, we see that the dot product of the m -th row of \mathbf{B} with the mean ZWD array \mathbf{l} yields the net transport of IWV into grid cell P due to mean laminar flow, and this transport of IWV contributes to overall ZWD recorded at grid cell P (and, hence, element m of \mathbf{l}_k) at the next time step. We note that only grid cells A and D contribute to determining the advective transport of ZWD into grid cell P because, in our implementation, the gradient of ZWD flux into grid cell P is approximated by a ‘‘backward’’ finite-difference

$$\begin{aligned} \frac{\partial(\overline{U}l_{wet}^z)|_P}{\partial x} &\approx \frac{(U_P l_{wet}^z(P)) - (U_A l_{wet}^z(A))}{\Delta} \\ \frac{\partial(\overline{V}l_{wet}^z)|_P}{\partial y} &\approx \frac{(V_P l_{wet}^z(P)) - (V_D l_{wet}^z(D))}{\Delta} \end{aligned}$$

The $M \times 1$ vector $\nabla^2 \mathbf{l}_k$ is a collection of second derivatives of the wet delay field at every grid cell, and this term denotes the contribution to mean ZWD transport due to turbulent diffusion. Analogously, the m -th row of the matrix ∇^2 is

$$\left[\cdots \quad \frac{1}{\Delta^2} \quad -\frac{4}{\Delta^2} \quad \frac{1}{\Delta^2} \quad \cdots \quad \frac{1}{\Delta^2} \quad \cdots \quad \frac{1}{\Delta^2} \quad \cdots \right] \quad (7.26)$$

where, now, the (m, m) element of matrix ∇^2 is the weight $-4/\Delta^2$.

In the second step of our algorithm, we begin by initializing an empty map with GPS ZWD data acquired some time $k = T_{window}$ after each SAR overpass at only those grid cells in the map occupied by the GPS network. We then find the IWV map \mathbf{l}_k at the previous time step $k = T_{window} - 1$ that produces a prediction of the IWV map at time $k = T_{window}$, $\mathbf{l}_{T_{window}}$, which matches in a least-squares sense the GPS ZWD measurements at that time but at only those grid cells occupied by the GPS sites. Subsequently, we adjust $\mathbf{l}_{T_{window}-1}$ by replacing the values inferred at those grid cells occupied by the GPS sites with ZWD measurements now acquired at time $k = T_{window} - 1$. The resulting map at time k is then the observation used to infer the IWV map at time $k = T_{window} - 2$. This procedure is repeated backwards until the SAR overpass times $k = 0$.

We summarize our algorithm in the flow chart Figure 7.4. Mathematically, the IWV

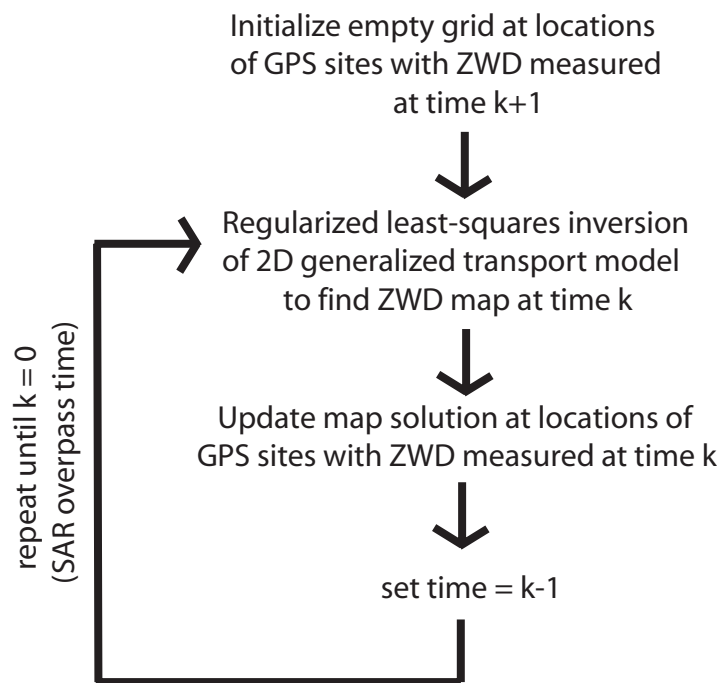


Figure 7.4 Flow chart describing iterative algorithm for estimating wet delay map using the generalized transport model Eq. (7.15) and timeseries of GPS ZWD measurements

map at time $0 \leq k \leq T_{window}$ is the map given as follows

$$\hat{\mathbf{I}}_k = \min_{\mathbf{I}_k} \|\mathbf{I}_{k+1}^{GPS} + \mathbf{B}_k \mathbf{I}_k\| + \alpha \|\nabla^2 \mathbf{I}_k\| \quad (7.27)$$

where \mathbf{I}_{k+1}^{GPS} is the IWV map estimate at time $k+1$ with values at the 29 GPS site locations now replaced by ZWD measurements acquired at time $k+1$. The regularization matrix ∇^2 is used to penalize the second-derivatives of the estimated wet delay field, thereby smoothing the resulting map. Physically, Eq. (7.27) above represents advection by mean flow given by the elements of \mathbf{B}_k and turbulent diffusion due to the regularization term of the IWV map at time k to produce the ZWD observed by GPS at the subsequent time step $k+1$. A similar procedure was implemented to solve for a map of wet delay based on ZWD timeseries recorded prior to the SAR overpass times. We then use the average of the resulting IWV difference maps propagated to the SAR overpass times ($k=0$).

7.3 Results

In this section, we present our results from applying our algorithm to the measured ZWD timeseries from the network of 29 GPS receivers. We show below estimates of spatially-variable mean laminar flow, obtained from the first step of our algorithm, and IWV difference maps at the SAR overpass times generated by the second step. We show that the IWV difference maps we estimate approximate the observed turbulently-mixed InSAR atmospheric phase distortions (Figure 6.3(a)) with lower error compared to corresponding IWV difference maps interpolated using only GPS ZWD observations recorded at the SAR overpass times, as they did in the frozen-flow algorithm of the previous chapter.

In Figure 7.5, we show estimates of mean flow velocities at the SAR overpass time, 18.31 UTC, obtained by applying Eq. (7.23) to timeseries of ZWD acquired on February 5th, 2000. In Figure 7.6, we show the flow velocities at 18.31 UTC on November 27th, 1999. The rms error from fitting the constrained finite-difference conservation equation to the GPS ZWD data was about 1 mm.

Before applying our algorithm to estimate IWV difference maps for correcting InSAR

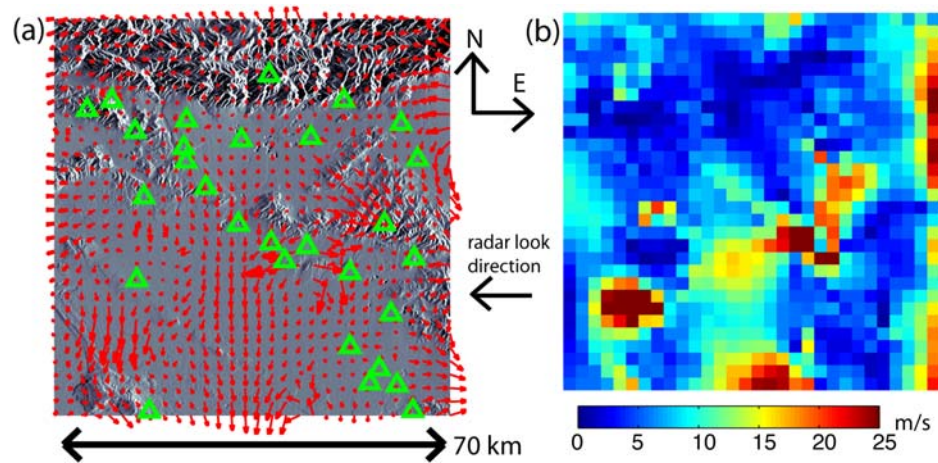


Figure 7.5 (a). Spatial distribution of flow field velocities \mathbf{V} at 18.31 UTC, February 5th, 2000. Eq. (7.23) was applied to timeseries of ZWD from the 29 GPS receivers at locations indicated by the green triangles. (b): Flow speed computed from velocity solutions on a 30×30 grid, with grid cell spacing of $\Delta = 2.3$ km

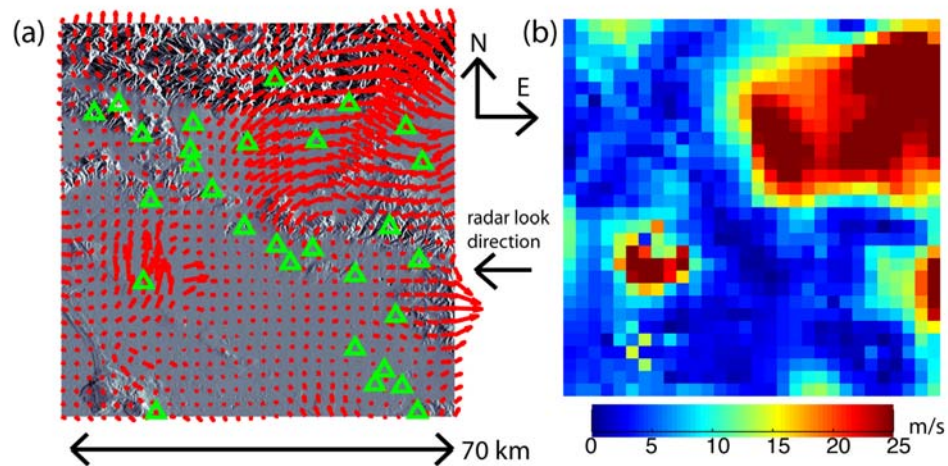


Figure 7.6 (a). Spatial distribution of flow field velocities \mathbf{V} at 18.31 UTC, November 27th, 1999. Eq. (7.23) was applied to timeseries of ZWD from the 29 GPS receivers at locations indicated by the green triangles. (b): Flow speed computed from velocity solutions on a 30×30 grid, with grid cell spacing of $\Delta = 2.3$ km

Table 7.1 Average cross-validation RMS error (mm) for estimating ZWD timeseries using the proposed algorithm and IDW-interpolation

	LS-inversion of transport model	IDW interpolation
Feb. 5th, 2000	5.3	7.4
Nov. 27th, 1999	4.5	7.2

atmospheric phase distortions, we first tested our algorithm using a cross-validation procedure. In this procedure, we removed one GPS site from the dataset and used our algorithm with the GPS ZWD timeseries measurements from the remaining 28 GPS receivers to estimate both spatially-variable flow fields and the withheld ZWD timeseries. The time window for this cross-validation experiment was 3000 seconds. We repeated this procedure for all 29 ZWD timeseries. Table 7.1 shows the cross-validation results. Specifically, the middle column shows the average rms error in mm for estimating a single ZWD timeseries by applying our algorithm to ZWD timeseries measurements from the remaining 28 receivers. The results in Table 7.1 are averaged rms errors, computed over 3000 seconds, obtained from applying the cross-validation procedure to all 29 measured timeseries.

For comparison, we also inferred the withheld ZWD timeseries by simple IDW-interpolation of the 28 GPS ZWD timeseries. The rightmost column in Table 7.1 shows the average RMS error in mm for interpolating a single ZWD timeseries using data from the remaining 28 receivers. Again, the results in the rightmost column are averages of rms errors computed from cross-validating all 29 measured GPS ZWD timeseries. We observe that over a time window of 3000 seconds centered on the SAR overpass times, our algorithm can estimate a withheld GPS ZWD timeseries with 2.4 mm better accuracy, on average, than by simply interpolating the remaining ZWD measurements.

In Figure 7.7, we show IWV difference maps estimated from the GPS ZWD timeseries measurements. These maps use different time windows about the SAR overpass times in which GPS ZWD observations were incorporated into the inversion procedure Eq. (7.27). Here, we use estimates of mean laminar flow at 2.3 km resolution as derived by our algorithm (Figures 7.5 and 7.6 show, for example, flow estimates at the SAR overpass times

only), and a diffusion coefficient $K = 3000000 \text{ m}^2/\text{s}$ which we found produces an IWV difference map that best matches (in terms of RMS error) the observed turbulently-mixed InSAR atmospheric phase (lower right corner of Figure 7.7). This value of the diffusion coefficient was constant for all time windows. Our algorithm produces IWV difference maps at the coarse 2.3 km resolution. In Figure 7.7, we have upsampled these maps at the full InSAR resolution (40 meters) for better visualization of our results.

In Figure 7.8(a), we show the global rms error as a function of time window duration for IWV maps estimated at the 2.3 km resolution. In various time windows about the SAR overpass times, we estimated these maps using our algorithm and then subtracted the results from the downsampled InSAR atmospheric phase (Figure 7.3(c)). We see from Figure 7.8(a) that, over 100 minutes, the rms error of observed turbulently-mixed InSAR atmospheric phase distortions was reduced from 6.5 mm to 5.5 mm. The residual phases after correction by the inferred maps are short-scale phase fluctuations that are not reproduced by the advection and diffusion of temporal ZWD variations from GPS. For consistency with our results in Chapter 6, Figure 7.8(b) shows the corresponding RMS error curve obtained when prior smoothing was applied using the $8 \text{ km} \times 8 \text{ km}$ boxcar filter. We note that the residuals may contain location phase features due to ground motion (Watson et al. (2002)) unmodeled by the inversion procedure or necessarily measured by the sparse network of GPS receivers. Subtracting an IDW-interpolated IWV difference map from GPS data acquired only at the SAR overpass times results in about 0.3 mm reduction in global RMS without prior smoothing and, with smoothing, the RMS error drops to 3.8 mm from 4.7 mm. Table 7.2 lists the results of RMS atmospheric phase after correction with IWV difference maps generated by the algorithm presented here.

Therefore, using the method described by Eq. (7.27), observations of ZWD from GPS acquired before and after the SAR overpass times can be incorporated into the estimation of a more accurate approximation of atmospheric phase artifacts observed by the SAR interferogram.

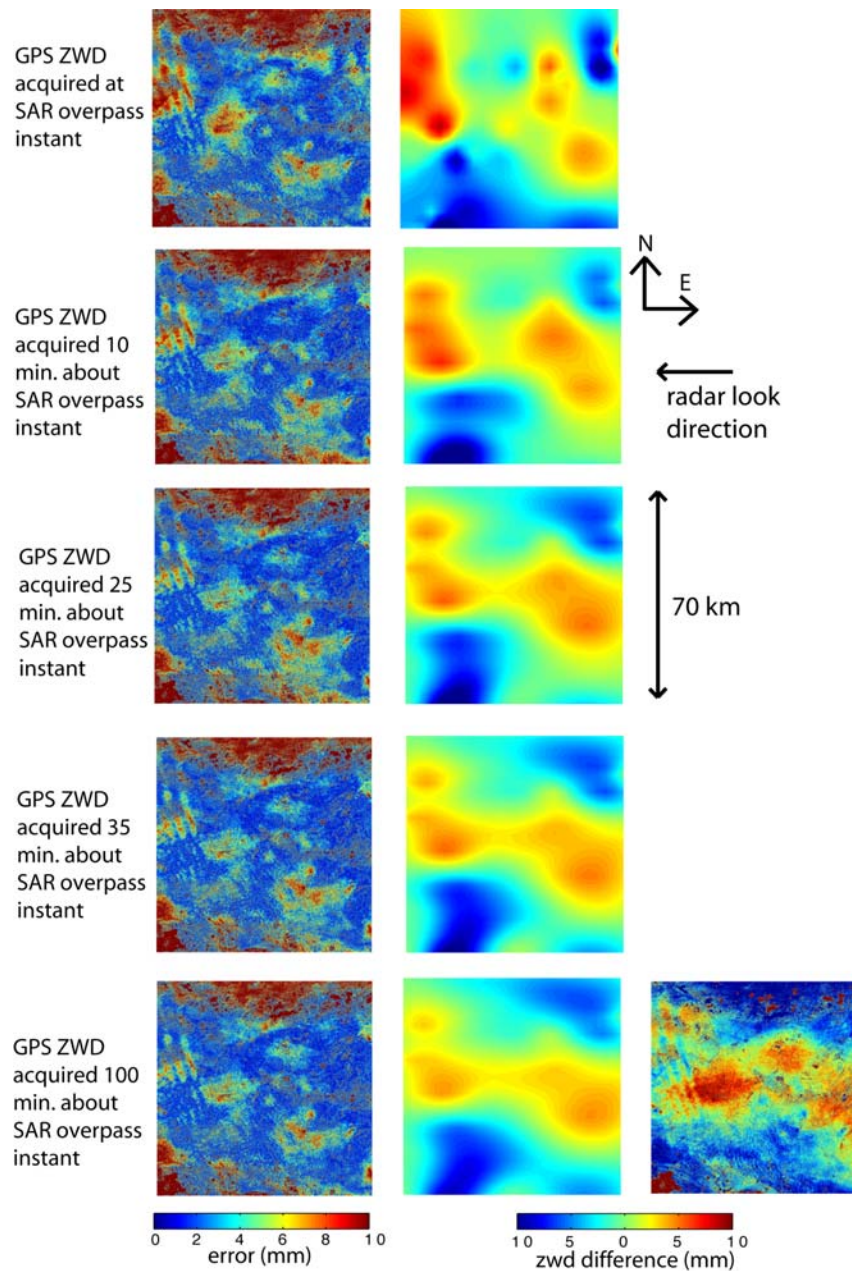


Figure 7.7 Estimates of ZWD difference at the SAR overpass time using GPS ZWD timeseries measurements and Eq. (7.27). We show maps, in the middle column, generated by using data recorded at, within 10 minutes, 25 minutes, 35 minutes and a 100 minutes over the SAR overpass times. The error magnitude from subtracting the map estimates from the observed turbulently-mixed atmospheric phase is shown in first column. The turbulently-mixed atmospheric phase is shown in the lower right corner

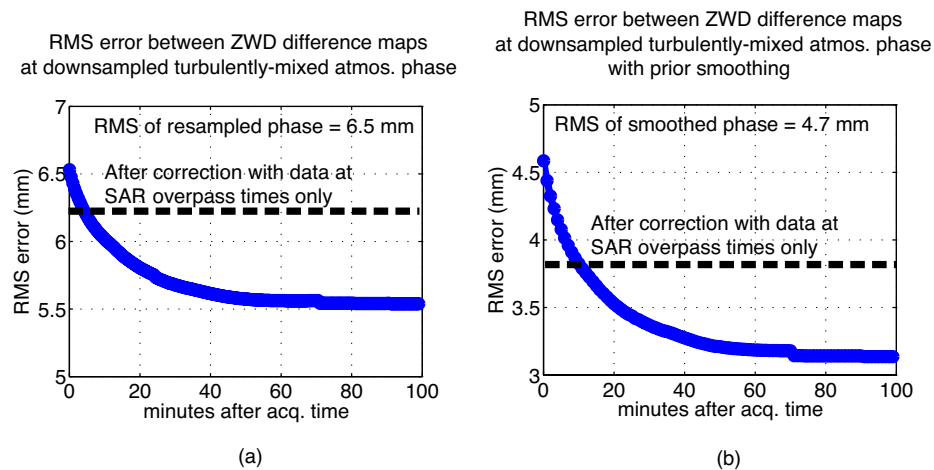


Figure 7.8 (a): RMS error as a function of time window length about SAR overpass times in which GPS ZWD measurements were used to infer IWV difference maps at the coarse 2.3 km resolution. (b): RMS error as a function of time window length with prior smoothing using the 8 km \times 8 km filter suggested by the cone-averaging effect in GPS

7.4 Discussion

We now discuss the results we obtained from least-squares inversion of the SCIGN GPS ZWD timeseries using the 2D transport model for wet delay. The algorithm presented in this chapter proceeded in two steps: (1) estimation of spatially-variable wind from the conservation equation for wet delay and (2) iterative least-squares estimation of a IWV difference map from the ZWD timeseries by using the wind estimates in a transport model for wet delay.

Comparing the results in Table 7.2 with our results in Chapter 6, Table 6.1, we find that the frozen-flow algorithm achieves a better correction of turbulently-mixed InSAR atmospheric phase distortions than the advection-diffusion algorithm presented in this chapter. Specifically, the residual rms phase fluctuation smoothed by the 8 km \times 8 km filter (suggested by the GPS averaging cone) after the frozen-flow correction is 2.7 mm while the corresponding rms phase fluctuation after the advection-diffusion correction is 3.1 mm. These results indicate that the frozen-flow algorithm delivers superior GPS-derived corrections

Table 7.2 RMS atmospheric phase fluctuations before and after GPS-derived corrections

	RMS error (mm)	
atmospheric phase	16.1	
corrected for topography-dependent variation	8.6	
resampled to $M = 30 \times 30$ grid	6.5	
	Entire spectrum	Low-pass filtered
rms error	6.5	4.7
correction using GPS ZWD at SAR overpass times only	6.2	3.8
correction using advection-diffusion algorithm	5.5	3.1

compared to the advection-diffusion algorithm. However, we note that the frozen-flow algorithm assumes accurate a priori knowledge of the spatial variation of the observed InSAR atmospheric phase, through an autocorrelation model. In contrast, the advection-diffusion algorithm presented here does not assume an a priori model for expected spatial variation of atmospheric phase. Instead, the advection-diffusion algorithm infers this variation indirectly through advective and turbulent diffusive transport of ZWD. The improved correction achieved by the frozen-flow algorithm, as shown in Table 6.1, is then a consequence of using an a priori autocorrelation model that is measured directly from the InSAR atmospheric phase.

We note that an autocorrelation function that is measured directly from the InSAR data may not always accurately describe variations solely due to the atmosphere. Non-atmospheric phase signatures, such as those due to ground deformation, will affect the general shape of the autocorrelation model, and using such a model might result in erroneous compensation of atmospheric phase components of the observed interferometric phase. To properly correct for atmospheric phase distortions, it is necessary to use an autocorrelation model that accurately describes only the atmospheric component of interferometric phase. However, most autocorrelation models for turbulently-mixed atmospheric phase are idealized and do not always accurately describe the observed variations. In particular,

most models are isotropic and thus neglect directional dependence of InSAR atmospheric effects. As we noted in Chapter 6, the frozen-flow algorithm is sensitive to the choice of assumed autocorrelation model and, consequently, an inaccurate model would further corrupt the residual ground deformation phase signatures after correction. In contrast, the advection-diffusion algorithm presented in this chapter is more general because of fewer a priori assumptions on the nature of InSAR atmospheric phase variations. We reserve for future work the incorporation of a statistical autocorrelation model of turbulent phase fluctuations into the ZWD transport model.

We find that estimates of spatially-variable wind depend on the choice of normalization constants T^* , L^* and l^* in Eq. (7.23). Since the estimated flow speeds are proportional to ratios of temporal to spatial gradients of wet delay, we expect a characteristic flow speed

$$V^* \approx \frac{L^* \partial l_{wet}^z / \partial t}{T^* \partial l_{wet}^z / \partial x} \quad (7.28)$$

We find that the large flow speeds observed in Figures 7.5 and 7.6 are due to the large ratio of assumed characteristic length to time scales, $\frac{L^*}{T^*} \approx 77 \text{ m/s}$. Typically, the characteristic length scale L^* is fixed to the dimensions of the grid cell and the time scale is set to be the sampling period. We find that increasing the characteristic time scale T^* by decimating the GPS ZWD timeseries results in a decrease in average flow speed, as shown in Figure 7.9. Thus, we see that the choice of time scale affects the overall magnitude of flow speeds inferred by our algorithm. For future work, the ambiguity in the choice of time scale can be circumvented given an a priori bound on maximum flow speed, V^* . Then, the time scale can be determined from the *Courant condition*, $T^* < L^* / V^*$ (Ostrovskii and Piterbarg (1995)). In addition, we would then have to include non-linear inequality constraints explicitly in the inversion procedure.

The estimated flow fields also depend on the spatial and temporal gradients measured from the smooth, IDW-interpolated delay fields. The choice of interpolator impacts the estimation of the flow fields because it affects the spatial gradients of ZWD from the sparse measurements. A possible improvement to this step of the algorithm is to incorporate estimates of water vapor gradients inferred from the GPS ZWD measurements themselves, as

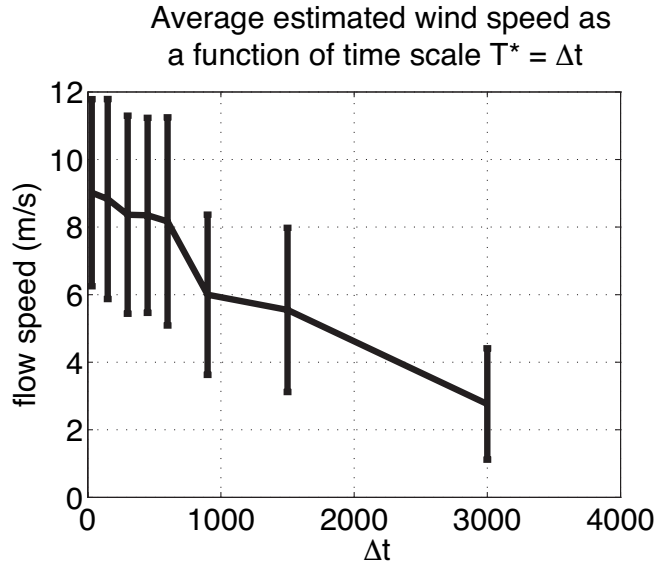


Figure 7.9 Average and standard deviation of flow speeds $\sqrt{U^2 + V^2}$ inferred from our method for a range of characteristic time scales T^*

shown by (Bar-Sever et al. (1998)), in the spatial interpolation of ZWD. The temporal gradients of ZWD are strongly influenced by the choice of the drift rate parameter, described in Chapter 3, used to estimate ZWD over time from the raw GPS carrier phase observables. While it is not possible to determine the appropriate choice of drift rate parameter without independent water vapor timeseries measurements (e.g. from ground-based water vapor radiometers), the 2D transport model for water vapor described here suggests that temporal and spatial gradients of water vapor are coupled through the flow field.

We also note that varying the normalization constants effectively changes the relative weighting between the data fitting and regularization terms in Eq. (7.23). However, we find that the impact on data fitting error is minimal for the choice of time scales shown in Figure 7.9 as the RMS error was less than 2 mm in all cases. This is because we have not incorporated an explicit weighting factor on the regularization terms in Eq. (7.23), as is conventionally done in regularized inverse problems. We neglected using an explicit regularization weighting factor because it was not possible to determine a priori the appropriate level of misfit to the GPS ZWD timeseries. Such an a priori constraint on the misfit can

be obtained, for example, by validating wind estimates produced by our methods with atmospheric motion vectors (AMV) inferred from analysis of sequences of water vapor IR images from the GOES satellites. Furthermore, comparison of our flow estimates with AMVs can also benefit the determination of an appropriate time scale T^* as, generally, the choice of this time scale depends on typical flow speeds V^* over the length scale of a grid cell (2.3 km assumed here) expected for vertically-averaged wind in the lower atmosphere. These AMV estimates can be obtained from the Cooperative Institute for Meteorological Satellite Studies (CIMSS) at the University of Wisconsin-Madison.

In our algorithm for iterative estimation of IWV difference maps from GPS timeseries, the diffusion coefficient K we used to produce the ZWD difference maps shown in Figure 7.7 is unphysically large. This is primarily because the diffusion term in Eq. (7.27) is used to smooth the ZWD difference map solution and is not directly incorporated in the data fitting component of the cost function. We chose this approach because we found that regularization with the diffusion operator smooths out errors caused by the initial ill-posedness of the inverse problem Eq. (7.27) and numerical instabilities. Thus, the magnitude of the diffusion coefficient K represents the combined effect of actual turbulent diffusion and regularization weighting. Apart from this, we find that the ratio of characteristic length to time scales used in the least-squares inversion also contributes to the magnitude of the diffusion parameter. In Figure 7.10(a), we plot the optimal diffusion coefficient K derived from our algorithm versus time scale $T^* = \Delta t$. Here, we applied our algorithm to estimate ZWD difference maps from the GPS ZWD timeseries decimated to different time scales. We fixed the length scale L^* at the grid cell size, 2.3 km. At each time scale then, we inferred the corresponding optimal K from that IWV difference map which best matches the observed InSAR phase. The RMS error between the estimated ZWD difference map and the turbulently-mixed atmospheric phase is shown in Figure 7.10(b). We observe that, except for GPS timeseries decimated to 300 seconds, the optimal diffusion coefficient decreases with increasing time interval between ZWD measurements indicating that the parameter K in our algorithm depends on the choice of time scale. We note from Figure 7.10 that the RMS error increases with increasing time scale. This is partly the result of fewer available measurements contributing to the estimation of the ZWD difference map as we decimated

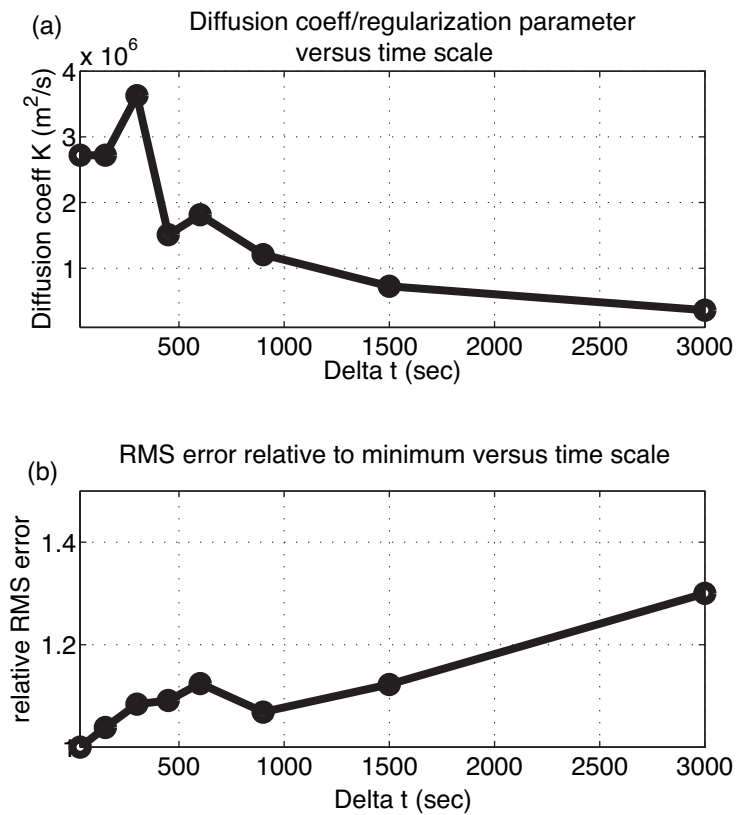


Figure 7.10 (a): Diffusion coefficient/ regularization weighting factor versus time interval (time scale) of ZWD timeseries. (b): Corresponding RMS error between estimated IWV difference map at the SAR overpass times and the downsampled turbulently-mixed InSAR atmospheric phase

the ZWD timeseries to greater time intervals. We note also that decimating the ZWD timeseries to larger time intervals may not accurately represent measurements of 2D transport of total column water vapor by Eq. (7.15) at those time scales. This is because the decimated timeseries will in general be different from ZWD timeseries estimated from raw GPS carrier phase observables initially decimated to those time scales.

7.5 Conclusions

In this chapter, we derived a transport model, parametrized by spatially-variable mean flow fields and a diffusion coefficient, that describes the spatial and temporal changes of IWV fields. We described an algorithm to estimate IWV maps at the SAR overpass times by solving an inverse problem of fitting ZWD timeseries, measured from a GPS network, to the transport model. We used these maps to correct the turbulently-mixed component of InSAR atmospheric phase variations observed in Figure 3.6.

The transport model is parameterized by spatially-variable 2D laminar flow fields. We estimated these velocity fields by fitting a finite-difference approximation of transport equation, ignoring turbulent diffusion, to the GPS ZWD timeseries. The velocity fields follow a flow model that posits non-divergent and irrotational laminar motion of air masses in the lower atmosphere. We then used estimates of flow velocity in the iterative algorithm to produce an IWV map approximating the observed turbulently-mixed atmospheric phase distortions in the radar interferogram. The IWV difference maps produced by the algorithm show spatial variations of ZWD due to advective transport and turbulent diffusion of water vapor in the atmosphere.

We tested our algorithm with a leave-one-out cross-validation procedure using the GPS ZWD timeseries. We found that our algorithm predicts the withheld GPS timeseries with an average RMS error of 2.4 mm less than the prediction error achieved by simply interpolating the other ZWD measurements.

We applied our algorithm to timeseries of ZWD from GPS acquired in a 100-minute window about the SAR overpass times. Our implementation generated IWV maps at a resolution much coarser (2.3 km) than the resolution of InSAR observations. However, we found that this was sufficient to reduce turbulently-mixed atmospheric phase distortions by

1.6 mm, assuming prior smoothing. Our algorithm produced IDW maps that further reduced RMS turbulently-mixed atmospheric phase by 0.8 mm over that achieved by simply interpolating GPS ZWD measurements acquired only at the SAR overpass times.

Our results indicate that the advection-diffusion algorithm presented in this chapter performs worse than the frozen-flow algorithm presented in the previous chapter. However, we argue that in the frozen-flow algorithm, the spatial variations of turbulently-mixed atmospheric phase are assumed to be known a priori, via an autocorrelation model, whereas the advection-diffusion algorithm does not require any prior knowledge of spatial variations of IWV. Instead, the variations are inferred indirectly through the ZWD transport model. We suggest that incorporation of an a priori atmospheric phase autocorrelation model into the advection-diffusion algorithm would be a fruitful direction for future work.

Finally, we note that the spatially-variable flow fields and the diffusion coefficient we used in our algorithm showed unphysically large values. This is a primarily an artifact of the choice of short time scales (30 seconds) and large spatial scales (grid cell size of 2.3 km) used in our implementation.

Chapter 8

A case study

In this chapter, we present a second analysis of GPS ZWD and InSAR dataset, acquired on May 14th, 2005 and July 23rd, 2005. Our objective here is again to reduce atmospheric phase distortions in this radar interferogram using timeseries estimates of ZWD from GPS. As discussed before, we do not infer quantitative measurements of water vapor from the GPS and InSAR data since this requires measurements of surface temperature over the study area to convert ZWD to total column water vapor and surface pressure data to calibrate out hydrostatic delays.

We aim to reproduce the spatial variation of atmospheric phase observed in the radar interferogram from the GPS ZWD timeseries. As before, we decompose spatial variations of wet delay into (1) a topography-dependent component due to vertical stratification of water vapor and (2) fluctuations caused by turbulent mixing of moisture in the lower atmosphere. We apply the methods presented in Chapter 5, Chapter 6 and Chapter 7 separately to estimate these two types of variations from the GPS data. These estimates will then be used to reduce total atmospheric phase distortions observed in the InSAR image.

In contrast to the 29 receivers from which we obtained the ZWD estimates shown in Figure 3.2, here we acquired data from 46 GPS receivers. This allows us to examine the performance of our methods using GPS data acquired from a denser network of receivers.

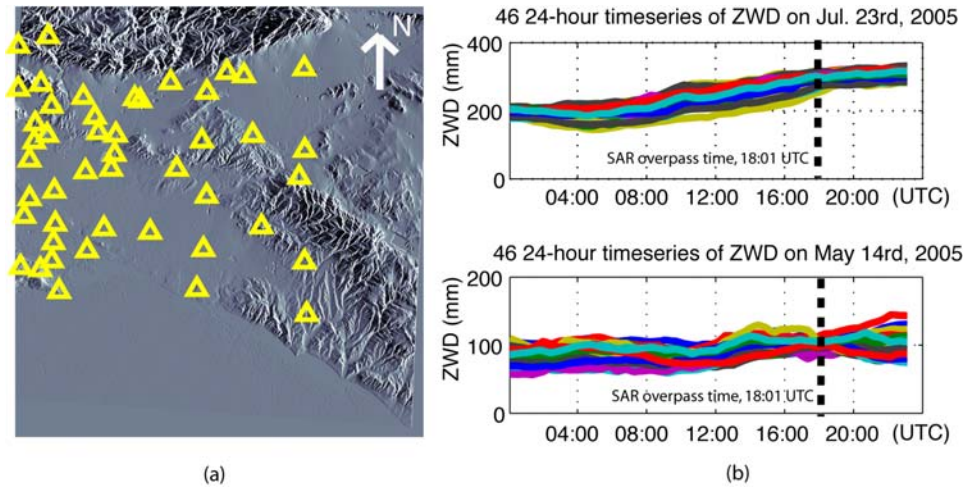


Figure 8.1 (a): Shaded relief map of the Los Angeles/Orange County basin. Yellow triangles indicate locations of SCIGN GPS receivers. (b): 24-hour timeseries of Zenith Wet Delay (ZWD) from 46 SCIGN continuous GPS receivers for July 23rd, 2005 (top) and May 14th, 2005 (bottom). The dashed vertical line in both plots indicate the time when radar observations over Southern California were acquired

8.1 GPS and InSAR observations

We obtained GPS raw carrier phase observations from 46 GPS receivers in the SCIGN network on May 14th and July 23rd, 2005. Using GIPSY, we reduced the raw GPS data to produce timeseries of ZWD sampled every 300 seconds. As in Chapter 3, we used GIPSY to solve for receiver position corrections, receiver clock offsets and ZWD from the carrier phase observables. We assumed a nominal value of 2.1 meters for zenith hydrostatic delay and we used a drift rate parameter $\alpha = 8 \times 10^{-8}$ km/ $\sqrt{\text{second}}$ for the first-order Gauss-Markov process used to model ZWD temporal variations. While processing the data, we used only GPS observations from satellites above a minimum elevation angle of 15° , and we used a Neill mapping function (Neill (1996)) to project GPS carrier phase observations at various elevation angles to the vertical. In Figure 8.1(a), we show the locations of the SCIGN receivers over the study area, while Figure 8.1(b) shows the resulting estimated ZWD timeseries from the 46 GPS receivers on both dates. The formal ZWD error, σ_{GPS} , from GIPSY processing was about 3 mm for estimates on both dates.

We formed a SAR interferogram from two ENVISAT observations of Los Angeles County, California area (33.5° N, 242.1° W) acquired at 18:01 UTC on May 14th, 2005 and July 23rd, 2005. The parameters of the ENVISAT SAR system are very similar to those of ERS-2, as given in Table 3.1. The SAR overpass times are indicated by the black dotted line in Figure 8.1. The perpendicular component of the interferometric baseline for these observations was 98.7 meters. We removed the contribution to interferometric phase due to topography, ϕ_{topo}^{INSAR} , using a DEM of the area derived from the results of the Shuttle Radar Topography Mission (SRTM) in 1999. We also removed a polynomial surface from the inferred phase image to correct a slowly-varying phase trend caused by errors in the orbit information used during SAR processing. The interferogram corrected for topography and orbit trends is shown in Figure 8.2. Due to the relatively short (2 months) time separation between SAR observations, we assumed that the contribution to interferometric phase due to tectonic effects was minimal. However, as in the previous example, we point out that phase signatures resulting from surface displacement caused by groundwater pumping and oil field activity have been observed in this area (Watson et al. (2002)). We interpret the residual phase as due primarily to (i) differences in neutral atmospheric delay (ii) temporal decorrelation, (iii) localized deformation signals and (iv) system noise. We used twenty looks during SAR processing and the resulting interferogram has a ground pixel spacing of 40 meters. We unwrapped the interferogram using the method of Chen (2001).

8.1.1 Vertical-dependence of GPS and InSAR delays

We first examine the vertical profile of GPS and InSAR observations, in order to estimate the topography-dependent atmospheric phase variations in the radar interferogram. Figure 8.3(a) shows GPS ZWD acquired at the SAR overpass times (blue squares) plotted as a function of height. We observe that the InSAR atmospheric phase exhibits a dissimilar altitude-dependent profile than was observed in the previous dataset. The atmospheric phase decreases with height for altitudes ≤ 500 meters but then increases with height at the higher altitudes. In the profile shown in Chapter 4, the InSAR atmospheric phase decreased with height for altitudes up to 2000 meters. We explain the profile observed in this dataset by noting that the InSAR atmospheric phase is proportional to a difference of

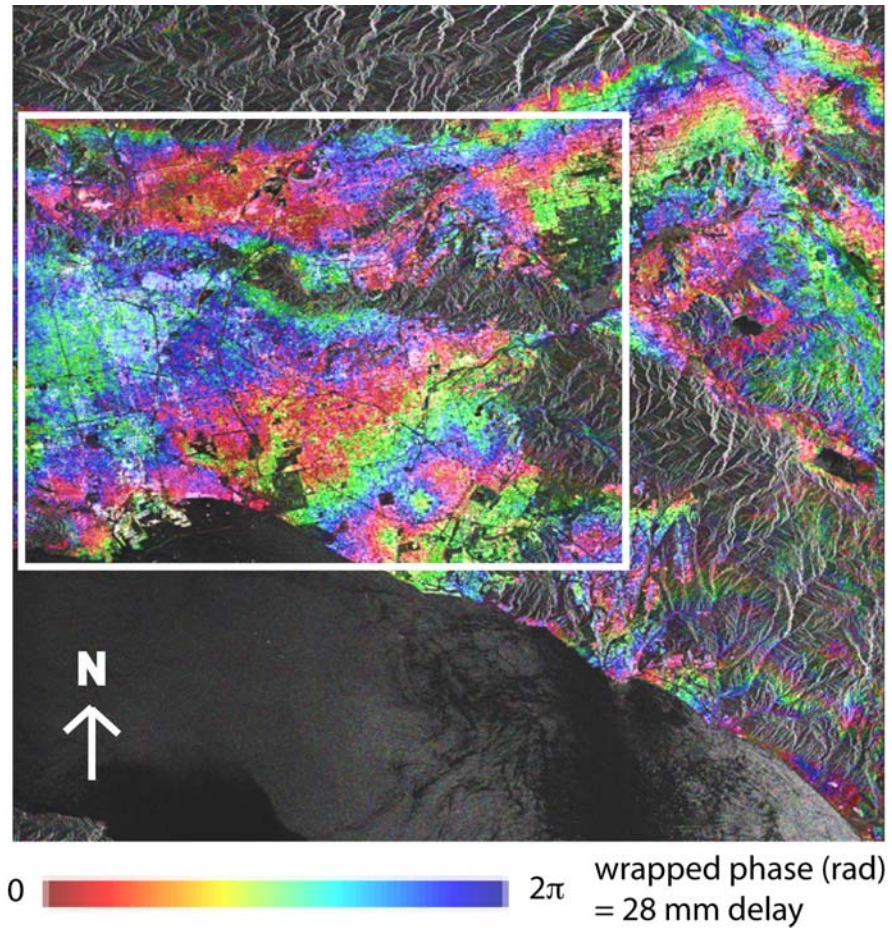


Figure 8.2 Interferogram over Los Angeles/Orange County basin derived from data acquired on May 14th 2005 and July 23rd 2005, with topographic phase removed. The area of study (white box) is approximately $60 \text{ km} \times 80 \text{ km}$

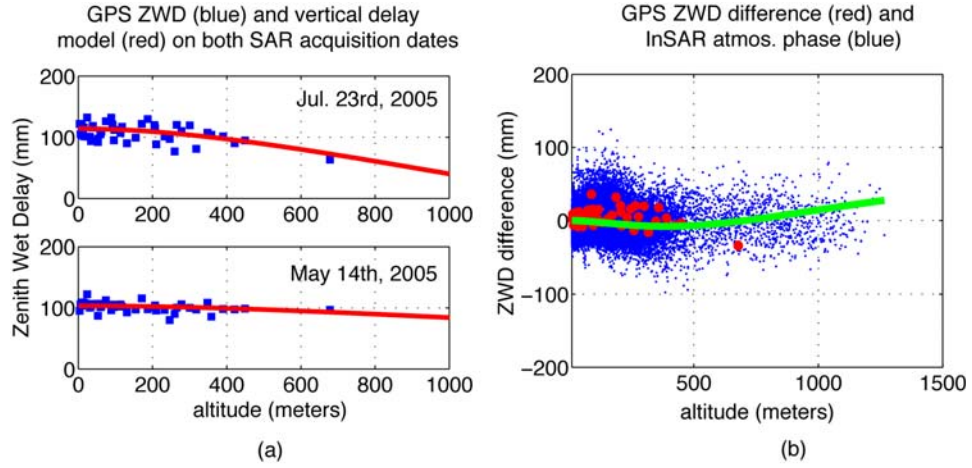


Figure 8.3 (a): GPS ZWD acquired at the 46 SCIGN stations at the SAR overpass times plotted as a function of altitude (blue). The best-fit vertical profile Eq. (5.1) is shown in red. We removed a bias of 18 cm in the GPS ZWD measurements acquired on July 23rd. (b): GPS ZWD differences at the SAR overpass times (red) and InSAR atmospheric phase (blue) plotted as function of altitude. In green, we show the profile of Eq. (5.1) fitted directly to the InSAR phase

neutral atmospheric delay vertical profiles at the two SAR overpass times. Assuming that neutral atmospheric delay decreases with height according to our model Eq. (5.1), the observed InSAR phase profiles would then be described by the difference of the two model functions. This difference model can exhibit increasing delay difference with height, depending on the relative magnitudes of the parameters C and α at the two SAR overpass times. We fit the model for vertical profile of neutral atmospheric delays, Eq. (5.1), to the measured ZWD and the resulting fits are shown in red. Table 8.1 gives the parameters C and α inferred from the fits, as well as the χ_{44}^2 goodness-of-fit statistic computed as follows

$$\chi_{44}^2 = (1/44) \sum_{k=1}^{46} \frac{(l_{wet}^{GPS,z}(z_k, t_i) - l_{vert}(z_k))^2}{\sigma_{GPS}^2} \quad t_i = \{t_1, t_2\} \quad (8.1)$$

where the factor of 1/44 in the above corresponds to 44 degrees of freedom from 46 GPS observations and 2 model parameters. The large value for the July 23rd, 2005 parameters

l_{min} and C in Table 8.1 is due to a bias of about 18 cm we observed in the GPS ZWD time-series estimated on that date. We believe that this bias is an artifact of GIPSY processing of GPS observables. We also note from Table 8.1 the large value for the χ^2 goodness-of-fit on July 23rd, 2005 relative to the goodness-of-fit on May 14th, 2005. This large value is because the formal error $\sigma_{GPS} = 3$ mm which we used to compute the chi-squared statistic underestimates the RMS of postfit-residual scatter around the model Eq. (5.1), as shown in Figure 8.3(a). The residual scatter is most likely due to ZWD fluctuations resulting from turbulent mixing of water vapor. Thus, this large χ^2 value does not necessarily suggest that the vertical dependence of GPS ZWD measurements on July 23rd, 2005 is poorly explained by the model Eq. (5.1).

Table 8.1 Parameter estimates and goodness-of-fit for altitude-dependent model fit to GPS ZWD data

	C (mm)	α (km ⁻¹)	l_{min} (mm)	χ_{44}^2
t_1 , Jul. 23rd 2005 (GPS)	294.0	0.96	243.4	21.05
t_2 , May. 14th 2005 (GPS)	103.5	0.79	80.0	5.70

In Figure 8.3(b), we plot InSAR atmospheric phase as a function of altitude (blue). The RMS atmospheric phase fluctuation was 26 mm. GPS ZWD differences are shown in red. In green, we show a vertical profile for atmospheric phase obtained from fitting our model Eq. (5.1) directly to the InSAR phase. The parameters estimated from the fit are shown in Table 8.2.

The large chi-squared goodness-of-fit statistic observed in Table 8.2 results from significant scatter of the observed InSAR atmospheric phase about the inferred model, as indicated in

Table 8.2 Parameter estimates and goodness-of-fit for altitude-dependent model fit to InSAR atmospheric phase

	C (mm)	α (km ⁻¹)	χ_{44}^2
t_1 , Jul. 23rd 2005	196.7	3.2	386.82
t_2 , May. 14th 2005	256.7	2.4	

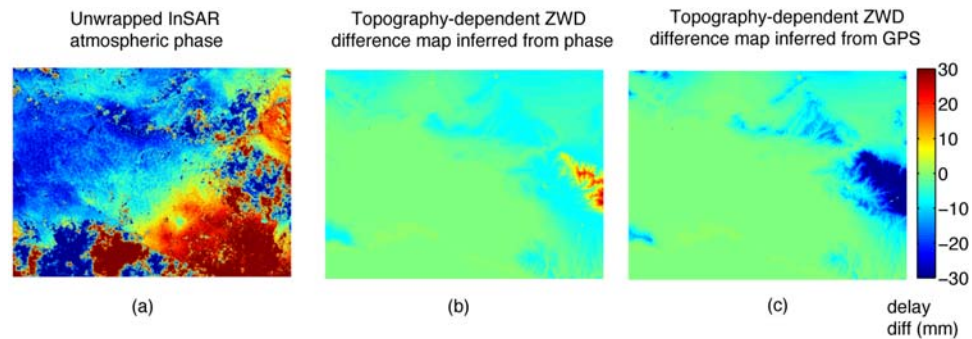


Figure 8.4 (a): Unwrapped atmospheric phase over the study area in Figure 8.2. (b): topography-dependent ZWD difference map constructed from a fit of Eq. (5.1) to the observed InSAR atmospheric phase. (c): topography-dependent IWV difference map constructed from a fit of Eq. (5.1) to the GPS ZWD observations at the SAR overpass times

Figure 8.3(b). The standard deviation of ZWD difference computed from interferometric correlation according to the formula given in Hanssen (1998) is about 5 mm. This does not take into account phase fluctuations due to the turbulent-mixing component of water vapor. The phase noise level in this InSAR observation is higher than in the InSAR data shown in Figure 3.6. This is because of the greater degree of spatial decorrelation in the SAR observations. There is a larger perpendicular baseline B_{\perp} (85 meters) between the two SAR passes here (Zebker and Villasenor (1992)) than for the observations made in 1999/2000 (1 meter).

Figure 8.4(b) shows a IWV difference map inferred from the parameters in Table 8.2 and a DEM of the area. Figure 8.4(c) shows a ZWD difference map constructed using

the GPS-derived parameters in Table 8.1. These maps are both estimates of topography-dependent atmospheric phase. However, we find that correcting the observed atmospheric phase in Figure 8.4(a), expressed as wet delay difference in mm, with the GPS-derived estimate of topography-dependent atmospheric phase results in a higher RMS residual. In contrast to the data shown in Figure 4.2, the GPS ZWD measurements here do not accurately reproduce the vertical-stratification of neutral atmospheric delays as observed in the radar interferogram. This are two possible reasons for this. First, the inferred fit of the model Eq. (5.1) to GPS ZWD observations underestimate the variation at higher altitudes due to sparsity of GPS sites at those heights. Second, the larger interferometric baseline B_{\perp} between SAR observations results in greater sensitivity of the interferometric phase to topography and topographic errors in the DEM which we used to form the image shown in Figure 8.2. Thus, it is possible that a portion of actual topography-dependent atmospheric variation was removed when we initially corrected the interferogram with the DEM. Further, we find that subtracting the IWV difference map Figure 8.4(b) from the atmospheric phase, Figure 8.4(a), yielded no reduction in RMS atmospheric phase residuals.

Therefore, the atmospheric phase shown in Figure 8.4(a) is mainly modeled as due to turbulent variations of water vapor. In the following section, we further examine the statistical spatial and temporal fluctuations of the observed atmospheric phase and GPS ZWD, individually corrected for altitude-dependent wet delay using the model Eq. (5.1).

8.2 Spatial and temporal variability

We first correct the GPS ZWD timeseries for vertical-dependent wet delay by fitting our model Eq. (5.1) to the GPS data. Since the GPS ZWD measurements do not reproduce the altitude-dependent trend of the InSAR phase data, we did not use the parameters of the InSAR fit to infer the altitude-dependent delay profiles of GPS ZWD data. Instead, both datasets were corrected for altitude-dependent trends separately, through fits to the model.

Figure 8.5 shows a comparison between ZWD differences measured at the 46 GPS sites at the SAR overpass times and corrected for vertical-dependent delay with turbulently-mixed component of InSAR atmospheric phase in $8 \text{ km} \times 8 \text{ km}$ boxes surrounding the receiver locations. Thus, Figure 8.5 compares GPS and InSAR measurements of wet delay

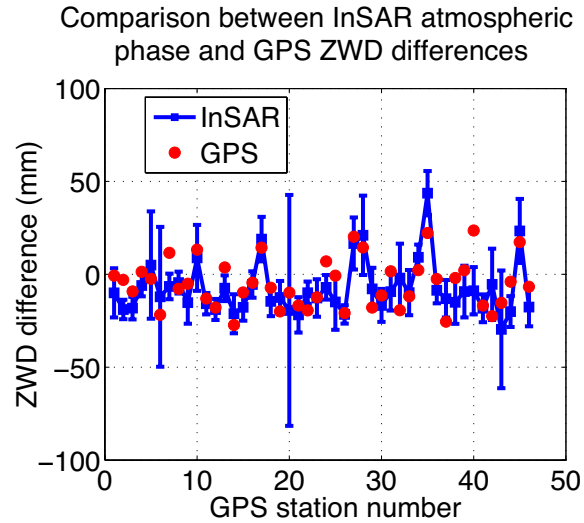


Figure 8.5 Comparison of GPS ZWD differences at the SAR overpass times (red) with InSAR atmospheric phase (blue) averaged in a box of dimensions $8 \text{ km} \times 8 \text{ km}$ centered on the receiver locations. GPS ZWD difference formal error is $\sqrt{2} \times 3 = 4.25 \text{ mm}$

after both datasets have been individually corrected for altitude-dependent delay. We compare GPS ZWD difference measurements with averaged phase in these boxes because of the cone-averaging effect in GPS ZWD estimation, as mentioned in Chapter 3. The formal error of the GPS ZWD differences shown in Figure 8.5 is $\sqrt{2} \times 3 = 4.25 \text{ mm}$. The correlation coefficient γ between GPS and InSAR measurements of wet delay differences is 0.74. We consider the statistical significance of this correlation by computing the t-statistic Eq. (5.6). The computed statistic was 7.30. If the GPS ZWD and InSAR measurements were actually uncorrelated with normally-distributed measurement noise, then the t-statistic would follow a t-distribution with $N - 2 = 44$ degrees of freedom. At a significance level of 0.01, the associated critical value of this distribution is 2.41. Since the computed statistic is greater than the critical value, we see that the computed correlation between GPS and InSAR wet delay difference measurements is statistically significant. We conclude that the GPS ZWD estimates acquired at the SAR overpass times approximates the observed InSAR atmospheric phase at the locations of the GPS receivers. From the discussion in the previous section and the results shown here, we note that while the altitude-dependent

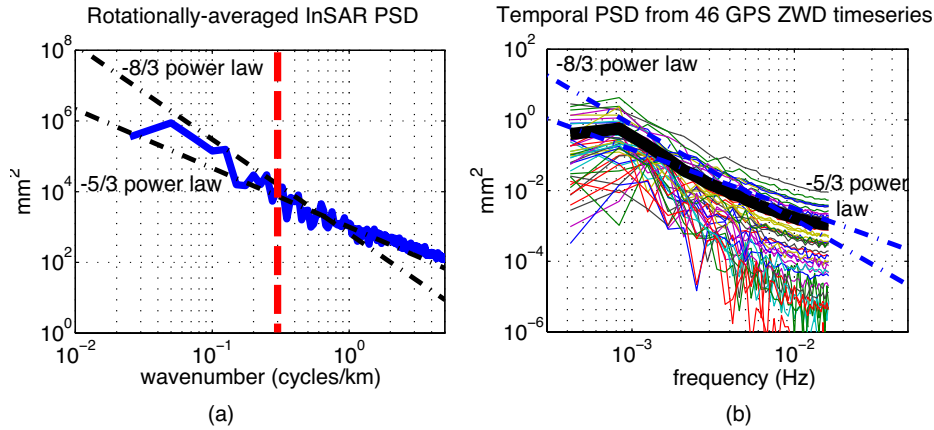


Figure 8.6 (a): Rotationally-averaged spatial PSD computed from the atmospheric phase in the center of the study area in Figure 8.2. A polynomial phase trend was subtracted from the phase values prior to computing the PSD. (b): Temporal PSD computed from detrended GPS ZWD difference timeseries measurements in a 40-minute time window about the SAR overpass times

profiles of GPS ZWD measurements and InSAR atmospheric phase do not agree, there is nonetheless a statistically significant correlation between the turbulently-mixed component of delay in these two datasets.

We now examine the spatial and temporal variability of InSAR atmospheric phase and GPS ZWD timeseries, respectively. Figure 8.6(a) shows the rotationally averaged PSD computed from the atmospheric phase in the study area shown in Figure 8.2. We note that we subtracted a polynomial phase trend from the phase values prior to computing the spectrum. Figure 8.6(b) shows temporal PSDs computed from GPS ZWD difference timeseries acquired in a 40-minute window about the SAR overpass times. The GPS data were similarly detrended prior to computing the spectrum. From the computed PSDs, we see that the fluctuations in InSAR and GPS measurements display a power-law wavelength and frequency dependence that is generally consistent with Kolmogorov theory. The observed power spectra slopes vary between $-5/3$ and $-8/3$ for different frequency/wavelength regimes. We observed this behavior for the data shown Chapter 4 and we noted that other authors (e.g. Hanssen (1998), Williams et al. (1998)) have also observed similar power law behavior in their analysis of GPS and InSAR wet delay measurements. Therefore, the short-scale variations observed in the GPS ZWD and InSAR atmospheric data here are

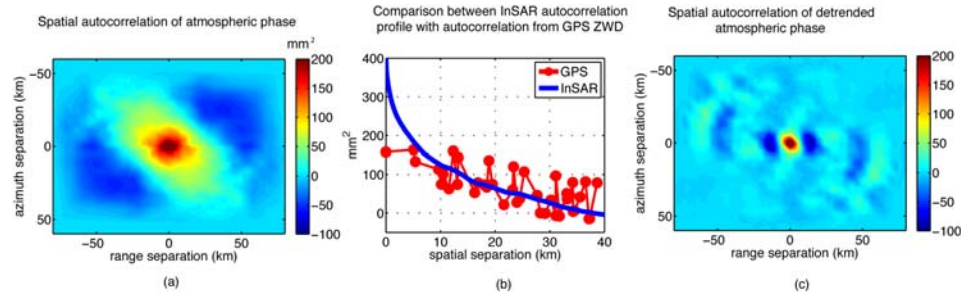


Figure 8.7 (a): Spatial autocorrelation function computed from InSAR atmospheric phase shown in Figure 8.4. (b): Comparison between InSAR autocorrelation profile (blue) and autocorrelations inferred from the GPS ZWD difference measurements at the SAR overpass times. (c): Spatial autocorrelation function computed from InSAR atmospheric phase after removing a polynomial phase trend

most likely due to turbulent mixing of water vapor.

Figure 8.7(a) shows the empirical 2D spatial autocorrelation function computed from the turbulently-mixed InSAR atmospheric phase shown in Figure 8.4(a). We quantify the distance over which these fluctuations are correlated by computing the correlation length l_{corr} ,

$$l_{corr} = \frac{1}{C(0)} \int C(r) dr \quad (8.2)$$

The correlation length of the turbulently-mixed atmospheric phase fluctuations in Figure 8.4(a) was about 7 km. Figure 8.7(b) shows the sparse autocorrelation values in red estimated using the method described in Chapter 4, from the GPS ZWD data acquired at the SAR overpass times. In Figure 8.7(b) also, we show in blue the rotationally-averaged autocorrelation function of Figure 8.7(a). The error between the sparse GPS ZWD and InSAR atmospheric phase autocorrelation values at those sparse lags was 105.4 mm^2 . We observe from Figure 8.7(b) that the GPS ZWD difference measurements significantly underestimates the spatial variations of atmospheric phase at short scales. The mean-squared fluctuations of GPS ZWD are about a factor of 2 lower than the mean-squared variations of InSAR atmospheric phase. In Figure 8.7(c), we show the empirical 2D spatial autocorrelation computed from the InSAR atmospheric phase after a removing a polynomial

phase trend from the image. We observe that the mean-squared turbulently-mixed atmospheric phase fluctuations after detrending are a factor of two lower. Furthermore, the correlation length of the detrended atmospheric phase fluctuations was reduced to about 2 km. This suggests that the large-scale correlations observed in Figure 8.7(a) are mostly the result of a large-scale gradient in the turbulently-mixed atmospheric phase. We also spatially detrended the GPS ZWD measurements and compared sparse autocorrelation values computed from the ZWD residuals with Figure 8.7(c). We found, however, that the relative error between autocorrelations of detrended GPS and InSAR measurements was higher than the relative error between the autocorrelation profiles shown in Figure 8.7(b). Therefore, we do not attempt to correct the GPS ZWD measurements for large-scale trends.

In the following section, we use the methods described in Chapter 6 and Chapter 7 to estimate the turbulently-mixed InSAR atmospheric phase distortions from the GPS ZWD measurements.

8.3 Estimating the turbulent phase variations

8.3.1 Frozen-flow algorithm

We applied the frozen-flow algorithm presented in Chapter 6 to GPS ZWD measurements acquired around the SAR overpass times. The GPS measurements were first corrected for vertically-dependent delay trends by fitting the model Eq. (5.1) to the data.

We used the 2D autocorrelation function in Figure 8.7(a) computed directly from the InSAR atmospheric phase as the autocorrelation model of wet delay spatial fluctuations. As mentioned previously, we corrected the InSAR data for altitude-dependent delay using the topography-dependent map (Figure 8.4(c)) derived from directly from the phase data, Figures 8.8(a) and (b) show the vertically-integrated, two-dimensional wind solutions inferred from correlation analysis of the GPS ZWD timeseries on both dates. Figures 8.8(c) and (d) show, in red, the denser networks of ZWD control points generated by applying the frozen-flow transport model to GPS ZWD measurements acquired in a 130-minute window after the SAR overpass times.

Figure 8.9(b) shows the combined result of kriging interpolating the denser networks

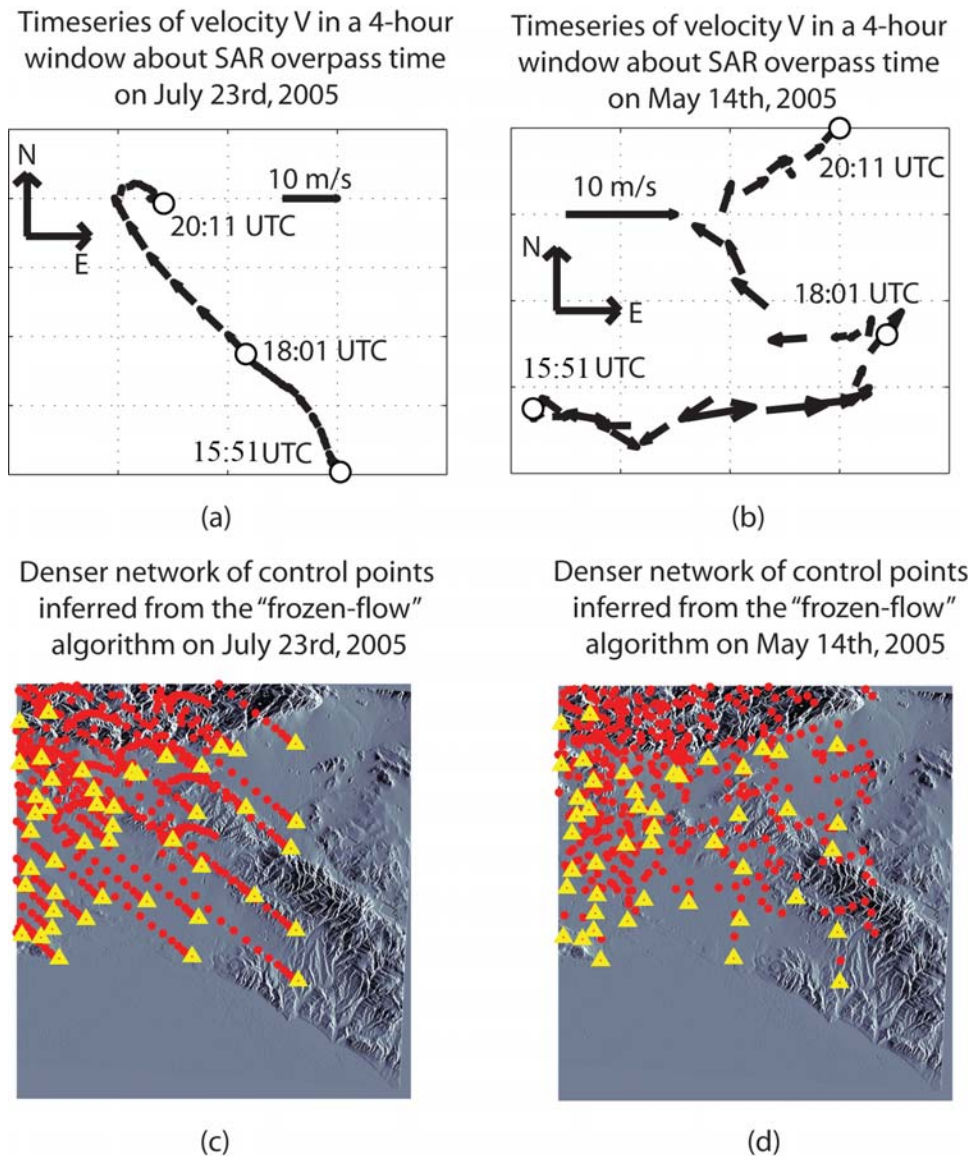


Figure 8.8 (a): Polar motion plots of vertically-integrated wind solutions in a time window of duration 130 minutes after the SAR overpass time (18:01 UTC) on Jul. 23rd, 2005. (b): Polar motion plots of wind solutions on May 14th, 2005. (c): Denser network of ZWD control points inferred by applying the "frozen-flow" algorithm (Chapter 6) to GPS ZWD timeseries on Jul. 23rd, 2005 and using wind solutions in (a). (d): Denser network of ZWD control points inferred by the "frozen-flow" algorithm for data acquired on May 14th, 2005

in Figures 8.8(c) and (d). This map is a linear combination of two maps generated by interpolating the control point networks twice using both autocorrelation functions shown in Figure 8.7. We found that using only the autocorrelation model with a large correlation length (Figure 8.7(a)) to interpolate the dense network of ZWD control points results in a smooth IWV difference map. Using an autocorrelation model with a large correlation length, a large number of control points contribute approximately equally to the estimation of ZWD difference at an unsampled location, results in a smooth interpolated map. However, by also using the autocorrelation model with a shorter correlation length (Figure 8.7(c)), fine-scale variations can be inferred and superimposed on the smooth map. Figure 8.9(d) shows the error magnitude from correcting the observed turbulently-mixed InSAR atmospheric phase distortions with the interpolated IWV difference map, Figure 8.9(b). The RMS error was reduced from 26 mm to 21.6 mm.

Figure 8.9(a) shows an IWV difference map estimated from the GPS ZWD data acquired only at the SAR overpass times using the 2D spatial autocorrelation function displayed in Figure 8.7(a). We found that a linear combination of this map with a separate IWV difference map interpolated using the autocorrelation model in Figure 8.7(c) yielded no improvement. Short-scale variations cannot be reliably inferred from ZWD measurements available only at the sparse receiver locations. We correct the observed turbulently-mixed InSAR atmospheric phase distortions, Figure 8.4(a) with this interpolated map. The magnitude of the residuals after correction is shown in Figure 8.9(c). The RMS error after correction was reduced to 23 mm from 26 mm. Thus, the frozen-flow algorithm yielded an IWV difference map that improved the reduction of atmospheric phase distortion by an additional 1.4 mm over that achieved by using GPS ZWD data acquired only at the SAR overpass times.

As with our results in Chapter 6, we find that prior smoothing improves the reduction of atmospheric phase distortion. Using a boxcar filter of dimensions $8 \text{ km} \times 8 \text{ km}$, suggested by the size of the GPS averaging cone, the RMS of atmospheric phase distortions was reduced from 18.5 mm to 12.3 mm by using the frozen-flow algorithm. In comparison, the RMS variations dropped to 14.6 mm by using GPS ZWD observations recorded only at the SAR overpass times. We note that, with prior smoothing, the improvement achieved by the frozen-flow method over that attained using only the sparse ZWD measurements was

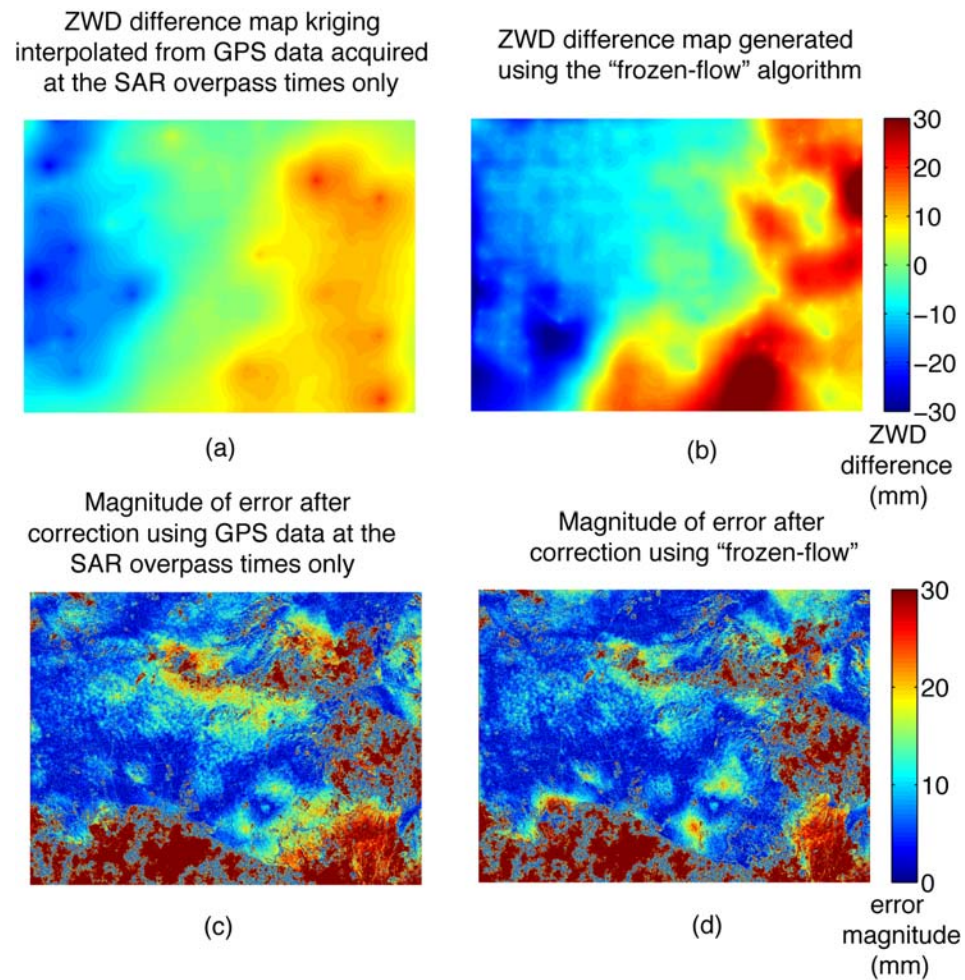


Figure 8.9 (a): IWV difference map generated by interpolating the 46 GPS ZWD difference measurements acquired at the SAR overpass times using the spatial autocorrelation model Figure 8.7(a). (b): IWV difference map generated by interpolating the dense network of control points shown in Figures 8.8 (c) and (d). (c): Error magnitude after subtracting (a) from the InSAR atmospheric phase, Figure 8.4(a). (d): Error magnitude after subtracting (b) from the InSAR atmospheric phase

Table 8.3 RMS atmospheric phase fluctuations before and after GPS-derived corrections

	RMS error (mm)	
atmospheric phase	26.0	
	Entire spectrum	Low-pass filtered
corrected for topography-dependent variation	26.0	18.5
correction using GPS ZWD at SAR overpass times only	23.0	14.6
correction using frozen-flow method	21.6	12.3

2.3 mm. This suggests that the interpolator introduces spurious high-frequency artifacts in the interpolated results, as we had noted before in Chapter 6. We summarize our results in Table 8.3.

8.3.2 Advection-diffusion modeling of GPS ZWD

For comparison, we present IWV difference maps estimated using the least-squares inversion of GPS ZWD timeseries using a generalized transport model for wet delay, as described in Chapter 7. We use a 30×30 ($M = 30$) computational grid covering an area slightly larger than the study area shown in Figure 8.2. The resulting grid cell size $\Delta = 2.67$ km. Figure 8.10 shows a sequence of ZWD difference maps generated using the advection-diffusion algorithm. We also show the change in error magnitude after correcting the turbulently-mixed atmospheric phase (lower right in Figure 8.10) with the estimated maps as the time window about the SAR overpass times is increased. For comparison, the first row in Figure 8.10 shows results we obtained by considering only GPS ZWD measurements acquired at the SAR overpass times. The IWV difference map shown in the first row was generated using IDW-interpolation.

In Figure 8.11(a), we show the RMS error as a function of time window duration about

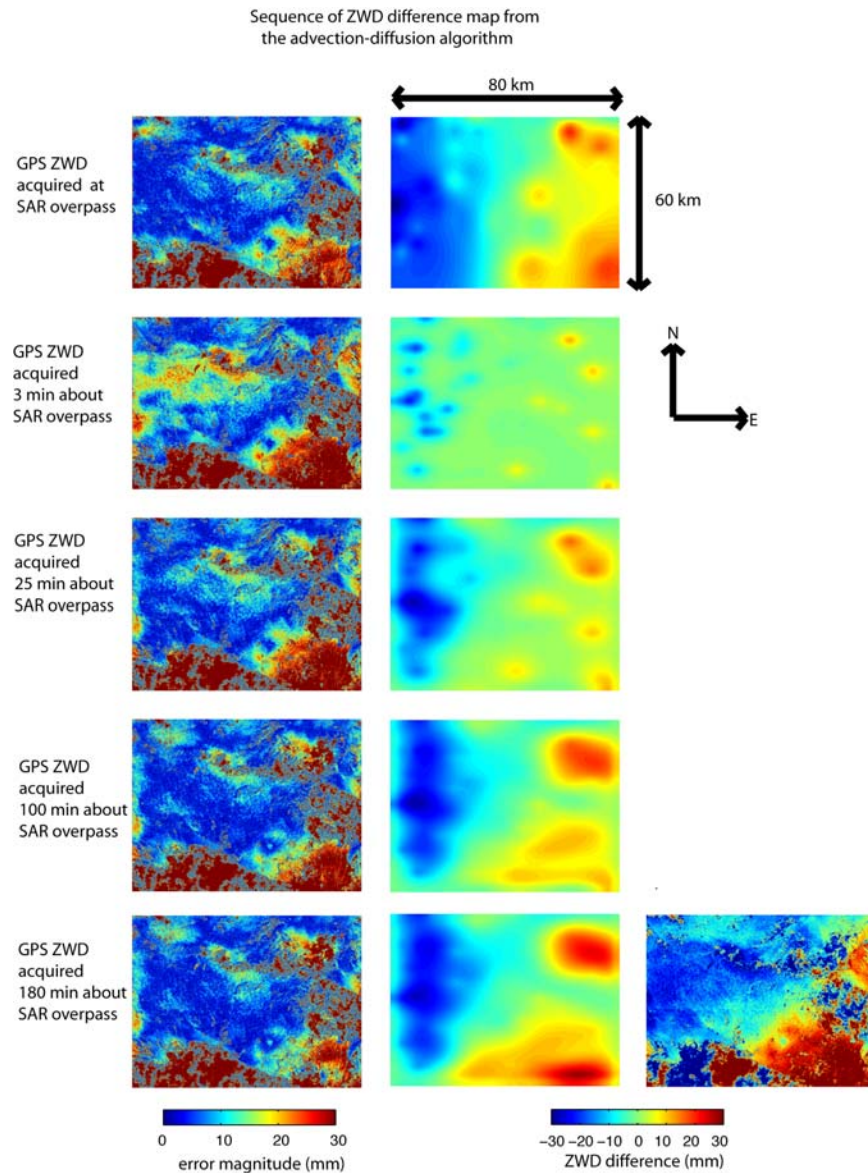


Figure 8.10 IWV difference maps from the GPS ZWD timeseries measurements and Eq. (7.27). We show maps, in the middle column, generated by using data recorded at, within 3 minutes, 25 minutes, 100 minutes and a 180 minutes over the SAR overpass times. The error magnitude from subtracting the map estimates from the observed turbulently-mixed atmospheric phase is shown in first column. The turbulently-mixed atmospheric phase is shown in the lower right corner

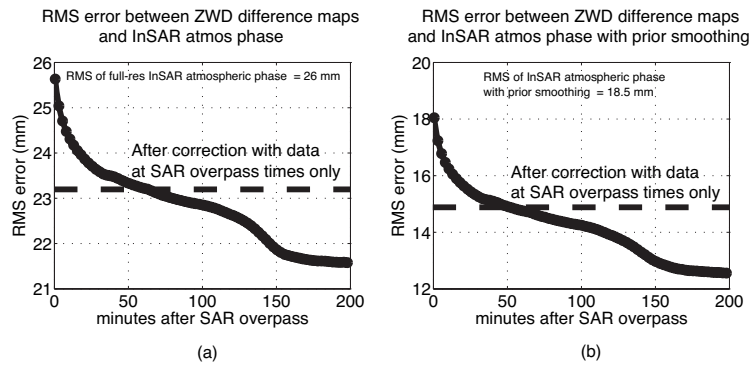


Figure 8.11 (a): RMS error between IWV difference maps inferred by the advection-diffusion algorithm and the turbulently-mixed InSAR atmospheric phase in Figure 8.4(a). (b): RMS error between ZWD difference maps and turbulently-mixed InSAR atmospheric phase with prior smoothing using an $8 \text{ km} \times 8 \text{ km}$ filter

the SAR overpass times in which GPS ZWD measurements are used in the advection-diffusion algorithm to produce IWV difference maps. For comparison, the dotted line shows the level of turbulently-mixed atmospheric phase distortion reduction achieved by correcting the phase in Figure 8.4(a) with an IDW-interpolated IWV difference map using only GPS ZWD observations acquired at the SAR overpass times. Here, we have applied corrections to the full-resolution atmospheric phase by bicubic upsampling the IWV difference maps generated by our algorithm at coarse (2.67 km) resolution to the InSAR resolution (40 meters). Figure 8.11(b) shows the corresponding RMS error when the data and IWV difference maps were smoothed with an $8 \text{ km} \times 8 \text{ km}$ boxcar filter suggested by the size of the GPS averaging cone, as we had done previously in Chapter 5, Chapter 6 and Chapter 7. Table 8.4 summarizes the results.

Table 8.4 RMS atmospheric phase fluctuations before and after GPS-derived corrections

	RMS error (mm)	
atmospheric phase	26.0	
	Entire spectrum	Low-pass filtered
corrected for topography-dependent variation	26.0	18.5
correction using GPS ZWD at SAR overpass times only	23.2	14.9
correction using advection-diffusion algorithm	21.7	12.5

Chapter 9

Conclusions

Temporal and spatial fluctuations of water vapor in the neutral atmosphere introduce excess path lengths in GPS signals and corresponding phase artifacts in InSAR interferograms. Water-vapor-induced phase distortions in InSAR interferograms are a major source of error in studies using InSAR observations to monitor ground deformation. While the error component due to water vapor can be estimated from GPS signals over time, it is not generally possible to separate out phase distortions caused by water vapor spatial variations from InSAR images alone. In this dissertation, we have presented several techniques for using GPS data to calibrate out the atmospheric phase distortions in the radar interferograms. The fundamental problem that we address in this work is how to reduce InSAR atmospheric phase distortions using ZWD measurements over time at only a few, irregularly-distributed locations within the area imaged by the radar.

9.1 Contributions

The ideas and approaches we used in this dissertation to reduce InSAR atmospheric phase distortions comprise our contributions to solving this problem, as follows:

- (1) We have shown that a sparse collection GPS ZWD measurements acquired only at the SAR overpass times can be used to generate maps proportional to total column water vapor that approximate: (i) the topography-dependent InSAR atmospheric phase distortions caused by vertical-stratification of the neutral atmosphere and (ii) the InSAR

atmospheric phase distortions resulting from the turbulent mixing of water vapor in the atmosphere. We have shown that both these maps reduce the level atmospheric phase distortion in radar interferograms.

- (2) We have developed two algorithms that can potentially surmount the limitations imposed by the sparseness of the GPS receiver network in the estimation of maps proportional to total column water vapor at InSAR resolution. These algorithms use estimates of vertically-integrated wind to incorporate additional measurements of ZWD from GPS acquired before and after the SAR overpass times. Both algorithms produce improved maps of the atmospheric phase distortion in radar interferograms. The first algorithm statistically interpolates a network of control points with greater spatial density than is suggested by the configuration of GPS receivers. This dense network is formed by applying the frozen-flow transport model and wind estimates to ZWD timeseries measured at sparse locations. The second algorithm incrementally constructs a map proportional to total column water vapor at the SAR overpass time from repeated least-squares inversions of ZWD timeseries measured from a sparse network of GPS receivers.
- (3) We have developed two algorithms to estimate vertically-integrated wind over time from ZWD timeseries sparsely measured by GPS over an area. The first algorithm is statistical and is based on the frozen-flow hypothesis of a wet refractivity field with time-invariant statistics advecting over the area containing the sparse network. The second algorithm is deterministic and is based on least-squares inversion of ZWD timeseries using a physical model of passive scalar transport by spatially-variable, vertically-integrated two-dimensional wind fields.

Our results suggest that the frozen-flow algorithm performs at least as well as the advection-diffusion algorithm at correcting InSAR atmospheric phase distortions using GPS ZWD measurements. However, we noted that this improved performance is a result of using an a priori model of spatial variations of atmospheric phase, as given by the spatial autocorrelation function measured directly from the InSAR data. The advection-diffusion algorithm does not assume any model for ZWD gradients; instead, the spatial variation of atmospheric phase is inferred from the transport model fitted to the GPS ZWD timeseries.

9.2 Future directions

Despite much effort in the field of radar interferometry devoted to solving this problem, atmospheric phase distortions remain a major source of error in InSAR images. We hope that the ideas presented in this dissertation can prove useful towards improving the quality of InSAR observations for geophysical studies. We also hope that our work can provide avenues for further research.

A possible avenue for further work is to better characterize the spatial autocorrelation function of InSAR atmospheric phase. Improved modeling of the spatial autocorrelation function of wet delay is important for accurate statistical estimation of InSAR atmospheric phase distortions. An autocorrelation model measured directly from InSAR observations may be biased by phase signatures due to non-atmospheric effects, such as the desired deformation phase. This is likely when the autocorrelation function is computed over large distances. To better characterize spatial autocorrelation of wet delay, two possible approaches might be considered:

- (1) empirically measuring spatial autocorrelation functions at different locations and over shorter distances within an imaged scene from products of two interferograms with one common SAR scene. This can provide insight into the space-varying behavior of the autocorrelation function at the time of common SAR scene.
- (2) when a GPS network is available, an autocorrelation model can be obtained from the ZWD measurements. This model can be used in the frozen-flow algorithm to generate a dense network of ZWD control points. The empirical autocorrelation of this virtual network can be compared against the autocorrelation function measured from the InSAR phase. The agreement between these two autocorrelations would be a function of wind estimates and time window around the SAR overpass times in which the frozen-flow algorithm is applied. This might provide an indication of the temporal and spatial scales of validity of the frozen-flow hypothesis and might further suggest how general models for spatial autocorrelation of turbulent wet delay fluctuations can be derived from a combination of theory (such as Kolmogorov turbulence theory) and mean wind estimates. Conversely, if the frozen-flow hypothesis for

wet delay fluctuations holds, then the shape of empirical autocorrelation functions computed from InSAR phase from (1) above may be related to mean wind.

Another possibility for future research is to validate flow estimates obtained by the frozen-flow and advection-diffusion algorithms presented in this dissertation with wind data obtained from spaceborne sensors. Atmospheric motion vectors (AMV) derived from analysis of sequences of water vapor IR images from the GOES satellites are a possible source of independent wind measurements. These estimates are produced by the Cooperative Institute for Meteorological Satellite Studies (CIMSS) at the University of Wisconsin-Madison. In particular, CIMSS produces wind estimates at different altitudes as well, thereby permitting the comparison between vertically-averaged estimates from these data and solutions produced by our algorithms. CIMSS also produces sequences of total column water vapor images over time. These measurements can also provide insight into the applicability of the frozen-flow hypothesis and the 2D transport model for describing water vapor variations over space and time.

Better characterization of the physics of water vapor transport may improve the understanding of the spatial variations of atmospheric phase observed in InSAR images. In particular, it is important to include the effects of topography and small-scale wind perturbations in the models describing moisture transport. The latter may be realized by:

- (1) using Lagrangian particle dispersion models (Wilson and Sawford (1996)) to better track and characterize individual columns of water vapor, as measured by GPS, as they are transported across space over time
- (2) incorporating more sophisticated velocity models in the Eulerian advection-diffusion approach, as opposed to simple irrotational and incompressible flow. A possibility here would be statistically model small scale fluctuations using the Kraichnan (1968) model

Appendix A

Dependence of Zenith wet delay on specific humidity

Zenith wet delay is expressed as

$$l_{wet} = 10^{-6} \left(\int_0^H k_2' \frac{P_v}{T} + k_3 \frac{P_v}{T^2} dz \right) \quad (\text{A.1})$$

where $k_2' = 17 \pm 10 \text{ K mbar}^{-1}$ (Bevis et al. (1992)). Defining weighted mean temperature as

$$T_m = \frac{\int \frac{P_v}{T} dz}{\int \frac{P_v}{T^2} dz} \quad (\text{A.2})$$

the expression for wet delay becomes

$$l_{wet} = \int_0^H \frac{1}{\kappa} \frac{P_v}{T} dz \quad (\text{A.3})$$

where $1/\kappa = 10^{-6} [k_2' + k_3/T_m] R_v$. The mean temperature T_m can be modeled empirically using measurements of surface temperature with a relative error of 2% (Bevis et al. (1992)). Thus, the factor in the integrand above is independent of height and

$$l_{wet} = \frac{1}{\kappa} \int_0^H \rho q dz \quad (\text{A.4})$$

Specific humidity is expressed as (Kursinski et al. (1997))

$$q = \left[\frac{m_d}{m_v} \left(\frac{P}{P_v} - 1 \right) + 1 \right]^{-1} \quad (\text{A.5})$$

where m_d and m_v are the molecular masses of dry air and water vapor respectively, $m_d/m_v = 1.61$, P is the total atmospheric pressure and P_v the partial pressure of water vapor. Substituting Eq. (A.5) in Eq. (A.4) gives

$$\begin{aligned} l_{wet} &= \frac{1}{\kappa R_v} \int_0^H \frac{P}{\left[\frac{m_v}{m_d} \left(\frac{1}{q} - 1 \right) + 1 \right] T} \\ &= \frac{1}{\kappa R_v} \frac{m_d}{m_v} \int_0^H \frac{Pq}{\left[1 + \left(\frac{m_d - m_v}{m_v} \right) q \right] T} \end{aligned} \quad (\text{A.6})$$

The quantity $\left[1 + \left(\frac{m_d - m_v}{m_v} \right) q \right] T$ is the virtual temperature, T_v , which is the temperature of dry air with the same density as moist air (Stull (1988)). Applying the ideal gas law for moist air $P = \rho R_d T_v$, with R_d the specific gas constant of dry air, the expression for wet delay Eq. (7.1) is obtained

$$l_{wet} = \frac{1}{\kappa} \int_0^H \rho q dz \quad (\text{A.7})$$

Appendix B

Structure functions and PSD of phase and ZWD

B.1 Introduction and preliminaries

In this appendix, we present the derivation of PSDs and structure functions of 2D InSAR turbulently-mixed atmospheric phase and 1D GPS ZWD timeseries. The derivations here parallel calculations by Tatarskii (1961) and Ishimaru (1978) and the reader is referred to these works for further details.

In the following, we let the random field $N(x, y, z, t)$ denote the turbulently-mixed water-vapor component of neutral atmospheric refractivity. We assume stationary statistics for N and the mean of N is zero. We assume further that refractivity distributions at SAR overpass times, t_1 and t_2 , have identical statistics and are mutually uncorrelated.

We will use the following notation in the derivations presented here:

- (1) The 3D structure function for N is

$$\begin{aligned} D(\mathbf{r}) &= \langle (N(x, y, z) - N(x', y', z'))^2 \rangle, \quad \text{where } \mathbf{r} = \begin{bmatrix} x - x' \\ y - y' \\ z - z' \end{bmatrix} \\ &= C^2 \|\mathbf{r}\|^{2/3}, \quad l_i < \|\mathbf{r}\| < l_o \end{aligned} \tag{B.1}$$

from Kolmogorov turbulence theory (Tatarskii (1961)). In the above, \mathbf{r} denotes the 3D spatial separation vector, while l_i and l_o are the inner and outer scales of turbulence, respectively. l_i is typically less than 100 meters while l_o is on the order of the thickness of the boundary layer where most water vapor resides, typically 1-2 km (Hanssen (1998)).

(2) The 3D PSD for N is

$$S(\mathbf{k}) \propto \|\mathbf{k}\|^{-11/3}, \quad \text{where } \mathbf{k} = \begin{bmatrix} k_x \\ k_y \\ k_z \end{bmatrix} \quad \text{and } k_o < \|\mathbf{k}\| < k_i \quad (\text{B.2})$$

In the above, \mathbf{k} denotes the 3D wavevector, while k_o and k_i are the wavenumbers corresponding to the outer and inner scales of turbulence respectively.

(4) Integrated water vapor (IWV) is

$$l(x, y, t) = \int_0^L N(x, y, z, t) dz \quad (\text{B.3})$$

where L denotes the distance from a signal source at height L to point on the ground.

(5) $D_\phi(\mathbf{R})$ and $S_\phi(\mathbf{u})$ respectively denote the 2D structure function and power spectrum of InSAR turbulently-mixed atmospheric phase, where

$$\mathbf{R} = \begin{bmatrix} x - x' \\ y - y' \end{bmatrix} \quad \text{and } \mathbf{u} = \begin{bmatrix} k_x \\ k_y \end{bmatrix} \quad (\text{B.4})$$

(6) $D_{GPS}(\tau)$ and $S_{GPS}(f)$ denote the 1D structure function and PSD of GPS ZWD time-series, where τ is time-lag in seconds and f is frequency in Hertz.

B.2 2D structure function of InSAR atmospheric phase

InSAR turbulently-mixed atmospheric phase is proportional to $l(x, y, t_1) - l(x, y, t_2)$, where t_1 and t_2 are the SAR overpass times. Since we have assumed that the two refractivity

fields at both SAR overpass times are uncorrelated random fields with identical statistics, then IWV fields l at the two times are also mutually uncorrelated and share identical statistics. Therefore, in the following, we will derive the 2D structure function for the IWV at the first SAR overpass time only, $l(x, y, t_1)$.

The 2D structure function of InSAR atmospheric phase is derived as follows (we omit the time variable t_1):

$$\begin{aligned}
D_\phi(\mathbf{R}) &\propto \langle (l(x, y) - l(x', y'))^2 \rangle \\
&= \left\langle \left[\int_0^L N(x, y, z) - N(x', y', z) dz \right]^2 \right\rangle \\
&= \int_0^L \int_0^L \langle [N(x, y, z) - N(x', y', z)][N(x, y, z') - N(x', y', z')] \rangle dz dz' \quad (\text{B.5})
\end{aligned}$$

We use the identity

$$(a - b)(c - d) = (1/2)[(a - d)^2 + (b - c)^2 - (a - c)^2 - (b - d)^2] \quad (\text{B.6})$$

to expand the integral in Eq. (B.5) above, yielding

$$\begin{aligned}
D_\phi(\mathbf{R}) &\propto \frac{1}{2} \int_0^L \int_0^L \left(\langle [N(x, y, z) - N(x', y', z')]^2 \rangle + \langle [N(x', y', z) - N(x, y, z')]^2 \rangle \right. \\
&\quad \left. - \langle [N(x, y, z) - N(x, y, z')]^2 \rangle - \langle [N(x', y', z) - N(x', y', z')]^2 \rangle \right) dz dz' \\
&= \frac{1}{2} \int_0^L \int_0^L (D(\mathbf{R}, z - z') + D(-\mathbf{R}, z' - z) - D(\mathbf{0}, z - z') \\
&\quad - D(\mathbf{0}, z' - z)) dz dz' \\
&= \int_0^L \int_0^L D(\mathbf{R}, z - z') - D(\mathbf{0}, z - z') \quad (\text{B.7})
\end{aligned}$$

where, in the last line above, we have used the fact that the structure function of refractivity is an even function in all three coordinate dimensions. Now, for an even function g , it is true that

$$\int_0^L \int_0^L g(x_1 - x_2) dx_1 dx_2 = 2 \int_0^L (L - \xi)g(\xi) d\xi \quad (\text{B.8})$$

where $\xi = x_1 - x_2$. Therefore, the structure function of InSAR atmospheric phase can be

expressed as

$$D_\phi(\mathbf{R}) \propto \int_0^L (L - \xi) [D(\mathbf{R}, \xi) - D(\mathbf{0}, \xi)] d\xi \quad (\text{B.9})$$

where $\xi = z - z'$. Eq. (B.9) is similar to results obtained by Treuhaft and Lanyi (1987). Substituting the theoretical form for the structure function of wet refractivity Eq. (B.1) into Eq. (B.9) above, and numerically integrating the result yields the profile shown in Figure 4.6, chapter 4.

B.3 2D PSD of InSAR atmospheric phase

In this section, we derive the form of the two-dimensional power spectrum of InSAR turbulently-mixed atmospheric phase. First, we note that, by the Wiener-Khinchin theorem,

$$S(\mathbf{k}) = \int_{-\infty}^{\infty} \int_{-\infty}^{\infty} \int_{-\infty}^{\infty} C(\mathbf{r}) e^{-j\mathbf{k}\cdot\mathbf{r}} d\mathbf{r} \quad (\text{B.10})$$

where $C(\mathbf{r}) = \langle N(x, y, z)N(x', y', z') \rangle$ is the 3D correlation function of the wet refractivity random field, which is assumed to be stationary.

Therefore, the PSD of 2D atmospheric phase, $S_\phi(\mathbf{u})$ is the Fourier transform of the correlation function of IWV. Specifically,

$$\begin{aligned} S_\phi(\mathbf{u}) &= \int_{-\infty}^{\infty} \int_{-\infty}^{\infty} \langle l(x, y)l(x', y') \rangle e^{-j\mathbf{u}\cdot\mathbf{R}} d\mathbf{R} \\ &= \int_{-\infty}^{\infty} \int_{-\infty}^{\infty} \left[\int_0^L \int_0^L \langle N(x, y, z)N(x', y', z') \rangle dz dz' \right] e^{-j\mathbf{u}\cdot\mathbf{R}} d\mathbf{R} \\ &= 2 \int_{-\infty}^{\infty} \int_{-\infty}^{\infty} \left[\int_0^L (L - \xi) C(\mathbf{R}, \xi) d\xi \right] e^{-j\mathbf{u}\cdot\mathbf{R}} d\mathbf{R} \end{aligned} \quad (\text{B.11})$$

where the last line in the above proceeds from applying Eq. (B.8) to the double z -integral of the correlation function, which we recognize as an even function in all three coordinate dimensions. Rearranging the order of the various integrals in the above, we arrive at an expression for the 2D PSD of InSAR atmospheric phase

$$S_\phi(\mathbf{u}) = 2 \int_0^L (L - \xi) F(\mathbf{u}, \xi) d\xi \quad (\text{B.12})$$

where $F(\mathbf{u}, \xi) = \int_{-\infty}^{\infty} \int_{-\infty}^{\infty} C(\mathbf{R}, \xi) e^{-j\mathbf{u}\cdot\mathbf{R}} d\mathbf{R}$, is the two-dimensional Fourier transform of the 3D correlation function of wet refractivity. That is, F represents the 2D PSD of a slice of the 3D refractivity correlation function C at ξ . Alternatively, $F(\mathbf{u}, \xi)$ is also given by

$$F(\mathbf{u}, \xi) = \int_{-\infty}^{\infty} S(k_x, k_y, k_z) e^{+jk_z\xi} dk_z \quad (\text{B.13})$$

Assuming that the signal propagation path length L is very large compared to the vertical correlation length of refractivity, then

$$\begin{aligned} S_\phi(\mathbf{u}) &\approx 2L \int_0^\infty F(\mathbf{u}, \xi) d\xi \\ &= 2L \int_0^\infty \left[\int_{-\infty}^{\infty} S(\mathbf{u}, k_z) e^{+jk_z\xi} dk_z \right] d\xi \\ &= L \int_{-\infty}^{\infty} \left[\int_{-\infty}^{\infty} S(\mathbf{u}, k_z) e^{+jk_z\xi} dk_z \right] d\xi \\ &= L \int_{-\infty}^{\infty} S(\mathbf{u}, k_z) \left[\int_{-\infty}^{\infty} e^{+jk_z\xi} d\xi \right] dk_z \\ &= L \int_{-\infty}^{\infty} S(\mathbf{u}, k_z) \delta(k_z) dk_z \\ &= LS(\mathbf{u}, 0) \end{aligned} \quad (\text{B.14})$$

Therefore, the 2D PSD of InSAR atmospheric phase is equal to the 3D refractivity PSD evaluated at $k_z = 0$. In particular, substituting the Kolmogorov PSD for 3D refractivity Eq. (B.2) in Eq. (B.14) above, we find that $S_\phi(\mathbf{u}) \sim \|\mathbf{u}\|^{-11/3}$

B.4 1D structure function of GPS ZWD

In this section, we derive the 1D structure function of GPS ZWD turbulence-driven fluctuations. Since GPS ZWD measurements are made at a fixed point on the ground over time, the structure function derived here will describe the variance of the difference of two ZWD measurements separated temporally, rather than spatially as was done previously.

However, we note that the statistical characterization of turbulent fluctuations which follows from Kolmogorov theory only predicts the spatial variations of refractivity and IWV. To compute temporal statistics of GPS ZWD observations, we use in the following

the “frozen-flow” hypothesis which posits a slab of neutral atmospheric wet refractivity moving at velocity V over a GPS receiver at a fixed point on the ground. The “frozen-flow” hypothesis assumes further that this moving slab has time-invariant spatial statistics described by Kolmogorov theory. As a consequence of this hypothesis, ZWD fluctuations observed over time at a fixed point is determined by the spatial fluctuations of refractivity along a particular 1D profile through the refractivity field as that slab moves over the fixed point. Thus, to determine the temporal structure function of GPS ZWD, it is sufficient to compute the structure function of only a 1D profile through the 2D field of IWV.

For simplicity, we assume that the refractivity field is moving in the x -direction, that is $V = V_x$. The ZWD timeseries measured by a GPS receiver at $(x, y) = (0, 0)$ can be expressed as

$$g(t) = l(x, 0, t)|_{x=V_x t} = \int_0^L N(x, 0, z, t) dz|_{x=V_x t} \quad (\text{B.15})$$

where the mapping $x = V_x t$ is a direct consequence of the “frozen-flow” hypothesis.

The temporal structure function of GPS ZWD is derived as follows

$$\begin{aligned} D_{GPS}(\tau) &= \langle (g(t) - g(t'))^2 \rangle, \quad \text{where } \tau = t - t' \\ &= \left\langle \left[\int_0^L N(x, 0, z) - N(x', 0, z) dz \right]^2 \right\rangle, \quad \text{where } \begin{array}{l} x = V_x t \\ x' = V_x t' \end{array} \\ &= \int_0^L \int_0^L \langle [N(x, 0, z) - N(x', 0, z)][N(x, 0, z') - N(x', 0, z')] \rangle dz dz' \quad (\text{B.16}) \\ &= \frac{1}{2} \int_0^L \int_0^L (\langle [N(x, 0, z) - N(x', 0, z')]^2 \rangle + \langle [N(x', 0, z) - N(x, 0, z')]^2 \rangle \\ &\quad - \langle [N(x, 0, z) - N(x', 0, z)]^2 \rangle \\ &\quad - \langle [N(x', 0, z') - N(x, 0, z')]^2 \rangle) dz dz', \quad \text{using Eq. (B.6)} \\ &= \frac{1}{2} \int_0^L \int_0^L (D(x - x', 0, z - z') + D(x' - x, 0, z' - z) \\ &\quad - D(0, 0, z - z') - D(0, 0, z' - z)) dz dz', \quad \text{where } x - x' = V_x(t - t') \\ &= 2 \int_0^L \int_0^L D(x - x', 0, z - z') - D(0, 0, z' - z) \\ &= \int_0^L (L - \xi) [D(x - x', 0, \xi) - D(0, 0, xi)] d\xi, \quad \text{textrm{using Eq. (B.8)} \end{aligned}$$

Therefore, we see that when wind V is known, the temporal structure function for GPS

ZWD can be obtained from the spatial structure function of IWV, Eq. (B.9) as follows

$$D_{GPS}(\tau) = D_{\phi}(V_x \tau, 0) \quad (\text{B.18})$$

We see then that the temporal structure function of ZWD as measured by GPS follows the Treuhaft and Lanyi model (Treuhaft and Lanyi (1987)), which is plotted in Figure 4.6, except that the horizontal axis in meters is replaced with time lag in seconds by the “frozen-flow” hypothesis.

B.5 1D PSD of GPS ZWD

In this section, we derive the 1D temporal PSD of GPS ZWD fluctuations. Following our approach in the derivation of the ZWD temporal structure function, we assume the “frozen-flow” hypothesis to convert between spatial and temporal statistics. Also, we assume as before that the flow of a refractivity slab is x -directed with velocity $V = V_x$.

Let the temporal correlation function of GPS ZWD fluctuations measured at $(x, y) = (0, 0)$ be $R(\tau)$. The corresponding temporal PSD of ZWD measured by a GPS receiver is, by the Wiener-Khinchine theorem

$$\begin{aligned} S_{GPS}(f) &= \int_{-\infty}^{\infty} R(\tau) e^{-j2\pi f \tau} d\tau \\ &= \int_{-\infty}^{\infty} \langle g(t)g(t') \rangle e^{-j2\pi f \tau} d\tau, \quad \text{where } \tau = t - t' \\ &= \int_{-\infty}^{\infty} \langle l(x, 0)l(x', 0) \rangle e^{-j2\pi f \tau} d\tau, \quad \text{where } \begin{array}{l} x = V_x t \\ x' = V_x t' \end{array} \\ &= \int_{-\infty}^{\infty} \left[\int_0^L \int_0^L \langle N(x, 0, z)N(x', 0, z') \rangle dz dz' \right] e^{-j2\pi f \tau} d\tau \\ &= \int_{-\infty}^{\infty} \left[\int_0^L \int_0^L C(x - x', 0, z - z') dz dz' \right] e^{-j2\pi f \tau} d\tau \end{aligned} \quad (\text{B.19})$$

where, from “frozen-flow”, $x - x' = V_x \tau$. Also, C in the last line above denotes the 3D correlation function of wet refractivity. Since C is an even function in the vertical coordinate,

we use Eq. (B.8) again to express the 1D PSD of GPS ZWD as

$$S_{GPS}(f) = 2 \int_{-\infty}^{\infty} \left[\int_0^L (L - \xi) C(x - x', 0, \xi) d\xi \right] e^{-j2\pi f \tau} d\tau \quad (\text{B.20})$$

As before, if we assume that the signal propagation path length is much larger than the vertical correlation length of refractivity fluctuations, then the following approximation can be made

$$S_{GPS}(f) = 2L \int_{-\infty}^{\infty} \left[\int_0^L C(x - x', 0, \xi) d\xi \right] e^{-j2\pi f \tau} d\tau \quad (\text{B.21})$$

The quantity in the paranthesis above is the 1D correlation function of GPS ZWD measurements. We observe that this correlation function is obtained from the 3D correlation function of refractivity by integrating out the z dimension and evaluating the 3D surface at the plane $y = 0$ (since the motion of the refractivity slab was assumed to be x -directed). By the properties of Fourier transforms then,

$$S_{GPS}(f) = \int_{-\infty}^{\infty} S(k_x, k_y, 0) dk_y, \quad \text{where } k_x = f/V_x \quad (\text{B.22})$$

Substituting in Eq. (B.22) the 3D PSD for refractivity as predicted from Kolmogorov theory, Eq. (B.2), we find that $S_{GPS}(f) \sim f^{-8/3}$.

Bibliography

AGU (December 1995). Water vapor in the climate system special report. *on the web*.

Bar-Sever, Y. E., Kroger, P. M., and Borjesson, J. A. (1998). Estimating horizontal gradients of tropospheric path delay with a single gps receiver. *Journal of Geophysical Research*, 103:5019–35.

Bevis, M., Businger, S., Herring, T. A., Rocken, C., Anthes, R. A., and Ware, R. H. (1992). Gps meteorology: remote sensing of atmospheric water vapor using the global positioning system. *Journal of Geophysical Research*, 97:15787–801.

Born, M. Wolf, E. (1959). *Principles of Optics*. Pergamon Press, London.

Brown, R. A. (1991). *Fluid Mechanics of the Atmosphere*. Academic Press, Inc., San Diego.

Celani, A. and Seminara, A. (2006). Large-scale anisotropy in scalar turbulence. *Physical Review Letters*, 96:184501/1–4.

Chen, C. W. (2001). *Statistical-cost Network-flow Approaches to Two-dimensional Phase Unwrapping for Radar Interferometry*, chapter 4. Space, Telecommunications and Radioscience Laboratory Technical Report SU-RIG-2001-1, Dept. Electrical Engineering, Stanford University, Stanford, California.

Corpetti, T., Memin, E., and Perez, P. (2002). Dense estimation of fluid flows. *IEEE Transactions on Pattern Analysis and Machine Intelligence*, 24:365–80.

- Davis, J., Herring, T., Shapiro, I., Rogers, A. E. E., and Elgered, G. (1985). Geodesy by radio interferometry: Effects of atmospheric modelling errors on estimates of baseline length. *Radio Science*, 20:1593–1607.
- Delacourt, C., Briole, P., and Achache, J. (1998). Tropospheric corrections of sar interferograms with strong topography. application to etna. *Geophysical Research Letters*, 25:2849–52.
- Elgered, G., Davis, J., Herring, T., and Shapiro, I. (1991). Geodesy by radio interferometry: Water vapor radiometry for estimation of the wet delay. *Journal of Geophysical Research*, 96:6541–6555.
- Elosegui, P., Rius, A., Davis, J. L., Ruffini, G., Keihm, S., Burki, B., and Kruse, L. P. (1998). An experiment for estimation of the spatial and temporal variations of water vapor using gps data. *Physics and Chemistry of the Earth*, 23:125–130.
- Emardson, T. R., Simons, M., and Webb, F. H. (2003). Neutral atmospheric delay in interferometric synthetic aperture radar applications: Statistical description and mitigation. *Journal of Geophysical Research*, 108:2231.
- Emardson, T. R. and Webb, F. H. (2002). Estimating the motion of atmospheric water vapor using the global positioning system. *GPS Solutions*, 6(1-2):58–64.
- Emeis, S. (1997). Numerical dispersion models for emission monitoring by spectroscopic remote sensing methods. *Proceedings of SPIE*, 3106:120–127.
- Eskes, H. J., Piders, A. J. M., Levelt, P. F., Allaart, M. A. F., and Kelder, H. M. (1999). Variational assimilation of gome total-column ozone satellite data in a 2d latitude-longitude tracer-transport model. *Journal of the Atmospheric Sciences*, 56:3560–72.
- Ferziger, J. H. and Peric, M. (1991). *Computational Methods for Fluid Dynamics*. Springer, Germany.
- Gao, B. C. and Kaufman, Y. J. (2003). Water vapor retrievals using moderate resolution imaging spectroradiometer (modis) near-infrared channels. *Journal of Geophysical Research*, 108:4389.

- Gersho, A. and Gray, R. (1992). *Vector quantization and signal compression*. Kluwer Academic Publishers, Norwell, Massachusetts.
- Goldstein, R. (1995). Atmospheric limitations to repeat-track radar interferometry. *Journal of Geophysical Research*, 22:2517–20.
- Goldstein, R. and Zebker, H. (1987). Interferometric radar measurement of ocean surface currents. *Nature*, 328:707–9.
- Goovaerts, P. (1997). *Geostatistics for Natural Resources Evaluation*. Oxford University Press.
- Hanssen, R. (1998). *Atmospheric heterogeneities in ERS tandem SAR interferometry*, chapter 2. Delft University Press, The Netherlands.
- Hanssen, R. F., Weckwerth, T. M., Zebker, H. A., and Klees, R. (1999). High-resolution water vapor mapping from interferometric radar measurements. *Science*, 283:1297–9.
- Ishimaru, A. (1978). *Wave Propagation and Scattering in Random Media, Volume 2*. Academic Press.
- Jinno, K., Kawamura, A., Berndtsson, R., Larson, M., and Niemczynowicz, J. (1993). Real-time rainfall prediction at small space-time scales using a 2-dimensional stochastic advection-diffusion model. *Water Resources Research*, 29:1489–1504.
- Kraichnan, R. (1968). Small-scale structure of a scalar field convected by turbulence. *Physics of Fluids*, 11:945–963.
- Kursinski, E., Hajj, G. A., Schofield, J. T., Linfield, R. P., and Hardy, K. R. (1997). Observing earth's atmosphere with radio occultation measurements using the global positioning system. *Journal of Geophysical Research*, 102:23429–65.
- Li, Z., Fielding, E. J., Cross, P., and Muller, J.-P. (2006). Interferometric synthetic aperture radar atmospheric correction:gps topography-dependent turbulence model. *Journal of Geophysical Research*, 111:B02404.

- Li, Z., Muller, J.-P., Cross, P., and Fielding, E. J. (2005). Interferometric synthetic aperture radar (insar) atmospheric correction: Gps, moderate resolution imaging spectrometer (modis), and insar integration. *Journal of Geophysical Research*, 110:B03410.
- Lichten, S. M. and Border, J. S. (1987). Strategies for high-precision global positioning system orbit determination. *Journal of Geophysical Research*, 92:12751–62.
- Massonnet, D., Feigl, K., Rossi, M., and Adragna, F. (1994). Radar interferometric mapping of deformation in the year after the landers earthquake. *Nature*, 369:227–30.
- Massonnet, D., Rossi, M., Carmona, C., Adragna, F., Peltzer, G., Feigl, K., and Rabaute, T. (1993). The displacement field of the landers earthquake mapped by radar interferometry. *Nature*, 364:138–42.
- Neill, A. (1996). Global mapping functions for the atmosphere delay at radio wavelengths. *Journal of Geophysical Research*, 101:3227–3246.
- Olmi, L. (2001). Systematic observations of anomalous refraction at millimeter wavelengths. *Astronomy and Astrophysics*, 374:348–357.
- Ostrovskii, A. and Piterbarg, L. (1995). Inversion for heat anomaly transport from sea surface temperature time series in the northwest pacific. *Journal of Geophysical Research*, 100:4845–65.
- Peltzer, G., Rosen, P., Rogez, F., and Hudnut, K. (1998). Poroelastic rebound along the landers 1992 earthquake surface rupture. *Journal of Geophysical Research*, 103:30131.
- Press, W., Teukolsky, S., Vetterling, W., and Flannery, B. (1986). *Numerical Recipes*, chapter UK. Cambridge Univ. Press.
- Saastamoinen, J. (1972). Introduction to practical computation of astronomical refraction. *Bulletin Geodesique*, 106:383–397.
- Sandwell, D. and Price, E. (1998). Phase gradient approach to stacking interferograms. *Journal of Geophysical Research*, 103:30183–30204.

- Sandwell, D. and Sichoix, L. (2000). Topographic recovery from stacked ers interferometry and a low resolution digital elevation model. *Journal of Geophysical Research*, 105:211–28.
- Segall, P. and Davis, J. (1997). Gps applications for geodynamics and earthquake studies. *Annal Review of Earth and Planetary Sciences*, 25:301–336.
- Smith, J. E. K. and Weintraub, S. (1953). The constants in the equation for atmospheric refractive index at radio frequencies. *Proceedings of the I.R.E*, 41:1035–1037.
- Solheim, F., Vivekanandan, J., Ware, R., and Rocken, C. (1999). Propagation delays induced in gps signals by dry air, water vapor, hydrometeors and other particulates. *Journal of Geophysical Research*, 104:9663–70.
- Stotskii, A. (1973). Large-scale phase fluctuations in propagation of radio waves in turbulent atmosphere. *Radio Engineering and Electronic Physics*, 18:1150–1154.
- Stull, R. B. (1988). *An Introduction to Boundary Layer Meteorology*. Academic Publishers, The Netherlands.
- Tatarskii, V. (1961). *Wave propagation in a turbulent medium*. McGraw-Hill, New York.
- Thayer, G. (1974). An improved equation for the radio refractive index of air. *Radio Science*, 9:803–807.
- Treuhaft, R. N. and Lanyi, G. E. (1987). The effect of the dynamic wet troposphere on radio interferometric measurements. *Radio Science*, 22:251–65.
- Wadge, G., Webley, P. W., James, I. N., Bingley, R., Dodson, A., Waugh, S., Veneboer, T., Puglisi, G., Mattia, M., and et. al, D. B. (2002). Atmospheric models, gps and insar measurements of the tropospheric water vapour field over mount etna. *Geophysical Research Letters*, 29:1905.
- Watson, K. M., Bock, Y., and Sandwell, D. (2002). Satellite interferometric observations of displacements associated with seasonal groundwater in the los angeles basin. *Journal of Geophysical Research*, 107:2074–2089.

- Weckwerth, T., Wulfmeyer, V., Wakimoto, R., Hardesty, R., Wilson, J., and Banta, R. (1999). Ncar-noaa lower-tropospheric water vapor workshop. *American Meteorological Society*, 80:2339–2357.
- Wickert, J., Reigber, C., Beyerle, G., Konig, R., Marquardt, C., Schmidt, T., Grunwaldt, L., Galas, R., Meehan, T. K., Melbourne, W. G., and Hocke, K. (2001). Atmosphere sounding by gps radio occultation: First results from champ. *Geophysical Research Letters*, 28:3263.
- Williams, S., Bock, Y., and Fang, P. (1998). Integrated satellite interferometry: tropospheric noise, gps estimates and implications for interferometric synthetic aperture radar products. *Journal of Geophysical Research*, 103:27051–67.
- Wilson, J. and Sawford, B. (1996). Lagrangian stochastic models for trajectories in the turbulent atmosphere. *Boundary Layer Meteorology*, 78:191–210.
- Zebker, H. and Villasenor, J. (1992). Decorrelation in interferometric radar echoes. *IEEE Transactions on Geoscience and Remote Sensing*, 30:950–9.
- Zebker, H. A. and Goldstein, R. M. (1986). The displacement field of the landers earthquake mapped by radar interferometry. *Journal of Geophysical Research*, 91:4993–9.
- Zebker, H. A., Rosen, P. A., and Hensley, S. (1997). Atmospheric effects in interferometric synthetic aperture radar surface deformation and topographic maps. *Journal of Geophysical Research*, 102:7547–63.
- Zimmerman, D., Pavlik, C., Ruggles, A., and Armstrong, M. P. (1999). An experimental comparison of ordinary and universal kriging and inverse distance weighting. *Mathematical Geology*, 31:375–390.
- Zumberge, J. F., Heflin, M. B., Jefferson, D. C., Watkins, M. M., and Webb, F. H. (1997). Precise point positioning for the efficient and robust analysis of gps data from large networks. *Journal of Geophysical Research*, 102:5005–17.